Technical Physics Letters, Vol. 27, No. 7, 2001, pp. 529–532. Translated from Pis'ma v Zhurnal Tekhnicheskoĭ Fiziki, Vol. 27, No. 13, 2001, pp. 1–9.

Acoustic Emission during Electrohydrodynamic Instability Development in a Nematic Liquid Crystal

E. G. Aksel'rod, A. N. Kuz'min, V. I. Kryuk, V. A. Dobrin, and K. L. Shvamm

Ural State Academy of Forestry Technology, Yekaterinburg, Russia

Received November 4, 2000

Abstract—It is experimentally demonstrated that a nonstationary motion of the convective rolls in a nematic liquid crystal is accompanied by the generation of acoustic waves. Informative parameters of the acoustic emission exhibit correlations with the type, morphology, and dynamics of the dissipative structures appearing in a cell with a large aspect ratio during increase in the critical parameter. We show a principal possibility to provide a quantitative description of the chaotic dynamics of dissipative structures in the space of parameters of the observed acoustic emission. *© 2001 MAIK "Nauka/Interperiodica".*

The existing theoretical methods used to describe the phenomenon of self-organization accompanying structural transitions in liquid crystals under the action of external fields are mostly applicable to the low-dimensional and model systems with a restricted number of the degrees of freedom (i.e., with small values of the aspect ratio Γ) and small values of the critical parameters [1]. Therefore, the development and application of new experimental methods for the investigation of dissipative structures and the study of possible scenarios of transition to the chaotic regime in real liquid-crystalline (LC) structures with distributed parameters is still an important task.

In this respect, interesting possibilities are offered by the acoustic emission (AE) spectroscopy—a method based on the detection of elastic stress waves arising as a result of the dynamic local changes in LC structures and the analysis of relationships between the AE signal and the motion of linear defects, domain boundaries, and phase interfaces. The nature of AE and the conditions of its manifestation in mesogenic structures are still insufficiently studied. In particular, no data are available on the AE activity of LC dissipative structures [2].

We have experimentally established for the first time that the formation and evolution of such dissipative structures during the electrohydrodynamic (electroconvection) instability development in LC systems with large aspect ratios are accompanied by the generation of acoustic waves. An analysis of this AE allowed us to justify the principal possibility of describing the chaotic dynamics of the field of the director **n** (related to the motion of elements of the dissipative structures) in the space of parameters of the AE pulses.

The experiments were performed with an experimental setup ensuring the registration of a series of AE parameters simultaneously with the measurement of optical properties and morphology of the LC texture. The experimental procedure was described in detail elsewhere [3]. A thermosonimetric chamber, including a sandwich-type cell with an MBBA liquid crystal ($\Gamma = 250$) in contact with a piezoelectric transducer, was mounted on the table of a polarization microscope equipped with a photoelectron multiplier detector and a video camera. The channels measuring the acoustic and optical response signals employed the principle of analog linear detection of the emission spectra. The main characteristics of the AE registration channel were as follows: frequency band, 0.5–20 kHz; total gain, 130 dB; intrinsic noise level (reduced to the input impedance), ≤ 4 μV; dynamic range of the amplitude measurement, 42 dB; time interval between pulses, 5–500 ms; threshold AE power (detection sensitivity), ~0.1 pW.

A special AE registration scheme ensured separation of a weak quasiperiodic AE signal from the noise background by (i) recording the AE time series into the memory of a multichannel pulse analyzer, (ii) grouping the analyzer channels, (iii) accumulating the data of coherent measurements with the channel background subtraction, and (iv) digital data processing. The AE was measured both in stationary dissipative structures (with a constant potential difference U across the cell) and for the transitions between different structures (with a linear U sweep at a rate of $\beta = 1$–10 V/min). The electroconvection in the LC mesophase is accompanied by the appearance of a series of dissipative structures. The order, type, and characteristic dimensions of these patterns and the corresponding threshold voltages (see table) agree with the published data [4].

An important point is to select an optimum frequency for the AE signal detection. The perturbations in orientation of the director **n** arise when the Eriksen number $\mathrm{Er} = \gamma\rho dV/K$ (where $\rho \sim 10^3$ kg/m^3 is the den-

1063-7850/01/2707-0529$21.00 © 2001 MAIK "Nauka/Interperiodica"

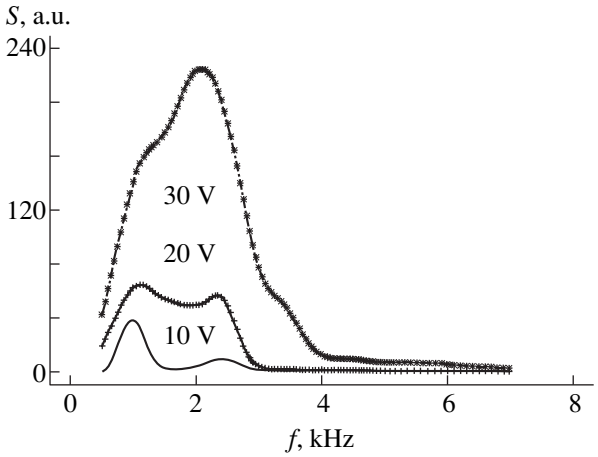

Fig. 1. The power spectra of AE from stationary dissipative structures measured at various values of the applied control voltage.

sity, $\gamma \sim 1$ cP is the rotational viscosity, and $K \sim 10^{-12}$ N is the Frank modulus of the liquid crystal) reaches a critical level of about unity, which is attained for a convective flow velocity of $V \sim 1$–100 μm/s. Accordingly, the characteristic frequency f of the flow velocity pulsations during the acoustic emission (determined by the Strouhal number $\mathrm{Sh} = fV/d$) falls within the 10^{-1}–10^{1} kHz range. Note that, for a given U, the V and d distributions are rather narrow, which is indicative of a limited frequency band of the acoustic emission from stationary dissipative structures.

The data presented in Fig. 1 show that the formation of dissipative structures is actually accompanied by the generation of acoustic waves. The main AE power (up to a several pW) falls within the frequency band from 0.5 to 7.0 kHz. The AE power generated by the elements of dissipative structures with a characteristic scale d obeys the relationship $W \propto d^2V^p$, where the velocity is proportional to the critical parameter ($V \propto (U^2 - U_1^2)$) and the characteristic size is inversely proportional to the applied voltage ($d \propto U^{-1}$) (see table). Therefore, $W \propto (U^2 - U_1^2)^n$, where $n = p - 2$. The experimental value of $n \approx 3.9$ is indicative of a predominantly dipole character of the AE sources [5], which is related to a nonstationary motion of the convective rolls.

A joint analysis of the behavior of acoustic and optical signals in the LC system studied in response to variation of the control parameter shows that the frequency and time parameters of the AE flux are correlated with the type, morphology, and dynamics of the LC dissipative structures (see Fig. 2 and the table). The data presented in Fig. 2 indicate that the probability density of the AE pulse repetition frequency and amplitude upon the narrow-band filtration deviate from the Poisson and normal laws, respectively. This is related to an asymmetric broadening and the appearance of additional high-intensity peaks caused by the low-frequency voltage pulsations in the dissipative structures. The latter is confirmed by calculations of the autocorrelation functions (ACFs) for the roll velocity oscillations. Indeed, the correlation time τ_c corresponding to the first ACF minimum exhibits extremal growth in the transition regions 1 and 2 (see table). According to [6], this is indicative of the intermittency development in the flux of AE events, which is related to time correlations in the operation of elementary AE sources.

There are grounds to believe that the AE activity of stationary dissipative structures is related to the collective spatial modes corresponding to the formation of large-scale coherent structures. An additional information on the correlation effects accompanying the nonstationary motion of rolls was obtained from an analysis of the distribution function of time intervals (DFTI) between AE pulses. As is seen from Fig. 2c, an increase in the critical parameter is accompanied by a shift of the DFTI center of gravity toward small $\Delta\tau$ values; the shift value exhibits correlation with the type of a stationary dissipative structure. The shape of the $N(\Delta\tau)$ curve for all dissipative structures deviates from exponential, the degree of deviation depending on the control voltage U

Dissipative structures formed during the electroconvection in MBBA liquid crystals

Stationary dissipative structure type	Williams domains (DW)	Fluctuating Williams domains (FDW)	Band texture (GP1)	Dynamic scattering mode 1 (DSM1)	Dynamic scattering mode 2 (DSM2)
Wavevector perturbation scheme	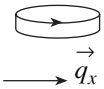	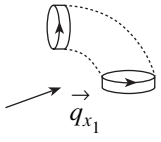	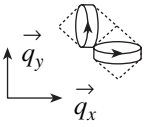		
Threshold voltage U, V	10	15	20	25	30
Characteristic size d, μm	72	36	21	13	6
Correlation time, s	28	48	24	173	21
Modulation in convective roll system		2D–3D convection transition (region 1)		DSM1–DSM2 transition (region 2)	

applied. This fact reflects the presence of a restricted aftereffect in the flux of AE events. The nature of this aftereffect is determined by the degree of correlation in the operation of elementary AE sources, which sharply increases under the intermittency development conditions.

The observed correlation between frequency, amplitude, and time characteristics of AE pulses and the oscillations of convective velocity V allows the AE data to be used for description the self-organization process dynamics during the appearance and evolution of LC dissipative structures. In particular, we may describe the development of a deterministic chaos related to the V oscillations imaged by a stochastic attractor in the phase space. The topological structure of this attractor is characterized by several parameters including the correlation dimension D_c, the maximum Lyapunov index λ_p, and order level P. The values of D_c and λ_p were determined using the time sequences for one coordinate in the phase space according to the Takkens theorem [1]. In the case of a distributed LC system, there arises a problem of selecting a measurable AE parameter related to an essential dynamic variable. As seen from Figs. 2a and 2c, the features of chaotic dynamics in dissipated structures related to the intermittency (space–time correlations) are most pronounced in variations of the AE activity level $\dot{N}$. Accordingly, the fractal structure of the attractor was determined using the time sequences of $\dot{N}(t)$. A quantitative criterion of the degree of stochasticity in the dynamics of dissipative structures during the intermittency and time correlation development in the roll motion (transition regions 1 and 2) was characterized by the order level $P = (m - D_c)/(m - 1)$, where m is the dimension of the attractor embedding. The deviation of the dynamic system statistics from the Gaussian law was characterized by the Hurst parameters H determined from the selected AE observable $\dot{N}(t)$. The H value, describing the persistent properties of the AE flux, increases during the intermittency and aftereffect development.

According to Fig. 3a, the parameters D_c, P, H and λ_p are also correlated with the type of a stationary dissipative structure and exhibit an anomalous behavior with increasing critical parameter. The appearance of fractional D_c values indicates that the dynamics of dissipated structures during the electroconvection in an LC cell with large aspect ratio exhibits a fractal nature. It is important that the value $D_c = 2.9$ (FDW texture) agrees with the value $D_c = 2.6$ reported for a cell with $\Gamma = 2–4$ [7], while the D_c value of the dynamic scattering mode coincides with the vale ($D_c \approx 5.4$) obtained for a isotropic medium ($\Gamma = 1$) under strong unipolar injection conditions [8]. However, in contrast to the case of isotropic distributed systems (where the attractor dimension monotonically increases with the critical

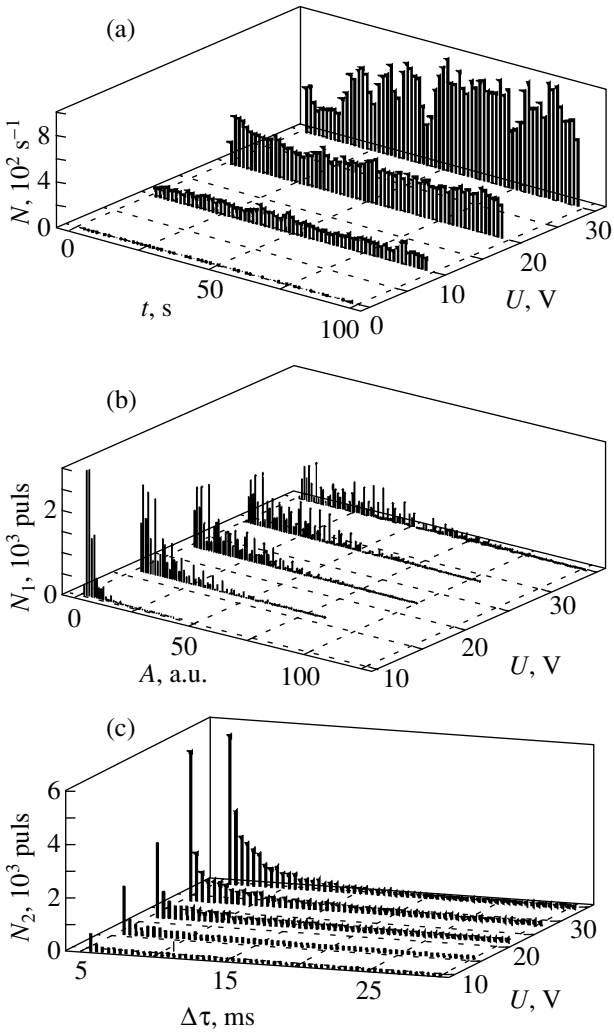

Fig. 2. Variation of the AE flux characteristics with increasing critical parameter: (a) AE activity kinetics; (b) AE pulse amplitude distribution; (c) distribution of time interval between AE pulses. Filtration frequency: 2.50 ± 0.15 kHz.

parameter), the D_c in the mesogenic medium is not only lower (by more than one order of magnitude) but exhibits a drop at a voltage of $U \geq 20$ V. The number of principal harmonics in the Fourier spectrum of the squared intensity of V oscillations coincides with the m value. Therefore, a low-dimensional stochastic ($\lambda_p > 0$) attractor appearing in the phase space of dissipative structures corresponds to a limited number of dynamic variables controlling the motion of the roll ensemble. This result indicates that the chaotic dynamics of dissipative structures is actually determined by a relatively small number of independent large-scale excitations; the other perturbations are dependent, which accounts for the formation of coherent structures.

In the case of a cyclic sweep of the control voltage, the system is characterized by two critical domains (regions 1 and 2) in which the AE parameters and the corresponding statistical moments of higher orders

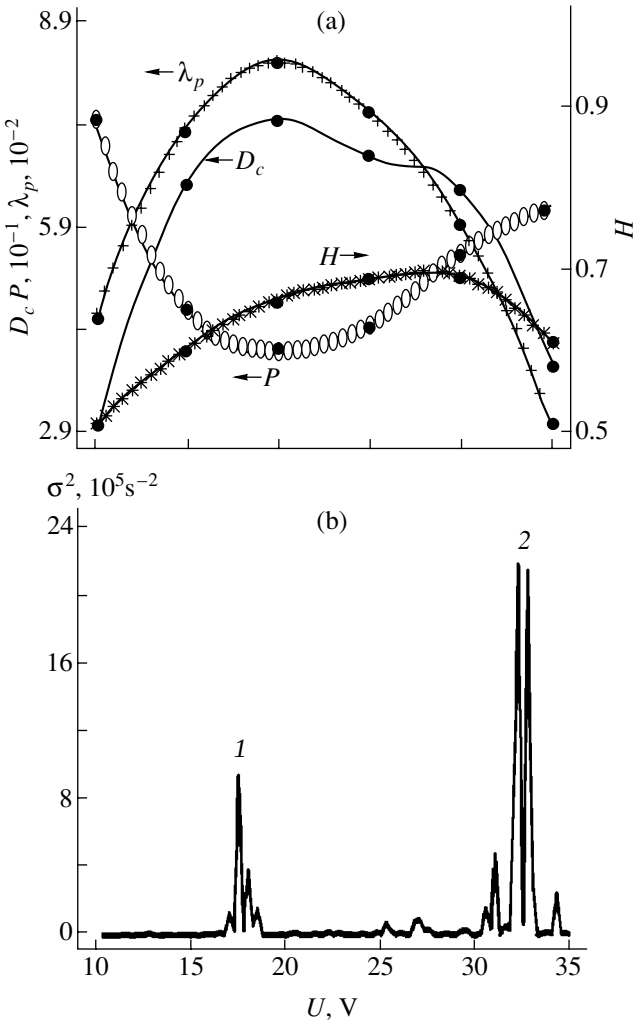

Fig. 3. The pattern of chaotic dynamics of the LC system in the space of AE parameters in the course of transitions between different dissipative structures with increasing critical parameter: (a) anomalous variations of the deterministic chaos characteristics; (b) AE activity dispersion.

exhibit extremal variations (Fig. 3b). These transitions are accompanied by a sharp increase in the correlation time and persistence in the flux of AE events (see table and Fig. 3a), the appearance of a local DFTI minimum (Fig. 2c), a decrease in the number of operative modes, and a low-frequency shift in the AE power spectrum (Fig. 1). These effects are related to qualitative changes in the fractal structure of the stochastic attractor, which reflect a transition between different dissipative structures according to a scenario involving the chaos–chaos intermittency [9].

Thus, the nonstationary motion of rolls in an LC cell with large aspect ratio is a source of the low-frequency narrow-band acoustic emission of a dipole nature. The appearance of collective excitations and the corresponding dipole AE sources during transitions between different dissipative structures accounts for the anomalously high values of dispersion and persistence for the time series of the AE activity, which are indicative of the intermittency development in the field of the convective roll velocities. The AE parameters can be used to elucidate a scenario of the chaotization process observed on increasing the critical parameter in an ensemble of convective rolls.

REFERENCES

1. M. C. Cross and P. C. Hohenberg, Rev. Mod. Phys. **65** (3), **851** (1993).
2. A. P. Kapustin and O. A. Kapustina, *Acoustics of Liquid Crystals* (Nauka, Moscow, 1986).
3. E. Axelrod, V. Bespalov, A. Kuzmin, *et al.*, Mol. Cryst. Liq. Cryst. **302** (3), 363 (1997).
4. H. Miike, S. Ikemoto, K. Ochiai, *et al.*, Jpn. J. Appl. Phys. **23** (6), L379 (1984).
5. L. D. Landau and E. M. Lifshitz, *Course of Theoretical Physics*, Vol. 6: *Fluid Mechanics* (Nauka, Moscow, 1986; Pergamon, New York, 1987).
6. Ya. B. Zel'dovich, S. A. Molchanov, and A. A. Ruzmaĭkin, Usp. Fiz. Nauk **152** (1), 3 (1987) [Sov. Phys. Usp. **30**, 353 (1987)].
7. Y. Hidaka, H. Orihara, and Y. Ishibashi, J. Phys. Soc. Jpn. **61** (11), 3950 (1992).
8. B. Malraison, P. Atten, and P. Berge, J. Phys. Lett. **44** (22), 897 (1983).
9. V. S. Anishchenko and A. B. Neĭman, Pis'ma Zh. Tekh. Fiz. **13** (17), 1063 (1987) [Sov. Tech. Phys. Lett. **13**, 444 (1987)].

Translated by P. Pozdeev

Technical Physics Letters, Vol. 27, No. 7, 2001, pp. 533–535. Translated from Pis'ma v Zhurnal Tekhnicheskoĭ Fiziki, Vol. 27, No. 13, 2001, pp. 10–15.

The Shock-Wave Synthesis of Ultradisperse Chromium-Doped Alumina Powder

Im Tkhek-de, N. E. Lyamkina, A. I. Lyamkin, O. P. Podavalova, V. V. Slabko*, and G. A. Chiganova

Krasnoyarsk State Technical University, Krasnoyarsk, Russia

** e-mail: slabko@kgtu.runnet.ru*

Received December 20, 2000

Abstract—An ultradisperse alumina (Al_2O_3) powder doped with Cr^{3+} ions was synthesized for the first time by shock-wave loading of a mixture of aluminum powder and ammonium chromate. The synthesized powder is composed primarily of the chromium-doped α- and δ-Al_2O_3 particles. The luminescence spectra of the α phase are identical to those of a macroscopic ruby crystal sample, which indicates that chromium atoms are incorporated into the alumina lattice. The Cr^{3+}-doped δ-Al_2O_3 modification represents a new optical material.

The development of new methods for obtaining optical materials is an important direction of research in materials science. Of considerable interest are powdered materials doped with the ions of chemical elements widely used as activators in the synthesis of luminophors and activated laser crystals. The group of most widely used activators includes the ions of transition metals, rare-earth elements, and actinides.

The physicochemical and optical characteristics of powdered materials depend on the method of synthesis. In recent years, intensively developed were the dynamic methods of powder synthesis. The ultradisperse materials obtained by these methods frequently exhibit unusual combinations of physicochemical properties. The optical characteristics of such powders doped with various activators may also differ from those of their usual counterparts obtained by the traditional methods. In particular, it was of interest to study the properties of small (several dozen Ångströms in size) particles of alumina (Al_2O_3) doped with chromium. These particles represent the so-called objects of low dimensionality.

The method used to obtain an ultradisperse alumina powder consists essentially in a shock-wave loading of a powdered porous aluminum layer contacting with a charge of an explosive, which leads to heating and ejecting the material into a reactive atmosphere. When a metal powder possessing a high initial porosity is employed, the layer of a shock-wave loaded material is heated to very high temperatures. The material particles flying out interact with gases in the reactor chamber to form an ultradisperse Al_2O_3 [1]. In this study, we used the shock-wave loading method to obtain an alumina powder doped with Cr^{3+} ions.

An experimental unit represented a cylindrical charge of explosive (free-poured hexogen powder) surrounded with a layer comprising a mixture of aluminum powder (PAP-1 grade) and ammonium chromate (6 wt % of the total mixture). The initial ammonium chromate to aluminum ratio was selected so as to provide for the chromium ion content of 3% in the product (for a maximum possible degree of chromium substitution for aluminum in the crystal matrix). The total powder layer in the charge was 20 mm. Since the process aimed at incorporating atomic chromium into the aluminum oxide lattice, the use of metal chromium or chromium oxide (refractory substances) in the initial mixture was unexpedient. Study of the luminescence spectra of a powder prepared using chromium oxide (Cr_2O_3) as a source of the dopant showed that chromium atoms were not incorporated into the aluminum oxide lattice.

The synthesis was effected in a hermetic explosion chamber filled with air. The selection of ammonium chromate $(NH_4)_2CrO_4$ as the dopant source is explained by the fact that this compound heated to 200°C in air vigorously burns with the formation of chromium oxide molecules [2]:

$$(NH_4)_2CrO_4 \longrightarrow Cr_2O_3.$$

The resulting chromium oxide molecules flying after the explosion are capable of reacting either with Al_2O_3 to form a mixed oxide compound or with aluminum (alumothermal reduction process) to yield atomic chromium:

$$Cr_2O_3 + 2Al = Al_2O_3 + 2Cr.$$

This chromium is capable of partly replacing aluminum atoms during the formation of aluminum oxide. It was expected that the shock-wave loading of the mixture of aluminum powder and ammonium chromate would

1063-7850/01/2707-0533$21.00 © 2001 MAIK "Nauka/Interperiodica"

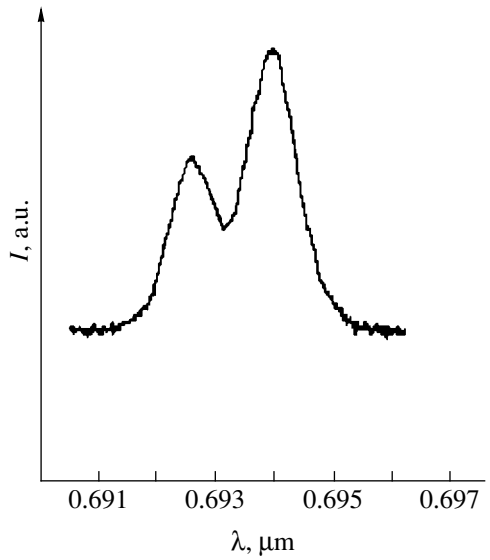

Fig. 1. The luminescence spectrum of an aqueous suspension of the coarse fraction of a chromium-doped alumina powder.

provide conditions for the incorporation of chromium ions into the crystal lattice of aluminum oxide.

A powder synthesized as described above was separated by elutriation into coarse and fine fractions. The former readily precipitated fraction accounted for ≈20% of the total product and consisted predominantly of shapeless particles with an average size of ~200 μm, representing agglomerates of smaller species. After drying, the coarse fraction exhibited pink color. The fine fraction was characterized by an average particle size of ~0.2 μm; upon drying, this powder exhibited a greenish tint.

According to the data of Beloshapko *et al.* [1, 3], the ultradisperse powder obtained by the shock-wave loading of a porous aluminum layer (free of dopants) is composed of aluminum oxide (α and δ modifications) and a nitride-containing oxide phase where oxygen is partly replaced by nitrogen. The α-Al_2O_3 phase (corundum) enters predominantly into the coarse fraction. The fine fraction contains predominantly a metastable δ-Al_2O_3 and an oxynitride phase of the $A_{(8/3 + x/3)}O_{4-x}N_x$ type with $0.22 < x < 0.5$.

The observed difference in the colors of coarse and fine chromium-doped alumina fractions can be explained as follows. Upon the Cr^{3+} ion incorporation into the corundum lattice, the coarse fraction consisting predominantly of α-Al_2O_3 acquires the characteristics analogous to those of a pink ruby crystal. Since the energy levels of an activator ion depend on the crystal matrix, the δ-Al_2O_3 doped with Cr^{3+} ions will possess modified spectral characteristics and exhibit a color different from that of the ruby crystal. The experimental evidence of the presence of chromium atoms incorporated into the aluminum oxide crystal lattice was obtained by method of luminescent analysis.

The ruby crystals that are frequently employed as the active elements of lasers are usually grown from a melted mixture of Cr_2O_3 and Al_2O_3. These crystals (α phase) possess a hexagonal rhombohedral crystal lattice. The well known luminescence spectrum of a ruby crystal contains two sharp lines corresponding to transitions from the $\bar{E}$ and $2\bar{A}$ levels to the ground $^4A_2$ level. According to [4], the centers of lines measured at 300 K are located at λ = 0.6943 μm (R_1 line) and 0.6928 μm (R_2 line).

In order to verify the above assumption that optical characteristics of the α modification are identical to those of a ruby crystal, we attempted at obtaining a luminescence spectrum of the synthesized powder. The spectra were excited by a quasi-continuous second harmonic radiation from a Nd^{3+}:YAG laser with λ = 0.530 μm, which falls within one of the broad absorption bands of the spectrum of ruby.

The samples were either prepared as aqueous suspensions with a powder concentration of about 0.5% or measured in the form of a dry powder layer with a thickness of 100 μm pressed between two optical glass plates. As noted above the α-Al_2O_3 phase enters predominantly into the coarse fraction of the synthesized powder. The luminescence spectrum of an aqueous suspension of the coarse fraction of the chromium-doped alumina powder is presented in Fig. 1.

The finely disperse powder fraction consists predominantly of the chromium-activated δ-Al_2O_3 modification and contains almost no α-Al_2O_3 phase. Our attempts at measuring the luminescence spectrum of this fraction excited with the second harmonic radiation from the neodymium laser were unsuccessful. This indicated that the spectrum of the chromium-doped δ-Al_2O_3 differed from the spectrum of ruby so that the exciting radiation employed did not fall within the absorption band of the sample. As is known, the δ-Al_2O_3 phase possesses a hexagonal crystal lattice with a density of $d = 2.4$ g/cm^3. Heated to 950°C, the δ phase transforms into a hexagonal α phase with $d = 3.99$ g/cm^3 [5]. The finely disperse fraction was heated to 1200°C and treated at this temperature for half an hour. Upon heating, the sample color changed to pink. The luminescence spectrum of such a heat-treated sample (measured as dry powder) is presented in Fig. 2.

A comparison of Figs. 1 and 2 shows that the two spectra are qualitatively similar, containing two rather sharp closely spaced lines with λ = 0.6943 and 0.6928 μm. A comparison to the data for ruby [4] indicates that the luminescence spectrum of a finely disperse chromium-activated alumina powder synthesized by the method of shock-wave loading is similar to the spectrum of ruby.

Thus, the proposed method of shock-wave loading allows a finely disperse alumina powder with atomic

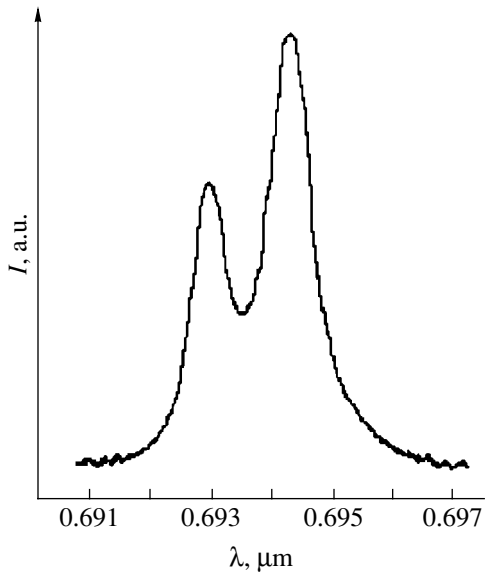

Fig. 2. The luminescence spectrum of the finely disperse chromium-doped alumina powder fraction (dry sample) measured after a thermal treatment.

chromium incorporated into the aluminum oxide crystal lattice. It should be noted that the luminescence spectra of some of the synthesized samples displayed additional emission bands not observed in the spectra of macroscopic crystals. Investigation of these bands and the corresponding optical emission mechanism is of special importance since we may deal with a difference between the ultradisperse and macroscopic state of the crystal. It is known that the δ-Al_2O_3 phase is unstable and does not exist in a macroscopic form. To our knowledge, the spectrum of the impurity states of chromium incorporated into this phase was never reported. Therefore, a study of the absorption and luminescence spectra of this crystal modification is of large independent interest.

REFERENCES

1. A. G. Beloshapko, A. A. Bukaemskiĭ, and A. M. Staver, Fiz. Goreniya Vzryva **26** (4), 93 (1990).
2. H. Remy, *Lehrbuch der anorganischen Chemie* (Geest und Portig, Leipzig, 1960; Mir, Moscow, 1974).
3. A. G. Beloshapko, A. A. Bukaemskiĭ, I. G. Kuz'min, T. P. Terent'eva, and G. A. Chiganova, in *Superdispersed Materials. Production and Properties. Interuniversity Collection* (Krasnoyarskiĭ Politekh. Inst., Krasnoyarsk, 1990), p. 91.
4. P. Görlich, H. Karras, G. Kötitz, and R. Lehmann, Phys. Status Solidi **5** (3), 437 (1964); **6** (2), 277 (1964).
5. *Physicochemical Properties of Oxides: A Handbook* (Metallurgiya, Moscow, 1978).

Translated by P. Pozdeev

Technical Physics Letters, Vol. 27, No. 7, 2001, pp. 536–537. Translated from Pis'ma v Zhurnal Tekhnicheskoĭ Fiziki, Vol. 27, No. 13, 2001, pp. 16–21.

Dispersion Characteristics of Slot and Microstrip Lines Based on Ferroelectric Film–Dielectric Substrate Structures

I. G. Mironenko and A. A. Ivanov

University of Electrical Engineering, St. Petersburg, Russia

e-mail: mit@eltech.ru, MironencoIG@rambler.ru, iva@solaris.ru

Received February 4, 2001

Abstract—The propagation constant is analyzed numerically for electromagnetic waves supported by slot and microstrip lines. The results obtained can be used in designing microwave transmission lines and planar devices based on ferroelectric films. © *2001 MAIK "Nauka/Interperiodica"*.

Nonlinear properties of ferroelectric materials are widely exploited in the microwave technology [1]. The interest in the dispersion characteristics of planar transmission lines based on ferroelectric film–dielectric substrate (FF–DS) structures is stimulated mainly by the fact that the electromagnetic wave propagation constant in these structures depends on the FF permittivity, which determines the design of these lines with controlled characteristics. Figure 1 shows a schematic diagram of the shielded slot and microstrip lines implemented in an FF–DS structure. In this paper, we analyze numerically the propagation constants of the main electromagnetic modes in such lines as functions of the FF thickness and permittivity in the frequency band of most practical interest. The analysis is performed within the framework of the full-wavelength model, which most adequately describes hybrid electromagnetic waves in planar transmission lines.

A hybrid electromagnetic wave in a transmission line is a superposition of *LE* and *LM* waves. Therefore, let us specify the Hertz vectors using the magnetic and electric potentials

$$\dot{\mathbf{A}} = \mathbf{e}_y A(x, y)\exp(-j(\gamma z - \omega t)),$$

$$\dot{\mathbf{F}} = \mathbf{e}_y F(x, y)\exp(-j(\gamma z - \omega t)),$$

respectively, where γ is the propagation constant for the electromagnetic waves in the line. In each cross section of the line (Fig. 1), the Fourier transforms (FTs) of the potentials $\bar{A}_i(y, s)$ and $\bar{F}_i(y, s)$ satisfy the equation

$$\left(\frac{\partial^2}{\partial y^2} + \alpha_i^2\right)\begin{Bmatrix}\bar{A}_i(y, s)\\ \bar{F}_i(y, s)\end{Bmatrix} = 0, \qquad (1)$$

where $\alpha_i = \sqrt{(s^2 + \gamma^2 - k^2\varepsilon_i)}$ and $k^2 = \omega^2\varepsilon_0\mu_0$ is the propagation constant in the free space.

The propagation constant is determined as follows.

(i) The FTs of the potentials are found from Eq. (1).

(ii) The FTs of the tangential components of the electric and magnetic field intensities in the plane $y = 0$ are calculated using the FTs of the potentials.

(iii) Matching the E_x, E_z, H_x, and H_z components across a slot yields a pair of integral equations for the electric field intensity in the slot.

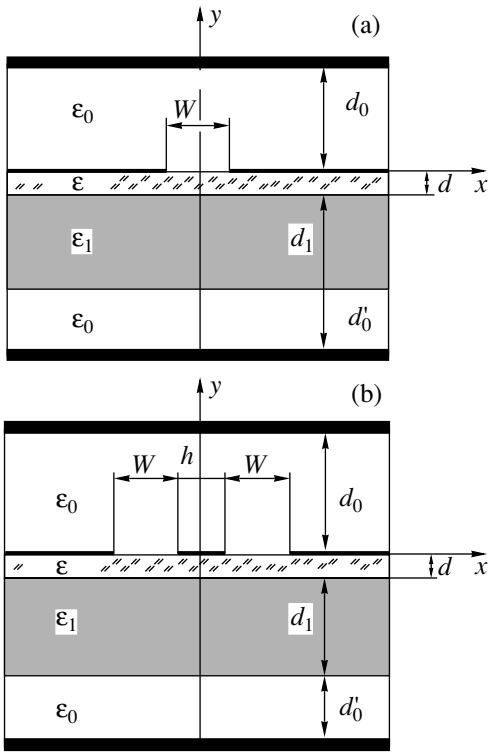

Fig. 1. Cross sections of (a) slot and (b) microstrip transmission lines: ε and d are the FF permittivity and thickness, ε_1 and d_1 are the DS permittivity and thickness, ε_0 is the permittivity of vacuum, and d_0 and d_0' are the distances to the shields.

1063-7850/01/2707-0536$21.00 © 2001 MAIK "Nauka/Interperiodica"

(iv) Expanding the fields in the slots in the Chebyshev polynomials [2, 3] and applying the Galerkin method reduces the integral equations to an infinite system of algebraic equations for the unknown expansion coefficients a_n and b_m and the propagation constant

$$\begin{aligned}\sum_{n=0,1,2}^{\infty} a_n K^{11}_{p,n}(\gamma, s) + \sum_{m=1,2}^{\infty} b_m K^{12}_{p,m}(\gamma, s) &= 0,\\ \sum_{n=0,1,2}^{\infty} a_n K^{21}_{q,n}(\gamma, s) + \sum_{m=1,2}^{\infty} b_m K^{22}_{q,m}(\gamma, s) &= 0,\end{aligned} \quad (2)$$

where

$$K^{11}_{p,n}(\gamma, s) = (-1)^{n+p}\int_0^{\infty} J_{2p}\left(\frac{sw}{2}\right) f_{11}(s, \gamma) J_{2n}\left(\frac{sw}{2}\right) ds$$

for the slot line and

$$K^{11}_{p,n}(\gamma, s) = (-1)^{n+p}\int_0^{\infty} J_{2p}\left(\frac{sw}{2}\right) f_{11}(s, \gamma) \times J_{2n}\left(\frac{sw}{2}\right)\sin\left(\frac{s(w+h)}{2}\right) ds$$

for the coplanar line ($K^{12}_{p,m}$, $K^{21}_{q,n}$, and $K^{22}_{q,m}$ are given by analogous expressions); $J_\nu(z)$ are the Bessel functions of the first kind; and $f_{11}(s, \gamma)$ (as well as $f_{12}(s, \gamma)$, $f_{21}(s, \gamma)$, and $f_{22}(s, \gamma)$ involved in the corresponding integrals) is a function depending only on the cross section dimensions and permittivities of the layers.

(v) The condition for the determinant of system (2) to be zero yields the equation for the propagation constant γ.

Figures 2a and 2b present the propagation constants calculated for the slot and microstrip lines. Using the product (εd) as the abscissa, we can find γ for FF thicknesses in the range $0 \le d \le 5 \times 10^{-3}$ mm and permittivities $\varepsilon \le 2.5 \times 10^3$. The calculations are performed for a DS with $d_1 = 0.34$ mm and $\varepsilon_1 = 9.5$ at 30 GHz. The shield effect is negligible at $d_0 = d_0' \ge 5$ mm. The calculation error estimated from the convergence of integrals in Eq. (2) does not exceed fractions of a percent.

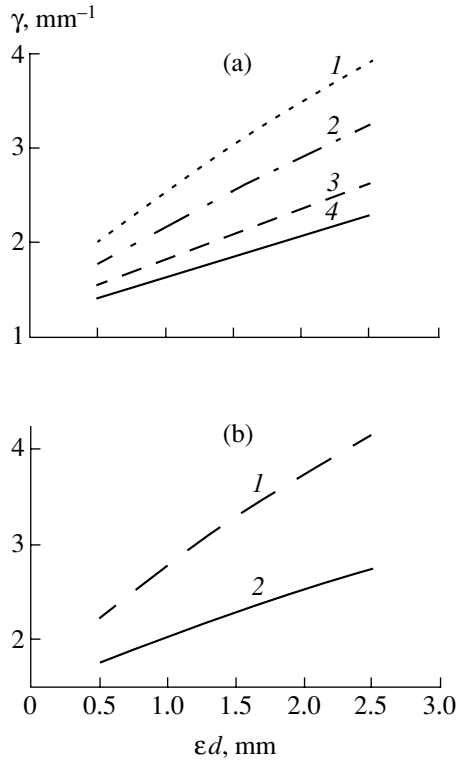

Fig. 2. (a) The propagation constant in the slotted line: w = 0.05 (*1*), 0.1 (*2*), 0.25 (*3*), and 0.5 mm (*4*). (b) The propagation constant in the coplanar line: (*1*) w = 0.05 mm, h = 0.1 mm; (*2*) $w = h$ = 0.05 mm.

The results obtained allow us to conclude that slot and microstrip lines formed on the FF surface ensure the propagation of desired slow waves and the efficient control of the propagation constant provided by the FF permittivity variation.

REFERENCES

1. Integr. Ferroelectr. **22** (1998).
2. K. C. Gupta, R. Garg, I. Bahl, and P. Bhartia, *Microstrip Lines and Slotlines* (Artech, Boston, 1996).
3. T. Itoh, IEEE Trans. Microwave Theory Tech. **MTT-28** (7), 733 (1980).

Translated by I. Efimova

Technical Physics Letters, Vol. 27, No. 7, 2001, pp. 538–541. Translated from Pis'ma v Zhurnal Tekhnicheskoĭ Fiziki, Vol. 27, No. 13, 2001, pp. 22–29.

A Photorefractive Effect Accompanying the Acoustooptical Interaction in Gyrotropic Cubic Crystals in the Presence of an Alternating Electric Field

G. V. Kulak

Mozyr State Pedagogical Institute, Mozyr, Belarus

e-mail: mozinst@mail.ru

Received December 4, 2000

Abstract—A photorefractive effect in gyrotropic cubic crystals is considered. The effect accompanies the Bragg diffraction of light by an ultrasound in the presence of an alternating electric field. The possibility of recording holographic gratings with the help of the light waves diffracted by traveling ultrasonic waves is demonstrated. The amplitude of the index phase grating is studied as a function of the intensity of the recording ultrasound, the length of the region of acoustooptical interaction, and the specific rotation of the crystal. © *2001 MAIK "Nauka/Interperiodica".*

Specific features of the recording and reading of optical holographic gratings (HG) formed in cubic crystals demonstrating a linear electrooptic effect and gyrotropic properties were studied in [1–3]. It was found that the gyrotropic properties of crystals of the sillenite type may substantially change selective and polarization characteristics of the light beams diffracted by holographic phase gratings. Shepelevich *et al.* [3] determined the crystal cuts and external electric field orientations optimizing the output energy characteristics of optical HGs. Previously [4], we studied the energy and polarization features of the acoustooptical (AO) Bragg diffraction in gyrotropic cubic crystals and derived expressions for the complex vector amplitudes of the zero- and first-order diffracted fields.

The acoustooptical memory effect in photorefractive (PR) crystals attracts considerable interest of researchers because this phenomenon can be used for creating various devices recording acoustic signals by optical methods [5, 6]. Of both theoretical and practical interest is utilizing optical methods for recording and reading acoustic signals in PR crystals such as sillenites ($Bi_{12}SiO_{20}$, $Bi_{12}GeO_{20}$, $Bi_{12}TiO_{20}$, etc.). These crystals are transparent in the visible spectral range and demonstrate a rather strong electrooptic effect. Unlike well-known uniaxial ferroelectric crystals ($LiNbO_3$, $LiTaO_3$, $BaTiO_3$, etc., see [1]), sillenites are optically isotropic materials with characteristics more suitable for the reversible recording and reading of HGs [7]. A theoretical and experimental study of the PR effect arising during the interference of light beams of the same frequency which result from the Raman–Nath AO diffraction of light by standing ultrasonic waves in a static electric field was performed by Berezhnoĭ and Sherstneva [8]. However, specific features of the process governing the PR grating recording in traveling ultrasonic waves have not yet been investigated. These gratings cannot be recorded in the presence of a static electric field [9, 10].

In this paper, we consider the recording of the HR gratings in gyrotropic cubic crystals by the light waves of various frequencies diffracted in the Bragg mode by traveling ultrasonic waves in the presence of an alternating electric field.

Let an ultrasonic wave with the displacement vector $\mathbf{U} = \mathbf{U}_0\exp[i(\mathbf{K}z - \Omega t)]$ (where $\mathbf{K} = \Omega/v$ and Ω is the cyclic frequency of the wave) propagate along the [111] axis of a gyrotropic cubic crystal. Below, we assume that the AO diffraction plane coincides with the *YZ*-plane obtained after the following rotations: (1) the initial crystal coordinate system $X_1X_2X_3$ is rotated through 45° about the OX_3-axis and (2) the obtained coordinate system $X'Y'Z'$ is rotated through angle $\theta = \arcsin\sqrt{2/3}$ about the OY'-axis until the OZ'-axis coincides with direction [111] (Fig. 1). Consider the noncollinear AO interaction of the light waves propagating at the Bragg angle (φ_B) with respect to the OY'-axis. The light diffracted by the traveling ultrasonic wave consists of light beams with the complex vector amplitudes $\mathbf{E}_0$ and $\mathbf{E}_1$ and different frequencies ω and $\omega \pm \Omega$ (for the anti-Stokes and Stokes AO diffraction, respectively). In the region confined by planes $y = 0$ and $y = l$, the beams intersect to form a distribution of the light intensity (the interference pattern), whose contrast m varies with the frequency Ω of the ultrasonic wave. Under these conditions [9, 10], recording static holographic gratings is only possible if an alternating electric field E^e with a frequency equal to the difference of the frequencies of the two recording beams (i.e., $E^e = E_0^e\cos\Omega t$, where

1063-7850/01/2707-0538$21.00

Ω is assumed to be much greater than τ_{sc}^{-1}, τ_{sc} being the time required for recording a hologram in the PR crystal) is applied to the crystal in the direction of the grating wavevector **K** [10]. This causes a stationary photocurrent $j \sim E^e(\mathbf{E}_0\mathbf{E}_1^*) \sim \exp(\mp i\Omega t)\exp(-i\omega t)\exp[i(\omega \pm \Omega)t]$ + c.c. flowing in the crystal in the direction of the wavevector $\mathbf{K} \parallel OZ$. The PR grating is formed by two light waves diffracted by the ultrasound ($\mathbf{E}_0 = \mathbf{E}_0^0\exp[i(\mathbf{k}_0\mathbf{r} - \omega t)]$ and $\mathbf{E}_1 = \mathbf{E}_1^0\exp\{i[\mathbf{k}_1\mathbf{r} - (\omega \pm \Omega)t]\}$) and the low-frequency electric field $E^e \sim E_0^e\exp(\mp i\Omega t)$. Under these conditions, the spatial component of the photocurrent j is proportional to $\exp(\pm i\mathbf{Kr})$. The spatially periodic stationary photocurrent leads to the charge separation in the PR crystal and the formation of an index grating [1, 9, 10]. It should be noted that, for the chosen direction of the ultrasonic wave, the piezoelectric effect is small (see [11]); therefore, the acoustophotorefractive holographic gratings recorded due to the electron bunching effect can be neglected [5, 6]. In view of the results presented in [4], distribution $I = (\mathbf{E}_0 + \mathbf{E}_1)(\mathbf{E}_0 + \mathbf{E}_1)^*$ of the light intensity in the region of intersection of the diffracted light beams is given by the relationships

$$I = I_0 + I_0\left[\frac{1}{2}m\exp(iKx) + \text{c.c.}\right], \qquad (1)$$

where I_0 is the total light intensity, $m = m_0\exp(-i\Omega t)$, and m_0 is the amplitude of the interference pattern modulation. The light intensity I_0 and amplitude m_0 are given by the relationships

$$I_0 = I_1 + I_2 + I_3 + I_4, \quad m_0 = (\sqrt{I_1 I_3} + \sqrt{I_2 I_4})/I_0, \qquad (2)$$

where

$$\begin{aligned}
I_1 &= [R_1\sin(a_1 l) + \tilde{R}_1\sin(a_2 l)A_\parallel \\
&\quad - Q(\cos(a_2 l) - \cos(a_1 l))A_\perp]^2, \\
I_2 &= [\underline{R}_1\sin(a_1 l) + \tilde{\underline{R}}_1\sin(a_2 l)A_\perp \\
&\quad + Q(\cos(a_2 l) - \cos(a_1 l))A_\parallel]^2, \\
I_3 &= [(S_0\cos(a_1 l) + \tilde{S}_0\cos(a_2 l))A_\parallel \\
&\quad + (L_0\sin(a_1 l) + \tilde{L}_0\sin(a_2 l))A_\perp], \\
I_4 &= [(\underline{S}_0\cos(a_1 l) + \tilde{\underline{S}}_0\cos(a_2 l))A_\perp \\
&\quad - (L_0\sin(a_1 l) + \tilde{L}_0\sin(a_2 l))A_\parallel].
\end{aligned} \qquad (3)$$

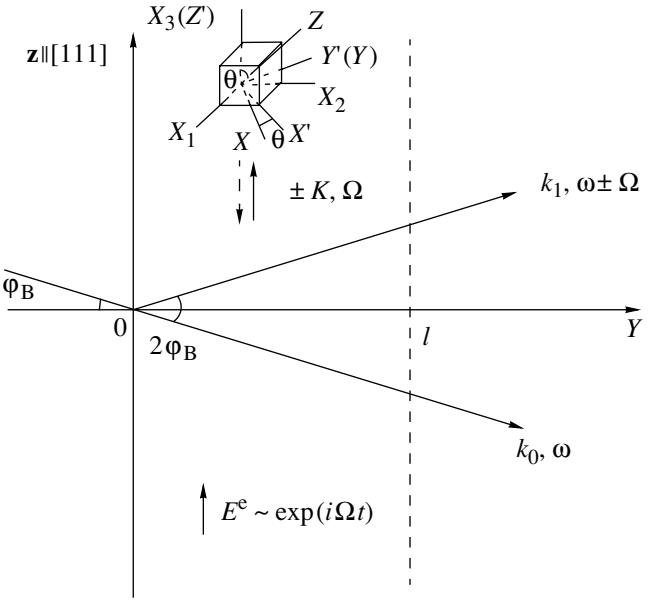

Fig. 1. Layout of the acoustooptical recording of the holographic grating in the process of the Bragg diffraction of light by an ultrasound in the presence of an alternating electric field.

The following notations were introduced:

$$Q = \frac{\rho(\chi_\parallel + \chi_\perp)}{(a_1^2 - a_2^2)}, \quad R_1 = \frac{\chi_\parallel(2\rho^2 + \chi_\parallel^2 - a_2^2 + \rho^2\chi_\perp/\chi_\parallel)}{a_1(a_1^2 - a_2^2)},$$

$$L_0 = \frac{\rho(\rho^2 + \chi_\parallel^2 + \chi_\perp^2 - a_2^2 + \chi_\perp\chi_\parallel)}{a_1(a_1^2 - a_2^2)},$$

$$S_0 = \frac{(\rho^2 + \chi_\parallel^2 - a_2^2)}{(a_2^2 - a_1^2)}, \qquad (4)$$

$$a_{1,2} = \left\{\left(\rho^2 + \frac{1}{2}\chi_\parallel^2 + \frac{1}{2}\chi_\perp^2\right)\right.$$

$$\left.\pm\left[\left(\rho^2 + \frac{1}{2}\chi_\parallel^2 + \frac{1}{2}\chi_\perp^2\right)^2 - (\rho^2 - \chi_\parallel\chi_\perp)^2\right]^{1/2}\right\}^{1/2},$$

where

$$\chi_\parallel = -\pi n^3 p_{\text{eff}}^\parallel\sqrt{2I_a/\sigma v^3}/2\lambda,$$

$$\chi_\perp = -\pi n^3 p_{\text{eff}}^\perp\sqrt{2I_a/\sigma v^3}/2\lambda,$$

I_a is the intensity of the ultrasonic wave, σ is the density of the PR crystal, n is the refractive index of the medium, λ is the wavelength of the incident light in vacuum, v is the phase velocity of the ultrasonic wave, $p_{\text{eff}}^\parallel$ and $p_{\text{eff}}^\perp$ are the effective photoelastic constants, and ρ is the specific rotation of the crystal. For the con-

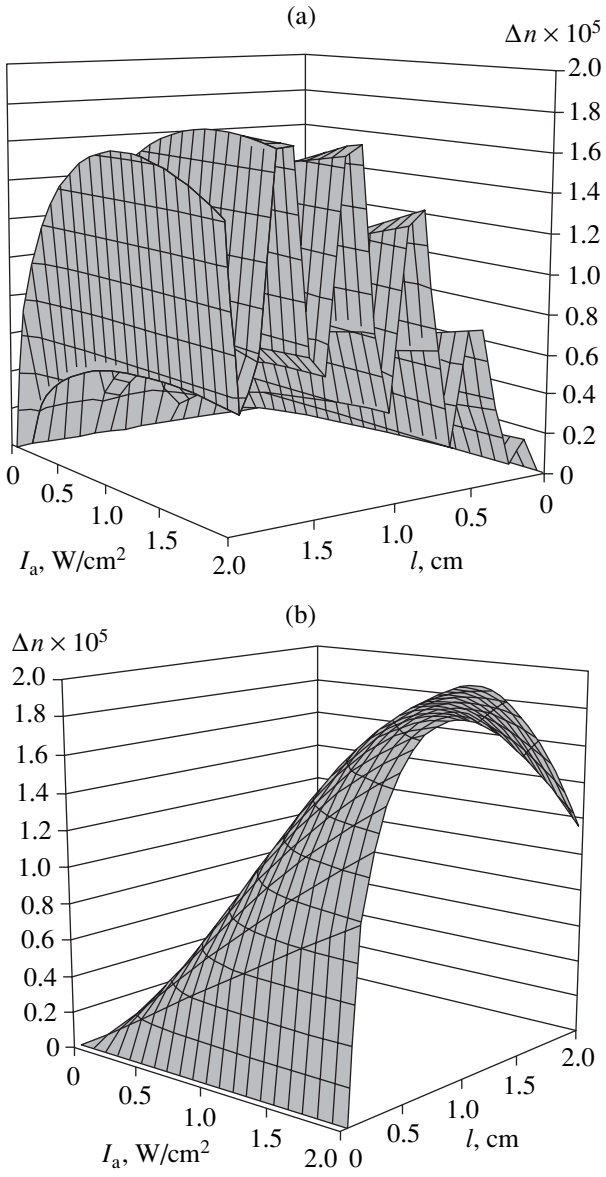

Fig. 2. Amplitude Δn of the index grating vs. the intensity I_a of an ultrasonic wave and the length l of the AO interaction for $\rho = 3.8$ (a) and 0 (b) cm^{-1} at $f = 0.1$ GHz, $N_A = 2 \times 10^{20}$ m^{-3}, $E_0^e = 5$ kV/cm, $A_\perp = 0$, and $A_\parallel = 1$.

figuration of the diffraction process under study, $p_{eff}^{\parallel} = \frac{1}{3}(p_{11} + p_{12} + p_{21} + 4p_{44})$ and $p_{eff}^{\perp} = \frac{1}{3}(p_{11} + p_{12} + p_{21} - 2p_{44})$, where p_{ij} are the components of the tensor of photoelastic constants. The top and bottom tildes in formulas (3) designate the following respective changes in expressions (4): $a_1 \Leftrightarrow a_2$ and $\chi_\parallel \Leftrightarrow \chi_\perp$; coefficients $A_\parallel$ and $A_\perp$ are the amplitudes of the *p*- and *s*-polarized components of the recording light.

In order to describe the hologram formation processes, we use a model of the PR grating proposed in [9, 10, 12]. According to this model, the expression for the electric field E_{sc} of a PR holographic grating has the form

$$E_{sc} = \frac{m_0 E_q E_\mu \{[(E_\mu + E_D)^2 + E_0^{e^2}]^{1/2} - E_\mu - E_D\}}{E_0^e \{[(E_\mu + E_D)^2 + E_D^2]^{1/2} + E_q - E_\mu\}}, \quad (5)$$

where $E_D = Kk_BT/e$ is the diffuse field, $E_q = eN_A/\varepsilon K$ is the space charge saturation field, $E_\mu = 1/\tau K\mu$ is the drift field, e is the absolute value of the electron charge, ε is the permittivity, τ is the lifetime of charge carriers, μ is the electron mobility in the crystal, T is the absolute temperature, and N_A is the concentration of acceptors in the forbidden band of the crystal. It should be noted that the HG recording process cannot be rigorously analyzed without using formulas (1)–(4), which ensure a correct account of the influence of the crystal gyrotropic properties on the diffraction pattern formation.

Field E_{sc} of the PR grating forms a static phase grating with the tensor of permittivity perturbations $\Delta\varepsilon_{il} = -n^4 r_{ilt} E_{sct}$ (where r_{ilt} are the components of the tensor of electrooptic constants). In the *XYZ* coordinate system, $\Delta\varepsilon_{11} = \Delta\varepsilon$, $\Delta\varepsilon_{22} = \Delta\varepsilon$, and $\Delta\varepsilon_{33} = -2\Delta\varepsilon$, where $\Delta\varepsilon = \frac{1}{2} n^3 r_{41}(E_{sc}/\sqrt{3})$. The amplitude of the index grating (the PR grating) is given by the relationship $\Delta n = \Delta\varepsilon/2n$ [1].

Numerical calculations were performed for bismuth silicate ($Bi_{12}SiO_{20}$) at the incident light wavelength $\lambda = 0.63$ μm and the carrier lifetime $\tau \approx 10^{-5}$ s. This crystal has been chosen because of its unique photorefractive and gyrotropic properties [1, 7].

Figure 2a depicts the surface $\Delta n(l, I_a)$ representing a nonuniform distribution of the HG amplitude across the wave vector **K**. The nonlinear behavior of the amplitude Δn of the PR grating modulation as a function of parameters l and I_a is caused by the specific features of the strong AO interaction in gyrotropic crystals [4]. If the gyrotropic properties are "disabled" (Fig. 2b), the grating amplitude changes substantially. These features of the PR grating recording process can be explained by the combined effect of the circular anisotropy of the crystal under consideration and the anisotropy of its photoelasticity on the AO interaction. Thus, using a gyrotropic crystal with *s*- or *p*-polarized incident light beams and varying the AO interaction length l or the intensity I_a of the ultrasonic wave, one may increase or decrease the diffraction efficiency in comparison with that of a nongyrotropic crystal (with $\rho = 0$) [4].

Features related to the influence of the external field E_0^e and the ultrasound frequency f on the grating amplitude follow from expression (5). It was established [1, 10] that, for PR crystals of the sillenite type, the field amplitude E_{sc} increases with the external field E_0^e and decreases with increasing the grating wave vector **K** (or the ultrasound frequency $f \sim |\mathbf{K}|$). It should be noted,

however, that the low-frequency boundary of the recording AO wave is limited by the Bragg AO diffraction conditions ($f \geq (0.6nv^2/\lambda l)^{1/2}$) [13].

The considered relationships show that gyrotropic cubic crystals such as sillenites can be successfully used for recording PR gratings with the help of the light waves diffracted in the Bragg mode by traveling ultrasonic waves. The recording is possible at moderate levels of the acoustic power and acceptable intensities of the external electric field. In comparison to other crystals, sillenites are real-time reversible crystals which are highly sensitive to the recording light. They allow recording signals and images with high contrast and ensures a high-resolution reproduction of the recorded data [7].

Acknowledgments. I am grateful to V.N. Belyĭ for the fruitful discussion of results.

This work was supported by the Belarus Republic Foundation for Basic Research, project no. F99-135.

REFERENCES

1. M. P. Petrov, S. I. Stepanov, and A. V. Khomenko, *Photorefractive Crystals in Coherent Optics* (St. Petersburg, 1992).
2. M. P. Petrov, A. V. Shamraĭ, V. M. Petrov, and I. Zoubulis, Fiz. Tverd. Tela (St. Petersburg) **39** (11), 1990 (1997) [Phys. Solid State **39**, 1779 (1997)].
3. V. V. Shepelevich, Y. Hy, A. Firsov, *et al.*, Appl. Phys. B: Lasers Opt. **B68** (5), 923 (1999).
4. G. V. Kulak and S. N. Kovchur, Opt. Spektrosk. **83** (6), 981 (1997) [Opt. Spectrosc. **83**, 907 (1997)].
5. A. A. Chaban, Akust. Zh. **41** (6), 924 (1995) [Acoust. Phys. **41**, 819 (1995)].
6. Yu. V. Vladimirtsev, A. V. Golenishchev-Kutuzov, and V. A. Golenishchev-Kutuzov, Akust. Zh. **41** (3), 357 (1995) [Acoust. Phys. **41**, 309 (1995)].
7. V. K. Malinovskiĭ, O. A. Gudaev, V. A. Gusev, and S. I. Demenko, *Photoinduced Phenomena in Sillenites* (Nauka, Novosibirsk, 1990).
8. A. A. Berezhnoĭ and T. N. Sherstneva, Opt. Spektrosk. **67** (6), 1313 (1989) [Opt. Spectrosc. **67**, 773 (1989)].
9. S. I. Stepanov and M. Petrov, Opt. Commun. **53** (5), 292 (1985).
10. P. N. Ilinykh, O. P. Nestiorkin, and B. Ya. Zel'dovich, J. Opt. Soc. Am. B **8** (5), 1042 (1991).
11. É. Dieulesaint and D. Royer, *Elastic Waves in Solids* (Wiley, New York, 1981; Nauka, Moscow, 1982).
12. N. V. Kuchtarev, V. B. Markov, and S. G. Odulov, Ferroelectrics **22** (3–4), 949 (1979).
13. V. I. Balakshiĭ, V. N. Parygin, and L. E. Chirkov, *Physical Principles of Acoustooptics* (Radio i Svyaz', Moscow, 1985).

Translated by A. Kondrat'ev

Technical Physics Letters, Vol. 27, No. 7, 2001, pp. 542–543. Translated from Pis'ma v Zhurnal Tekhnicheskoĭ Fiziki, Vol. 27, No. 13, 2001, pp. 30–33.

Erbium Electroluminescence in an Al/a-Si:H(Er)/*p*-c-Si/Al Heterostructure

I. O. Kon'kov*, A. N. Kuznetsov, P. E. Pak, E. I. Terukov, and L. S. Granitsyna

Ioffe Physicotechnical Institute, Russian Academy of Sciences, St. Petersburg, 194021 Russia

** e-mail: Oleg.Konkov@pop.ioffe.rssi.ru*

Received February 20, 2001

Abstract—It is demonstrated for the first time that a high-intensity electroluminescence of erbium in amorphous hydrogenated silicon can be obtained using an Al/a-Si:H(Er)/*p*-c-Si/Al structure operated in a forward bias regime. © *2001 MAIK "Nauka/Interperiodica".*

Extensive investigations of the erbium photo- and electroluminescence in amorphous hydrogenated silicon (a-Si:H) in recent years were explained by the following circumstances: (i) the erbium emission wavelength (λ = 1.54 μm) falling within an optical absorption minimum of quartz optical fibers, (ii) a weak temperature luminescence quenching, and (iii) a relatively simple doping method offered by the magnetron sputtering [1–2]. The electroluminescence was observed in heterostructures of the Al/a-Si:H(Er)/*n*-c-Si/Al type representing essentially the Schottky barrier structure with a barrier height of 0.7–0.8 eV at the Al/a-Si:H(Er) junction. The a-Si:H(Er)/*n*-c-Si junction was almost ohmic because the *n*-crystalline silicon (*n*-c-Si) had a resistivity of 0.1–0.5 Ω cm. Forward-biased at room temperature (with minus on the c-Si substrate), the samples exhibited a free-exciton luminescence (λ = 1.16 μm) from the substrate; upon switching the bias to reverse, the erbium (λ = 1.54 μm) and defect (λ = 1.3–1.4 μm) luminescence was observed from the amorphous silicon layer [3].

This paper reports on the first observation of the erbium electroluminescence in a heterostructure of the Al/a-Si:H(Er)/*p*-c-Si/Al type in the forward-bias regime.

The films of erbium-doped amorphous hydrogenated silicon were obtained by reactive magnetron sputtering of metallic erbium in a silane-containing atmosphere (MASD) [4]. The MASD process parameters were as follows: initial gas mixture, 12.5% SiH_4 + 37.5% H_2 + 50% Ar; magnetic field strength, 80 mT; anode voltage, 600 V; discharge power density, 0.2 W/cm^2; total gas pressure, 4×10^{-3} Torr. The erbium target was made of 99.99% Er foil. The amorphous silicon film thickness was 0.5–0.6 μm; the heterostructure working area was 1 mm^2.

The samples represented *n*–*p* heterostructures with the barrier heights of 0.3–0.4 eV for electrons and 0.9–1.1 eV for holes. The current–voltage (*I*–*V*) characteristic of the heterostructure, typical of the *p*–*n* junction, is presented in Fig. 1. Application of a reverse bias voltage leads to an insignificant increase in the current. In this regime, the sample exhibits no electroluminescence. In the forward-bias regime, the current grows initially by the power law with an exponent of 1.15; when the applied voltage increases above ~30 V, the current growth becomes exponential. When the currents exceeds 5 mA, the sample exhibits a strong electroluminescence of erbium with λ = 1.54 μm and a weak luminescence due to free excitons. A typical electroluminescence spectrum is presented in Fig. 2.

Since the current density in the structure reaches 7 A/cm^2, the electroluminescence was observed for the samples with a crystalline silicon substrate mounted on a heat sink; the measurements were performed in a pulsed mode at a repetition frequency of 100 Hz and the on–off ratio 1 : 2. In the absence of heat removal, the samples exhibit overheating with the resulting reversible loss of electroluminescence.

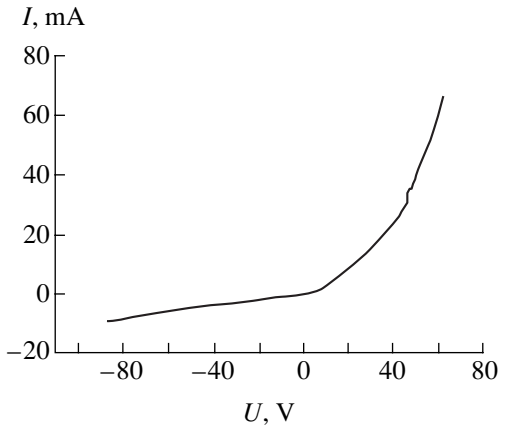

Fig. 1. A current–voltage characteristic of the Al/a-Si:H(Er)/*p*-c-Si/Al heterostructure.

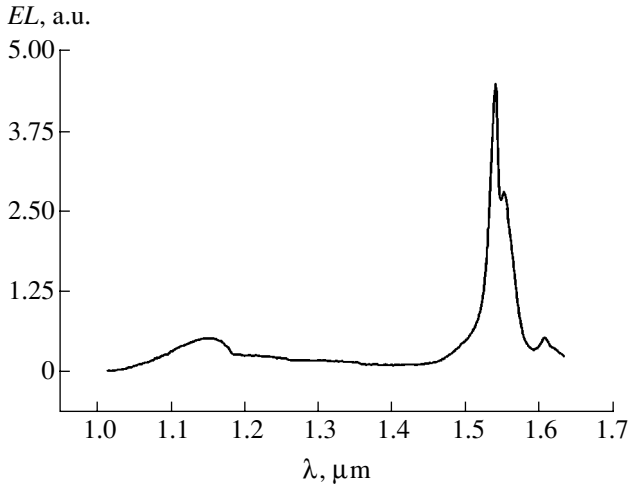

Fig. 2. Room-temperature electroluminescence spectrum of an Al/a-Si:H(Er)/*p*-c-Si/Al heterostructure operating at a current of 50 mA in the forward-bias regime.

The erbium electroluminescence intensity in the heterostructure studied exceeded that observed in reverse-biased Al/a-Si:H(Er)/*n*-c-Si/Al heterostructures for the same current density. The estimated electroluminescence efficiency was on a level of $\sim 2 \times 10^{-5}$.

The conduction and electroluminescence phenomena observed in the Al/a-Si:H(Er)/*p*-c-Si/Al heterostructures studied can be explained in terms of the mechanism of hole tunneling from c-Si via localized states in a-Si followed by release in the valence band or by recombination with electron in the conduction band of a-Si:H [5]. We believe that this mechanism provides for the best conditions for the resonance excitation of erbium ions; the electroluminescence efficiency in a heterostructure of this type may reach a greater level.

Thus, we have demonstrated for the first time that high-intensity electroluminescence of erbium can be obtained using an Al/a-Si:H(Er)/*p*-c-Si/Al structure operated in a forward-bias regime, which opens the way to implementing such devices in fiber optic communication lines.

Acknowledgments. This study was supported by the Russian Foundation for Basic Research.

REFERENCES

1. M. S. Bresler, O. B. Gusev, V. Kh. Kudoyarova, *et al.*, Appl. Phys. Lett. **67** (24), 3599 (1995).
2. J. H. Shin, R. Serna, G. N. van den Hoven, *et al.*, Appl. Phys. Lett. **68** (7), 997 (1996).
3. O. B. Gusev, M. S. Bresler, B. P. Zakharchenya, *et al.*, Fiz. Tverd. Tela (St. Petersburg) **41** (2), 210 (1999) [Phys. Solid State **41**, 185 (1999)].
4. M. S. Bresler, O. B. Gusev, B. P. Zakharchenya, *et al.*, Fiz. Tverd. Tela (St. Petersburg) **38** (4), 1189 (1996) [Phys. Solid State **38**, 658 (1996)].
5. H. Matsuura, T. Okuno, H. Okushi, and K. Tanaka, J. Appl. Phys. **55** (4), 1012 (1984).

Translated by P. Pozdeev

Technical Physics Letters, Vol. 27, No. 7, 2001, pp. 544–545. Translated from Pis'ma v Zhurnal Tekhnicheskoĭ Fiziki, Vol. 27, No. 13, 2001, pp. 34–38.

A Magnetic Field Sensor Based on the Mechanoelectric Effect in Semiconductors

Sh. M. Aliev, I. K. Kamilov*, A. K. Ataev, K. M. Aliev, and A. Kh. Abduev

Institute of Physics, Dagestan Scientific Center, Russian Academy of Sciences, Makhachkala, Dagestan, Russia

** e-mail: kamilov@datacom.ru*

Received February 13, 2001

Abstract—A highly sensitive magnetic field transducer based on the mechanoelectric effect in semiconductors is proposed. © *2001 MAIK "Nauka/Interperiodica".*

A mechanical-pressure-induced modification in the current–voltage characteristic of semiconductor devices, known as the mechanoelectric effect, is employed in various pressure transducers, microphones, acoustic pickups, and accelerometers [1, 2]. In the mechanoelectric transducers, the pressure-sensitive elements are typically based on the *p–n* junctions, transistors, Schottky diodes, and tunneling diodes, while the pressure is usually developed in a uniaxial regime or with the aid of a needle [1, 2].

In this paper, we will demonstrate that the mechanoelectric effect can be also used to create a highly sensitive magnetic field transducer.

Consider a magnetic dipole, possessing a central axis of rotation, with the side needles mounted on the poles capable of transferring mechanical pressure to some immobile pressure-sensitive semiconductor elements (Fig. 1a). Exposed to a magnetic field **H**, this dipole will be subjected to the action of a rotational moment due to an external couple [3]:

$$\mathbf{L} = \mathbf{MH}\sin\alpha, \qquad (1)$$

where **M** is the magnetic dipole moment and α is the angle between **H** and **M** vectors. Since the force moment always tend to rotate the dipole in the field direction, the mutual orientation of **M** and **H** vectors will determine the direction of the external couple acting upon the dipole (Figs. 1b and 1c). Note that $L = Fl$ and $M = ml$, where F is the force acting upon the dipole, l is the dipole length, and m is the "magnetic charge" value.[1] The pressure produced by the needle on the semiconductor element is

$$p = \frac{F}{S} = \frac{mH\sin\alpha}{S}, \qquad (2)$$

where S is the area of the needle–semiconductor element contact.

[1] The magnetic charge value usually is introduced for convenience by analogy with the electric charge and has the dimensionality of the magnetic field [Wb].

A prototype sensor manufactured for these experiments was based on a magnetic dipole with a length of 15 mm and a cross section of 1.5 × 1.5 mm cut of a

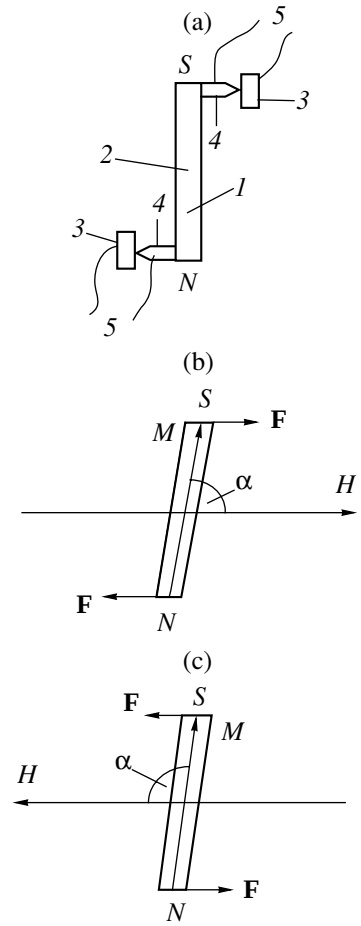

Fig. 1. (a) A schematic diagram of the magnetic field sensor employing the mechanoelectric effect: (*1*) magnetic dipole; (*2*) axis of dipole rotation; (*3*) immobile pressure-sensitive semiconductor elements; (*4*) needles; (*5*) electric leads. (b, c) Schematic diagrams illustrating the external coupes acting upon the magnetic dipole in magnetic fields having the opposite orientations.

1063-7850/01/2707-0544$21.00 © 2001 MAIK "Nauka/Interperiodica"

samarium–cobalt permanent magnet (KS 37 grade). The dipole, bearing indium-coated tungsten needles, was mounted on a clock pendulum mechanism made of a nonmagnetic material. The needle point radius was 30 μm. A semiconductor sensor represented 2×2 mm plates of germanium possessing a resistivity of 40 Ω cm, with a Pb–Sb alloy deposited onto one side so as to form ohmic contacts. The needle contact with the semiconductor crystal surface and the corresponding current–voltage (*I–V*) characteristic of the point diode was observed on an oscilloscope display. In order to improve the diode properties and provide for a high mechanical strength of the metal–semiconductor contact, the diode was subject to an electroforming treatment by passing current pulses with an amplitude of 1 A and a duration of 10 ms.

The transducer was placed into an organic glass case (protecting the electric contacts and mobile parts of the device from dust and moisture). Figure 2 shows the *I–V* curves of a sensor mounted at the center of a long solenoid. The magnetic field strength and direction were controlled by changing the magnitude and direction of the current passed through the solenoid; the α angle was 90°. As is seen from Fig. 2, a change in the field strength by a few Oersteds leads to a significant modification of the *I–V* curves of the point diodes. Reversal of the field direction shifts the *I–V* curve in the opposite direction relative to the curve observed for $H = 0$. This behavior is explained by the fact that a change in the field direction leads to reversal of the couple acting upon the dipole (Fig. 1b and 1c).

By analogy with the magnetic diode [4], the transducer sensitivity can be evaluated by the formula

$$\gamma = \frac{\Delta V}{IH}, \qquad (3)$$

where $\Delta V = V_H - V_O$ is the change in the diode voltage observed upon exposure of the sensor to the magnetic field and I is the current passing through the diode.

In a magnetic field with a strength of $H = 5$ Oe, the transducer response was $\gamma = 50$ V/(A Oe) for the forward *I–V* branch ($I = 0.4$ mA) and $\gamma = 3.0 \times 10^3$ V/(A Oe) for the reverse branch ($I = 0.1$ mA). Therefore, the reverse *I–V* branch is more sensitive to the magnetic field than the forward branch. In addition, the *I–V* curves show that the γ value depends on the magnetic field as well, being relatively more sensitive to weak fields. The sensitivity can be controlled toward both increase and decrease by varying the S and m values entering into formula (2). However, it must be borne in mind that the upper measurable field is limited by the coercive force of the dipole, which must be considerably greater than the field strength to be measured. For this reason, the sensor dipoles should be made of high-coercivity magnetic materials.

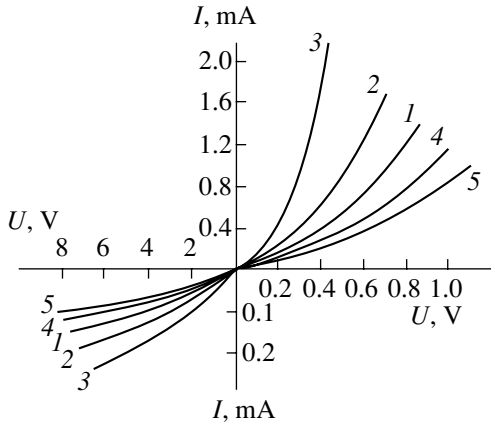

Fig. 2. Current–voltage characteristics of the mechanoelectric sensor diodes in the magnetic fields of various strength $H = 0$ (*1*); 5 (*2*); 20 (*3*); –5 (*4*); –20 Oe (*5*).

REFERENCES

1. A. L. Polyakova, *Deformation of Semiconductors and Semiconductor Devices* (Énergiya, Moscow, 1979).
2. I. I. Krivonosov, *Semiconductor Electroacoustic Converters in Radio Circuits* (Énergiya, Moscow, 1977).
3. S. Tikazumi, *The Physics of Ferromagnetism: Magnetic Properties and Applications* (in Japanese) (Mir; Moscow, 1987).
4. I. M. Vikulin and V. I. Stafeev, *Semiconductor Transducers* (Sov. Radio, Moscow, 1975).

Translated by P. Pozdeev

Technical Physics Letters, Vol. 27, No. 7, 2001, pp. 546–547. Translated from Pis'ma v Zhurnal Tekhnicheskoĭ Fiziki, Vol. 27, No. 13, 2001, pp. 39–43.

Thermobaric Treatment Induced Changes in the Structure and Magnetic Properties of Manganese Antimonide

V. S. Goncharov and V. M. Ryzhkovskiĭ

Institute of Solid State and Semiconductor Physics, National Academy of Sciences of Belarus, Minsk, Belarus

e-mail: dymont@ifttp.bas-net.by

Received January 19, 2001

Abstract—An orthorhombic phase of Mn_2Sb (a = 0.562 nm; b = 0.432 nm; c = 0.757 nm) was obtained for the first time in the manganese antimonide samples treated at a pressure of P = 7 GPa and a temperature of T = 1800 K. The high-pressure phase is metastable under normal conditions and breaks on heating above 420 K. A characteristic feature of this phase is the absence of a total magnetic moment at T > 90 K. © *2001 MAIK "Nauka/Interperiodica".*

Transition (3d) metal pnictides with the chemical formula A_2B (A = 3d element; B = Sb, As, P), including Mn_2Sb, crystallize in one of the three close structures: (i) tetragonal Cu_2Sb type (C38), (ii) hexagonal Fe_2P type (C22), and (iii) orthorhombic Co_2P type (C23). These compounds exhibit various magnetic properties determined to a considerable extent by their structural and dimensional characteristics. The genetic similarity of these structures (a common rhombohedral subcell, two types of structurally inequivalent cationic positions, similar coordination of a cationic environment of the anion, etc.) provides energetically favorable conditions for their mutual transformations both under the action of external factors (temperature, pressure) and upon changing the initial chemical matrix composition.

In the case of pressure- and chemical-substitution-induced lattice contractions, the direction of structural rearrangements usually follows the order C38 ⟶ C22 ⟶ C23, which can be related both to a decrease in the molecular volume in this structural sequence [1] and to an increase in strength of the metal–metal bonds with decreasing interatomic distances [2]. This very sequence of phase transformations was observed in the $Mn_{2-x}Co_xAs$ system [2], although the domains of existence of the C38, C22, and C23 phases are highly variable; in some concentration intervals, these phases may even coexist. Our experimental results showed that the boundary regions are characterized by close thermodynamic conditions of equilibrium between these related structures. This circumstance accounts for the structural instability (lability) and the sensitivity to variations in the chemical composition, degree of homogeneity, the presence of catalytic impurities, etc. [3].

Under normal conditions, the intermetallic compound Mn_2Sb possesses a tetragonal crystal structure of the Cu_2Sb type ($P4/nmm$, C38) and exhibits ferrimagnetic properties in the entire temperature range of magnetic ordering (T_k = 550 K). Below, we present new results concerning the effect of thermobaric treatments on the crystal structure and magnetic properties of this compound.

We have studied polycrystalline Mn_2Sb samples quenched from high temperatures, which contained a minimum amount of the accompanying nickel arsenide type phase (MnSb) [4]. The X-ray diffraction measurements were performed at T = 300 K on a diffractometer using CuK_α radiation. The magnetization was measured by the Faraday method at a magnetic field of 360 kA/m in a range of temperatures from 90 to 600 K. The samples were treated for 5 min under a quasihydrostatic pressure of 7 GPa and various temperatures (ranging from 300 to 1800 K). Then the samples were quenched and characterized by the X-ray diffraction and magnetic measurements.

The initial Mn_2Sb samples possessed a tetragonal crystal structure of the Cu_2Sb type (C38) with the lattice parameters a = 0.4075 nm; c = 0.6545 nm. The results of the X-ray diffraction measurements performed after the P–T treatment showed that no changes in the crystal lattice symmetry were induced by the treatment at P = 7 GPa in the temperature range from 300 to 1200 K. For the samples heated to T > 1200 K, the X-ray diffraction patterns revealed weak additional reflections not belonging to the initial tetragonal phase. The intensity of these reflections increased with the temperature, while intensity of the main phase reflections dropped accordingly. After the treatment at T = 1800 K, no reflections of the initial phase (tetragonal structure of the Cu_2Sb type) were observed. The X-ray diffractograms of the high-pressure Mn_2Sb were indexed within the framework of an orthorhombic unit cell with the parameters a = 0.562 nm; b = 0.432 nm; and c = 0.757 nm (Fig. 1).

The results of magnetic measurements (Fig. 2), on the one hand, confirmed the X-ray diffraction data indicative of the structural transformation of Mn_2Sb and, on the other hand, showed that the magnetic state of the

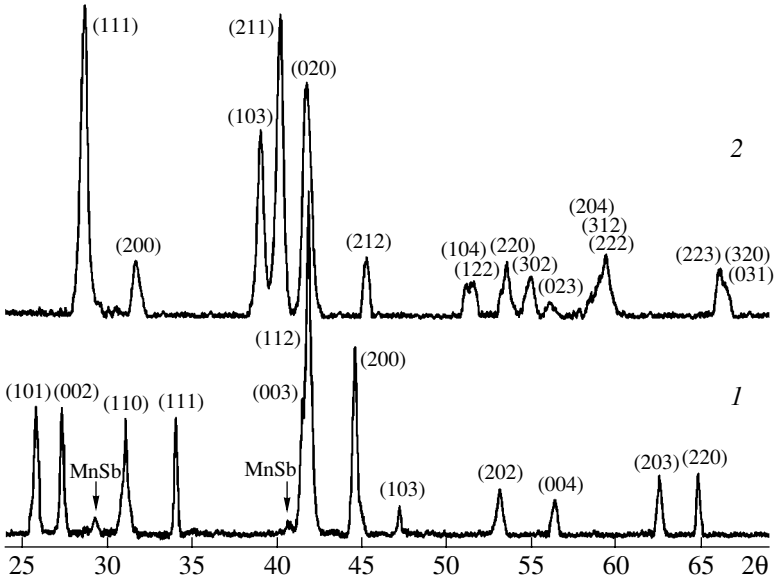

Fig. 1. X-ray diffraction patterns of Mn_2Sb samples (*1*) in the initial state and (*2*) after a thermobaric treatment at $P = 7$ GPa and $T = 1800$ K.

material sharply changed as well. Treatment of the initial samples at $P = 7$ GPa and $T = 300$–1000 K did not introduce principal changes into the magnetization behavior. A decrease in the magnetization level observed for the samples heated to $T > 1200$ K correlates with the X-ray diffraction data showing a decrease in the content of the initial ferrimagnetic phase and an increase in the proportion of a new, high-pressure phase, possessing (magnetometric data) no total magnetic moment. A small residual magnetization still observed can be attributed, in our opinion, to the presence of a small amount (≈1.5%) of the accompanying ferromagnetic phase MnSb.

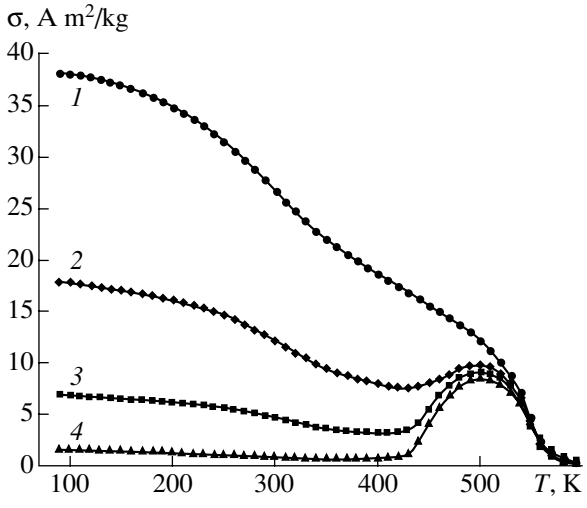

Fig. 2. The plots of specific magnetization σ versus temperature for Mn_2Sb samples (*1*) in the initial state and (*2*–*4*) upon the treatment at $P = 7$ GPa and $T = 1300$ (*2*), 1550 (*3*), and 1800 K (*4*).

An anomalous increase in the specific magnetization σ observed when the samples upon thermobaric treatment were repeatedly heated above 420 K is related to decomposition of the metastable high-pressure phase and the transition of the sample into the initial ferrimagnetic state with a tetragonal structure. This was confirmed by the X-ray diffraction data, according to which a sample treated at $P = 7$ GPa and $T = 1800$ K and then annealed for 20 h at 600 K possessed a tetrahedral structure of the initial type.

The presence of magnetic ordering and its character in the high-pressure phase of Mn_2Sb can be determined by direct neutron diffraction and Mössbauer measurements. These investigations are in progress.

Acknowledgments. The authors are grateful to V.P. Dymont and E.M. Nekrashevich for the fruitful discussions of results.

This study was partly supported by the Belarussian Foundation for Basic Research.

REFERENCES

1. J. B. Goodenough, J. Solid State Chem. **7**, 428 (1973).
2. A. Nylund, A. Roger, J. P. Senateur, *et al.*, Monatsch. Chem. **102**, 1631 (1971).
3. V. M. Ryzhkovskiĭ, E. M. Nekrashevich, V. P. Dymont, *et al.*, Cryst. Res. Technol. **31** (8), K96 (1996).
4. V. M. Ryzhkovskiĭ, V. P. Dymont, and I. L. Pashkovskiĭ, Dokl. Akad. Nauk Belarusi **40** (2), 64 (1996).

Translated by P. Pozdeev

Technical Physics Letters, Vol. 27, No. 7, 2001, pp. 548–550. Translated from Pis'ma v Zhurnal Tekhnicheskoĭ Fiziki, Vol. 27, No. 13, 2001, pp. 44–49.

Translational Partition Functions and Equilibrium Constants of Atomic and Molecular Particles

S. I. Igolkin

Baltic State Technical University, St. Petersburg, Russia

e-mail: kaf_m4@bstu.spb.su

Received November 20, 2000

Abstract—Some special features of the calculation of partition functions for the objects possessing finite dimensions are considered. It is shown that atomic, molecular, and more extended clusterlike objects are subject to certain spatial limitations related to the initial assumptions employed in the statistical approach. The values calculated for a material point or an object such as electron are overstated when applied to atomic particles. The classical expressions for the kinetic and statistical equilibrium constants of the reactions of formation and dissociation of diatomic molecules are compared. The observed discrepancies are eliminated by introducing corrections into formulas for the translational partition functions. *© 2001 MAIK "Nauka/Interperiodica".*

Features of the classical formula. The task of conducting detailed kinetic calculations for the reactions involving dissociation and formation of polyatomic cluster particles implies the necessity of a strict analysis of the standard methods used to determine the values entering into the kinetic equations and expressions for the equilibrium constants. In this context, the term representing a translational partition function for an elementary indivisible particle, atom, or molecule is of special importance.

The procedure of deriving a translational partition function presented in the classical monographs [1, 2] is based on an expression for the elementary phase volume containing a particle with the mass M, the geometric dimensions of which are related to the particle momentum via the Heisenberg uncertainty relationship:

$$\Delta p_x \Delta p_y \Delta p_z \Delta x \Delta y \Delta z = \left(\frac{h}{2\pi}\right)^3. \quad (1)$$

Upon determining the number of independent and nonrepeating energy states of the system by integrating over the gas volume V, we obtain the well-known expression for a partition function of the translational motion:

$$Z_m = \left(\frac{2\pi MkT}{h^2}\right)^{\frac{3}{2}} V. \quad (2)$$

The form of this expression indicates that the partition function is by no means related to the geometric dimensions of the particle. This is quite natural, since the initial formula for the phase volume refers to a material point or an object such as electron possessing pronounced wave properties or a large de Broglie wavelength.

The basic assumption that expressions (1) and (2) are derived for an ideal perfect gas cannot justify application of these formulas to the description of atomic and molecular objects, since both the phase volume and the vessel volume V enter into the calculation relationships in the explicit form. On thoroughly treating the problem, one may readily see that particles possessing final dimensions on the atomic level (such atoms, molecules and the more so, clusters) cannot be considered as material points or simple wave objects.

The above considerations imply, in particular, that a physical space volume occupied by a single atom may contain many various particles obeying relationship (1), including a nucleus, electrons of the same atom, etc. However, this volume may accommodate only one (!) whole atom. This discrepancy is rather significant and quite evident. Indeed, on repeating a classical calculation of the number of independent energy states for the translational motion of an isolated atom in a physical volume V commensurate with an atomic volume, we will not obtain the classical formula (2).

Kinetic formulas for the dissociation reaction and equilibrium constants. There are two possible approaches to determining the reaction rates for the association of atoms or the dissociation of dimers and, accordingly, to calculating the equilibrium constant of the forward and reverse reactions.

An expression for the equilibrium constant of the reaction of dimer formation derived according to the method of partition functions [2] is as follows:

$$K_S = \frac{P_1^2}{P_2} = \sqrt{kT}\frac{1}{4\sqrt{\pi}} M^{\frac{3}{2}} \frac{\nu_{vib}}{I_2} \frac{g_1^2}{g_2} e^{\frac{-\varphi_d}{kT}}, \quad (3)$$

where M is the atomic mass; ν_{vib} is the intrinsic oscillation frequency of the dimer; I_2 is the dimer gyration

moment; $g_{1,2}$ are the electron statistical weights of atom and dimer, respectively; and φ_d is the dissociation energy. Formula (3) is derived by disclosing expressions for the particular partition functions Z of free atoms and diatomic molecules occurring in the gas volume V:

$$K_S = \frac{Z_1^2}{Z_2} = \frac{Z_{m1}^2 Z_{e1}^2}{V Z_{m2} Z_{vib} Z_{rot} Z_{e2}}. \quad (4)$$

An alternative approach also frequently used for determining the equilibrium constant [2, 3] is as follows. According to the kinetic laws, an equation describing the formation of a diatomic molecule represents a balance of the rate of association for a three-body interaction of isolated atoms and the rate of dimer dissociation as a result of the impact of atoms belonging to the high-energy tail of the Maxwell velocity distribution:

$$\frac{dn_2}{dt} = \alpha 2 n_1^3 \sigma_a^2 \overline{v^2} \overline{\Delta v_L} \tau_c \left(1 - e^{-\frac{E_L}{kT}}\right)^s - \beta n_2 n_1 \sigma_d \bar{v} \overline{\Delta v_H} e^{-\frac{E_H}{kT}}, \quad (5)$$

where σ is the collision cross section; $\bar{v}$ is the average particle velocity; $\overline{\Delta v_L}$, $\overline{\Delta v_H}$ are corrections to the average velocity of reacting particles belonging to the slow and fast wings of the Maxwell distribution; τ_c is the characteristic time of interatomic collision, which is usually calculated by the formula $\tau_c = \frac{\sqrt{\sigma}}{v}$; E_H, E_L are the upper and lower energy thresholds for the given reaction; n_2 is the concentration of dimers in the ground state; n_1 is the concentration of free atoms; α and β are the correction coefficients taking into account the probability of the transition. In Eq. (5), the first term describes the rate of dimer formation, while the second term reflects the rate of its dissociation as a result of collisions with the particles possessing velocities above the threshold.

In the stationary state, the left-hand part of Eq. (5) is zero and the kinetic equilibrium constant is

$$K_k = \frac{P_n^2}{P_{n2}} = kT \frac{\beta}{\alpha} 2\sigma^{-\frac{3}{2}} \frac{\overline{\Delta v_H}}{\overline{\Delta v_L}} \frac{e^{-\frac{E_H}{kT}}}{\left(1 - e^{-\frac{E_L}{kT}}\right)^s}.$$

In a simplified form, this constant can be written as

$$K_k \approx kT 2\sigma^{-\frac{3}{2}} e^{-\frac{\varphi_d}{kT}}. \quad (6)$$

A principal difference between expressions (3) and (6) consists in using either the collision cross section σ or the mass M as constant factors at the exponent describing the reaction energetics. Discrepancies, reaching up to several orders of magnitude for various working bodies, are related to the features of determining the translational partition functions for heavy particles including atoms and molecules.

Translational partition function for heavy particles. Ambiguity related to the value of "characteristic size" of an atom or molecule and the features related to selection of the V value, the possibility of obtaining a rigorous formula for the partition function is not quite evident. The situation is elucidated by the following estimates and considerations. According to Eq. (2), the expression for the elementary phase volume occupied by any particle contains the product $\Delta p \Delta x$. For particles possessing pronounced wave properties, a characteristic size is the de Broglie wavelength related to the particle momentum by the uncertainty relationship (2). For better illustration, we may consider the phase volume of a particle as equal on the average to a cubic mathematical expectation of the de Broglie wavelength. Then, the translational partition function is equal to the number of such volumes accommodated in the vessel V at a given temperature T.

For an atomic or molecular particle (declining from its internal structure), the characteristic size and volume are constant quantities determined by the gasokinetic cross section. These values are independent of the particle energy and momentum:

$$r \approx \sqrt{\sigma}, \quad v \approx \sigma^{\frac{3}{2}}.$$

The dimensions of real atoms are, as a rule, significantly greater than the corresponding de Broglie wavelength λ_D. For example, the λ_D values for the atoms of copper and nitrogen at $T = 0.1$ eV amount to 0.16 and 0.34 Å, respectively. The characteristic atomic dimensions are on the order of $r_a \approx 2.5$ Å [4]. For the comparison, the de Broglie wavelength for electron with an energy of 0.1 eV is $\lambda_D = 5.5$ Å. Thus, in the range of practically important temperatures featuring the reactions of association of atoms and dissociation of dimers, a characteristic real particle size is more than ten times greater than the size stipulated in the translational partition function determined by Eq. (2).

Determined as the number of independent energy states of a particle contained within the system volume V, the translational partition function of a slow or immobile structureless object possessing an intrinsic volume v does not obey relationship (2) because of a sufficiently high determinacy of the positions of larger particles and their velocities. The probabilities of atomic distribution in the space of momenta are given by the Maxwell distribution. The integral over all possible momenta in a single atomic volume is equal to unity, independently of the coordinates or the uncertainty relationship. The integral over the volume V for a system of immobile hard particles occupying a physical

volume $v = \sigma r$ yields a simple expression for the partition function of or the number of independent positions within the volume V:

$$Z_m = \frac{V}{v} = \frac{V}{\sigma r} \approx \frac{V}{\sigma^{\frac{3}{2}}}. \quad (7)$$

The question as to which formula has to be employed apparently depends on the context of a physical problem to be solved. Once the characteristic temperature is known, a comparison of the real object size and the uncertainty relationship at this temperature should be used to select a maximum intrinsic volume between these of the wave and particle. Then the number of allowed different states is determined by integrating over the volume and momenta. It should be emphasized that these considerations refer to the whole indivisible atomic and molecular objects, their internal structures being ignored.

By substituting expression (7) into (4), both formulas for the equilibrium constants can be reduced to a common relationship of the type of relationship (6) containing a characteristic gasodynamic cross section with an exponent of –3/2. The remaining differences between equations are related to the features of taking into account the internal degrees of freedom of the dimeric molecules and fall out of the scope of this paper.

Thus, if the translational partition function of electron in the range of practically important temperatures has to be determined by formula (2), the partition function of atomic and molecular particles and clusters must be calculated by formula (7). Differences between the results of calculation according to formulas (2) and (7) for various working bodies may reach 4–5 orders of magnitude.

Conclusion. In calculating the rates of kinetic reactions using partition functions, it is necessary to explicitly take into account both the characteristic dimensions of objects and their velocities determined by the problem conditions. The proposed correction of the equilibrium relationships eliminates the discrepancies. This approach reflects the possible degeneracy of the allowed qualitatively different states of the object and the freezing of some degrees of freedom of the system, in accordance with a particular physical problem.

REFERENCES

1. L. D. Landau and E. M. Lifshitz, *Course of Theoretical Physics*, Vol. 5: *Statistical Physics* (Nauka, Moscow, 1964; Pergamon, Oxford, 1980).
2. Ya. B. Zel'dovich and Yu. P. Raizer, *Physics of Shock Waves and High-Temperature Hydrodynamic Phenomena* (Nauka, Moscow, 1966; Academic, New York, 1966).
3. J. W. Bond, K. M. Watson, and J. A. Welch, *Atomic Theory of Gas Dynamics* (Addison-Wesley, Reading, 1965; Mir, Moscow, 1968).
4. A. A. Radtsig and B. M. Smirnov, *Reference Data on Atoms, Molecules, and Ions* (Atomizdat, Moscow, 1980; Springer-Verlag, Berlin, 1985).

Translated by P. Pozdeev

Technical Physics Letters, Vol. 27, No. 7, 2001, pp. 551–553. Translated from Pis'ma v Zhurnal Tekhnicheskoĭ Fiziki, Vol. 27, No. 13, 2001, pp. 50–56.

Quantization of the Average Velocity of Motion in a Periodic Potential under the Action of an Ultrasonic Perturbation

V. L. Popov

Paderborn University, Germany

Institute of Strength Physics and Materials Science, Siberian Division, Russian Academy of Sciences, Tomsk, 634055 Russia

e-mail: popov@phys.unipaderborn.de

Received January 23, 2001

Abstract—The motion of a body in a periodic potential relief with weak damping is considered. It is shown that, in the presence of an additional periodic external action, dependence of the period-average velocity on the mean force of friction exhibits plateaus where variations in the acting force do not lead to changes in the average velocity. The plateau velocity is proportional to the frequency of the applied periodic perturbation and can be readily controlled. The effect can be used to create the driving mechanisms capable of ensuring motion at a strictly preset velocity not affected by the applied load variations. © *2001 MAIK "Nauka/Interperiodica".*

There are many technical applications involving drives where it is necessary to provide for the strictly controlled driving system parameters such as force, velocity, etc. The constancy of these parameters is usually ensured by creating a feedback chain. We propose using a principle according to which a constant sliding velocity in an artificial tribological couple (operating in a certain interval of loads) can be maintained based on the effect of phase self-adjustment analogous to one of the variants of the nonstationary Josephson effect [1].

Let us consider the motion of a body in a periodic potential with weak damping (Fig. 1). The equation of motion in this potential is as follows:

$$m\ddot{x} = F_R - \eta\dot{x} - F_0\sin(2\pi x/a), \qquad (1)$$

where m is the body mass, F_R is the force acting upon the body, η is the viscosity coefficient, F_0 is the amplitude of the periodic force, and a is the wavelength of the periodic potential. The model described by Eq. (1) provides for a simplified but very successful description of dry and boundary friction. In this or a slightly modified form, this model was extensively used in tribology and rheology (see, e.g., [2, 3]).

On the other hand, an equation of type (1) written as

$$\left(\frac{\hbar C}{2e}\right)\ddot{\varphi} = j - \left(\frac{\hbar}{2eR}\right)\dot{\varphi} - j_0\sin\varphi, \qquad (2)$$

describes the dynamics of the Josephson contact. Here, $\hbar$ is the Planck constant, φ is the phase difference between the contacting superconductors, C and R are the contact capacitance and resistance of the contact, e is the electron charge, and j_0 is the maximum current in the contact [1]. The mathematical equivalence of the two problems implies that the tribological systems admitting a microscopic model described by Eq. (1) must exhibit the effects analogous to those observed in the Josephson contacts. One of such effects consists in modification of the current–voltage (I–V) characteristic of the Josephson contact under the action of an external periodic perturbation, whereby the I–V curve exhibits a plateau corresponding to a strictly constant value of the voltage (this effect is employed, in particular, in the modern quantum standard of voltage).

A tribological analog of this effect would be the appearance of a plateau featuring a constant average velocity of motion in a certain interval of forces acting upon the moving body. This effect would be obviously important from the technical standpoint: the possibility of creating drives ensuring strictly fixed average velocity of motion in a certain interval of loads can readily find numerous mechanical applications. To our knowledge, this phenomenon (despite admitting direct analogy to the Josephson effect) was never considered in the tribological literature. Below, we present a mathematical analysis of the problem.

The physical mechanism of the proposed effect is as follows. If a body is moving at a macroscopically constant velocity in the presence of a spatially periodic

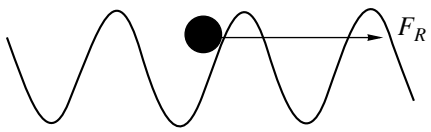

Fig. 1. A schematic diagram of a body moving in a periodic potential field.

1063-7850/01/2707-0551$21.00 © 2001 MAIK "Nauka/Interperiodica"

potential, the instantaneous velocity of motion and the force acting upon the body are (in the general case) periodic functions of time with a frequency depending on the average velocity. The time-averaged values of the acting force and velocity are evidently independent of the "initial phase" of these periodic functions, which phase can therefore be arbitrary. The situation will qualitative change if an additional external periodic action is applied to the body with a frequency equal to the aforementioned "intrinsic" frequency of the velocity and force oscillations. In view of the nonlinear dynamics of the system, the application of this additional periodic perturbation will result in the appearance of terms with equal frequencies in the equation of system dynamics. These terms will not vanish on averaging with respect to time and the corresponding average is dependent on the initial phase. This dependence implies that the time-averaged force can be varied by phase adjustment, while the average velocity remains unchanged. Note that the problem of describing the body motion in a periodic potential with weak damping is mathematically equivalent to the problem concerning dynamics of a single Josephson contact; the aforementioned phase self-adjustment phenomenon is analogous to a variant of the nonstationary Josephson effect [1].

The proposed effect can be illustrated by considering a particular case in which the additional periodic motion is superimposed onto the motion at a constant velocity. Below we will present the simplest mathematical analysis, although the same effect takes place under more complicated conditions as well.

As was mentioned above, when a body is moving in a periodic potential at a constant velocity v_0, the force acting upon this body is a periodic function of the time:

$$F_R = \eta v_0 + F_0 \sin\frac{2\pi}{a}(x_0 + v_0 t); \tag{3}$$

the average value of this force is $\bar{F}_R = \eta v_0$.

Now let the body moving with the constant velocity v_0 be subject to an additional periodic perturbation with a much smaller amplitude v_1 ($v_1 \ll v_0$):

$$v = v_0 + v_1 \cos\omega t. \tag{4}$$

The coordinate of the body is now described by a modified periodic function of the time

$$x = x_0 + v_0 t + \frac{v_1}{\omega}\sin\omega t, \tag{5}$$

while the force acting upon the body can be expressed as

$$F_R = \eta(v_0 + v_1\cos\omega t) + F_0 \sin\frac{2\pi}{a}\left(x_0 + v_0 t + \frac{v_1}{\omega}\sin\omega t\right). \tag{6}$$

The time-averaged force can be readily obtained upon expanding Eq. (6) in powers of the small parameter v_1/v_0 ($v_1 \ll v_0$):

$$\begin{aligned} F_R &= \eta(v_0 + v_1\cos\omega t) + F_0\left\{\sin\frac{2\pi}{a}(x_0 + v_0 t)\right. \\ &\left. + \frac{2\pi}{a}\cos\frac{2\pi}{a}(x_0 + v_0 t)\frac{v_1}{\omega}\sin\omega\right\} \\ &= \eta(v_0 + v_1\cos\omega t) + F_0\left\{\sin\frac{2\pi}{a}(x_0 + v_0 t)\right. \\ &\left. + \frac{2\pi v_1}{a\omega}\begin{bmatrix}\sin\left(\frac{2\pi}{a}(x_0 + v_0 t) + \omega t\right)\\ -\sin\left(-\frac{2\pi}{a}(x_0 + v_0 t) + \omega t\right)\end{bmatrix}\right\}. \end{aligned} \tag{7}$$

For the first three terms, the time-averaged values are always zero, while the last term in square brackets is zero for $\omega \neq \frac{2\pi v_0}{a}$ and equals to

$$\bar{F}_R = \eta v_0 + F_0\frac{2\pi v_1}{a\omega}\sin\frac{2\pi}{a}x_0 \tag{8}$$

for

$$\omega = \frac{2\pi v_0}{a}. \tag{9}$$

Thus, at a certain frequency of the external periodic perturbation, the average force acting upon the body may acquire any value in the interval

$$\eta v_0 - \left|F_0\frac{2\pi v_1}{a\omega}\right| < \bar{F}_R < \eta v_0 + \left|F_0\frac{2\pi v_1}{a\omega}\right|, \tag{10}$$

while the average velocity of motion remains unchanged. The force changes as a result of the phase self-adjustment to the initial value of $2\pi x_0/a$ according to Eq. (8). If the external force exceeds the maximum boundary value in the interval (10), the velocity will again increase with the force. As can be readily seen, all velocities obeying the relationship

$$v_0 = \frac{a\omega}{2\pi}n, \tag{11}$$

where n is an integer, correspond to plateaus in which the force may vary within certain limits not affecting the corresponding average velocity. The behavior of the average velocity of motion in this system plotted as a

function of the average external force is qualitatively illustrated in Fig. 2.

The assumption concerning smallness of the perturbation amplitude was important only for the above simple calculation based on the expansion into the Taylor series. As is known from the physics of the Josephson contact, this condition is not principally significant for the velocity quantization effect.

The "quantized" velocity values corresponding to plateaus of the velocity versus force curves are determined by formula (11) and, as is seen from this expression, depend only on the frequency of the external periodic perturbation and the wavelength of the potential relief. Therefore, these velocity values can be set with high precision and readily controlled by varying the frequency.

The effect describe above can be used for creating drives providing for a strictly fixed and readily controlled velocity of motion. An example of such a system implementing the effect is offered by the contact of two plates with the surfaces bearing an artificial periodic microrelief (relative to the translation or rotation direction). Under the action of an acoustic wave of sufficient amplitude acting upon one of the contacting plates, the system acquires a force–velocity characteristic of the type schematically depicted in Fig. 2, with the plateau velocities determined by formula (10), where a is the period of the microrelief. For example, a plateau velocity of 1 m/s in a system with $a = 1$ μm is provided by an external perturbation with a frequency of about 1 MHz. This example shows that, taking into account the existing possibilities of forming regular surface microreliefs and the available ultrasound sources, the creation of the stable drives with controlled velocity within technically important intervals presents no significant difficulties.

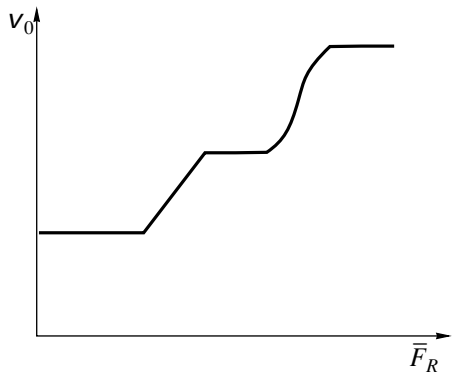

Fig. 2. A qualitative pattern of variation of the average sliding velocity v_0 as a function of the average friction force $\bar{F}_R$ in the presence of an additional periodic perturbation. See the text for explanation.

REFERENCES

1. A. Barone and G. Paterno, *Physics and Applications of the Josephson Effect* (Wiley, New York, 1982; Mir, Moscow, 1984).
2. V. Zaloj, M. Urbakh, and J. Klafter, Phys. Rev. Lett. **81** (6), 1227 (1998).
3. V. Zaloj, M. Urbakh, and J. Klafter, Phys. Rev. Lett. **82** (24), 4823 (1999).

Translated by P. Pozdeev

Technical Physics Letters, Vol. 27, No. 7, 2001, pp. 554–556. Translated from Pis'ma v Zhurnal Tekhnicheskoĭ Fiziki, Vol. 27, No. 13, 2001, pp. 57–63.

Effect of the Target Surface Temperature on the Distribution of Nanoparticles Formed by Ion Implantation

A. L. Stepanov[ab]*, D. Hole[c], and V. N. Popok[de]

[a] *1. Physikalisches Institut, Aachen Technical University, 52056 Aachen, Germany*
[b] *Kazan Physical-Technical Institute, Russian Academy of Sciences, Kazan, 420029 Russia*
[c] *University of Sussex, BN1 9QH Brighton, England*
[d] *Göteborg University & Chalmers University of Technology, 41296 Göteborg, Sweden*
[e] *Belarussian State University, Minsk, 220050 Belarus*
** e-mail: stepanov@physik.rwth-aachen.de*
Received December 26, 2000

Abstract—Metal-nanoparticle-containing composite layers were synthesized by implantation of 60 keV Ag^+ ions into a soda-lime silicate glass to a dose of 3×10^{16} ion/cm^2 at an ion beam current density of 3 μA/cm^2 and a substrate temperature of 35°C. The results of implantation depend on the temperature effects developed in the glass targets of various thicknesses. Data on the silver distribution profile and the nucleation and growth of metal nanoparticles in depth of the implanted layers were obtained from the optical reflection spectra. It is demonstrated that even small variations in the surface temperature of the ion-bombarded glass substrate lead to significant changes in the conditions of nanoparticle formation in the sample. © *2001 MAIK "Nauka/Interperiodica".*

Ion implantation is one of the most effective and technological methods available for the synthesis of nanoparticles in solids [1]. For example, silicate glasses containing nanoparticles of Ag, Au, or Cu can be used for solving the tasks of nonlinear optics [2, 3], layers containing Fe clusters can be employed in magnetic data storage elements [4], and silicon dioxide films with Sn or Sb nanoinclusions on silicon substrates can serve a base for combined optoelectronic devices [5]. The main advantage of ion implantation in the synthesis of composite materials is the possibility of filling the implanted layer with atoms of almost any metal at an amount above the equilibrium solubility limit.

Despite obviously good prospects, the synthesis of metal nanoparticles in insulating matrices by the ion implantation technique is a complicated process depending on a large number of factors. One of the main features in the ion implantation process is a statistical scatter in the penetration depth of implanted ions and, hence, an inhomogeneous distribution of the concentration of impurity atoms in the subsurface layer of the ion-irradiated target. This results in that the nanoparticles formed are characterized by a size distribution both in the lateral direction (parallel to the target surface) and in depth of the ion-implanted material [1, 6]. However, the conditions of formation of the implanted metal nanoparticles can be changed by varying parameters of the ion implantation process.

It is well known that the temperature of an ion-bombarded substrate is one of the most important factors affecting the implanted impurity distribution (depth–concentration profile) in the target. Unfortunately, this parameter is frequently not controlled in the course of the ion implantation process, although an increase in the substrate temperature by only a few dozen degrees may lead to intensive thermostimulated diffusion of the impurity in depth of the target, thus reducing the local concentration of metal atoms in a glass substrate [7]. In practice, a preset substrate temperature is usually maintained by forced cooling of the target holder. However, this approach is insufficiently effective in the case of insulators, which typically possess low thermal conductivities. This circumstance increases the role of the thickness of dielectric substrates as a factor determining the target surface temperature during the ion implantation and, hence, influencing the synthesis of nanoparticles. The purpose of this study was to experimentally verify this assumption in the case of Ag nanoparticles formed by silver ion implantation into a soda-lime silicate (SLS) glass.

A composite material was based on an SLS glass (Societa Italiana Vetro company, Italy) representing a homogeneous mixture of the chemical components: 70% SiO_2, 20% Na_2O, 10% CaO. The SLS glass was characterized by an optical transmission of ~90% in the 350–900 nm range. The samples were prepared in the form of plane-parallel plates with lateral dimensions 1.5×1.5 cm and two thicknesses: 0.15 mm (thin samples) and 3.1 mm (thick samples). These glass substrates were implanted with 60 keV $^{107}Ag^+$ ions at an ion beam current of 3 μA/cm^2 to a dose of 3×10^{16} ion/cm^2; all samples were processed under identi-

cal conditions on a Whickman implanter system in a vacuum of 10^{-5} Torr. The glass substrates were fixed with a heat-conducting glue on a massive metal plate. The temperature of this target holder could be monitored and stabilized by a system including a resistive heater and a gas cooler. During the implantation process, the target holder temperature was maintained at 35°C.

The ion-implanted samples with inhomogeneous distribution of metal nanoparticles in depth of the material were analyzed by a method described previously [6], based on the light reflection measurements from both the front (ion-irradiated) and the rear (unirradiated) surface of a glass target. The reflection and transmission spectra of the samples were measured at room temperature using a single-beam fiber spectrometer of the Monolight type. The spectra were measured in the range from 350 to 800 nm at a 90° angle of the probing beam incidence on the sample surface. The intensities of reflection spectra were corrected for the signal attenuation depending on the sample thickness.

An increase in the concentration of Ag atoms in the glass above the solubility limit leads to the nucleation of metal nanoparticles. Assuming that the nanoparticle growth results from the sequential attachment of Ag^0 atoms formed upon the neutralization of Ag^+ ions, we may suggest that the growth of nanoparticles is controlled simultaneously by the diffusion coefficient and the local concentration of silver atoms. If the mobility of Ag^0 in the glass matrix is low, the growth will proceed mostly at the expense of incorporated Ag^+ ions (the nanoparticle growth under limited diffusion conditions [8]). Since an increase in the absolute concentration of metal ions in the implanted layer is described by the depth–concentration profile depending on the irradiation time (or on the accumulated ion dose), the process of nucleation and growth of metal nanoparticles is also time-dependent.

Evidently, the size of metal particles formed at a certain depth is proportional to the factor of glass matrix filling with metal at the same depth and, hence, is also determined by the depth–concentration profile of implanted ions. According to the theoretical profiles of Ag distribution in SLS glass, which were calculated with an allowance for the sputtering effects but with neglect of the diffusion mobility, the Ag concentration exhibits a maximum at the target surface and then monotonically decreases in depth of the sample [9]. Therefore, the largest Ag nanoparticles also form at the target surface and a decrease in the implanted ion concentration with depth must be accompanied by a drop in the particle size, which was confirmed by the electron-microscopic observations in the cross sections of metal-implanted glass samples [3, 10].

The experimental reflection and transmission spectra of SLS samples of different thickness implanted with Ag^+ ions are presented in the figure. The broad selective spectral bands observed in the visible spectral

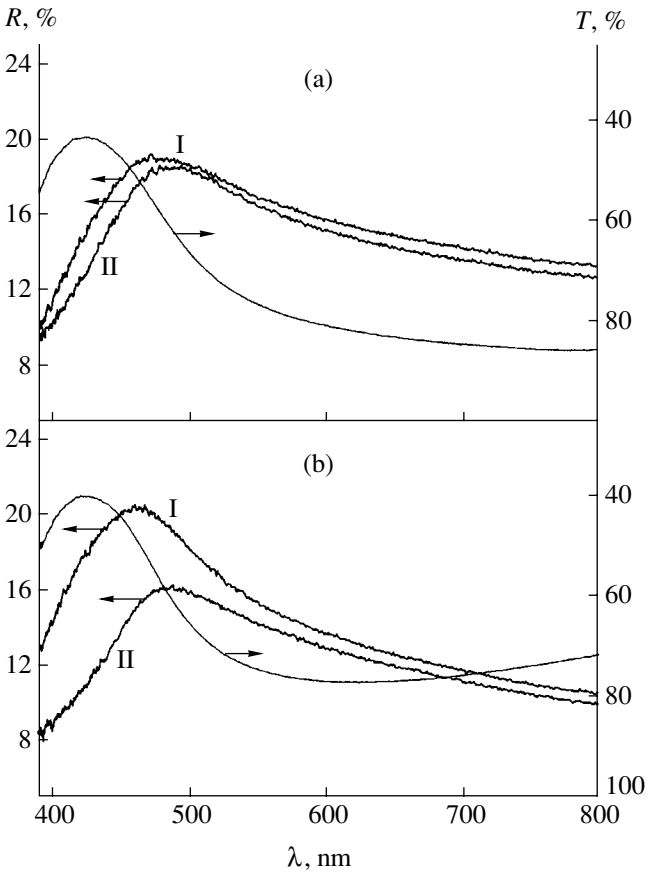

Experimental optical spectra of reflection R and transmission T for the Ag^+-ion implanted soda-lime glass samples with a thickness of (a) 0.15 mm and (b) 3.1 mm measured from the (I) ion-irradiated and (II) unirradiated side.

range are related to the formation of Ag nanoparticles in the glass matrix and explained by the phenomenon of plasma polariton resonance [6, 11]. The transmission spectra measured from both the ion-irradiated and unirradiated sides of the substrate are identical. As is seen, there is no visible distinctions between the absorption bands at 425 nm (corresponding to the optical resonance of Ag nanoparticles) in the spectra of thick and thin samples. A small difference in the long-wavelength part of the spectrum was due to the intrinsic absorption spectrum of SLS glass, which was manifested because the transmission measurements were performed without compensation for the sample thickness.

As was demonstrated previously [6], the optical transmission spectra do not reflect the character of distribution of the impurity nanoparticles in depth of the implanted samples. We will compare the samples based on their reflection spectra. If a sample features inhomogeneous distribution of the nanoparticle size with depth, this unavoidably leads to variation in the light absorption and reflection conditions in the layers containing particles of different size and must be manifested by a difference in the shape of reflection spectra

measured from the ion-irradiated and unirradiated sides of the glass substrate. Indeed, this difference is clearly observed for the reflection spectra of a thick sample presented in panel (b) of the figure. According to these, the reflection spectrum measured from the ion-irradiated side exhibits a broad intense band with a maximum at 460 nm, whereas the spectrum measured from the opposite side displays a much less intense band peaked at a wavelength of 485 nm. This difference is explained [6] by dissimilar distribution of meal nanoparticles in depth of the sample, whereby greater particles are located at the ion-irradiated surface while the smaller species are incorporated deeper into the sample. This situation is typical and was frequently observed in ion-implanted glasses [10, 12].

A somewhat different situation is observed in the spectra of thin sample presented in panel (a) of the figure. Here, the reflection spectra measured from both the ion-irradiated and unirradiated sides of the glass substrate are almost identical with respect to both intensity and position of the absorption peak (475 nm) and the shape (spectral intensity distribution). This similarity is indicative of a uniform distribution (symmetric profile) of Ag nanoparticles in depth of the implanted layer.

Apparently, the difference observed between the spectra of thin and thick samples implanted under identical conditions can be attributed to a difference in the temperature gradient developed in the subsurface layers of two glass targets heated by the ion beam. Since the surface temperature of a thick sample must be higher (because of the hindered heat removal) than that of a thin one, the implanted atoms in the former case would possess a higher mobility and more readily diffuse from the surface inward the sample. This leads to a more uneven accumulation of impurity in the implanted layer and, eventually, to the formation of an inhomogeneous particle depth–concentration profile. In a thin sample, featuring a lower temperature gradient between the ion-irradiated surface and the unirradiated surface contacting with the cooled plate, the target surface is not subject to overheating—a factor stimulating redistribution of silver nanoparticles in depth of the implanted layer.

Thus, we have experimentally established the effect of the surface temperature of a soda-lime glass target on the final distribution of implanted silver. It was demonstrated that the effect is more significant for thick samples, where a greater temperature difference between the ion-irradiated and cooled sample surfaces can be expected. Such temperature gradients lead to an inhomogeneous depth–concentration profile of impurity in the target and, eventually, to an inhomogeneous nanoparticle size distribution in depth of the sample. Although the difference in the thickness of glass substrates used in our experiments was very small (below two millimeters), the spectral characteristics of ion-implanted samples were significantly different. This fact suggests that the optical spectra can be used in practice for monitoring the fabrication of optical devices.

Acknowledgments. One of the authors (A.L.S.) is grateful to the Alexander Humboldt Foundation (Germany) for the financial support of his work in Germany; V.N.P. is grateful to the Scientific Research Council of Sweden (SNFR).

The work was supported by the Russian Foundation for Basic Research, project no. 99-02-17767.

REFERENCES

1. P. D. Townsend, P. J. Chandler, and L. Zhang, *Optical Effects of Ion Implantation* (Cambridge Univ. Press, Cambridge, 1994).
2. A. L. Stepanov, I. B. Khaĭbullin, P. Townsend, D. Hole, and A. A. Bukharaev, RF Patent No. 2156490 (2000).
3. H. Hosono, Phys. Rev. Lett. **74** (1), 110 (1995).
4. A. A. Bukharaev, A. V. Kazakov, R. V. Manapov, and I. B. Khaĭbullin, Fiz. Tverd. Tela (Leningrad) **33** (4), 1018 (1991) [Sov. Phys. Solid State **33**, 578 (1991)].
5. A. Nakajima, H. Nakao, T. Futatsugi, and N. Yokoyama, J. Vac. Sci. Technol. B **17** (4), 1317 (1999).
6. A. L. Stepanov, Opt. Spektrosk. **89** (3), 444 (2000) [Opt. Spectrosc. **89**, 408 (2000)].
7. D. E. Hole, A. L. Stepanov, and P. D. Townsend, Nucl. Instrum. Methods Phys. Res. B **148**, 1054 (1999).
8. A. C. Zettlemoyer, *Nucleation* (Marcel Dekker, New York, 1969).
9. A. L. Stepanov, V. A. Zhikharev, D. E. Hole, *et al.*, Nucl. Instrum. Methods Phys. Res. B **166**, 26 (2000).
10. L. C. Nistor, J. van Landuyt, J. B. Barton, *et al.*, J. Non-Cryst. Solids **162**, 217 (1993).
11. U. Kreibig and M. Vollmer, *Optical Properties of Metal Clusters* (Springer-Verlag, Berlin, 1995).
12. N. Kishimoto, Y. Takeda, N. Umeda, *et al.*, Nucl. Instrum. Methods Phys. Res. B **166**, 840 (2000).

Translated by P. Pozdeev

Technical Physics Letters, Vol. 27, No. 7, 2001, pp. 557–559. Translated from Pis'ma v Zhurnal Tekhnicheskoĭ Fiziki, Vol. 27, No. 13, 2001, pp. 64–69.

Microwave Generation Features in a Vircator with an Inhomogeneous Magnetic Field in the Interaction Region

A. E. Dubinov and V. D. Selemir

Institute of Experimental Physics, Russian Federal Nuclear Center, Sarov, Russia

Received January 24, 2001

Abstract—A vircator with an inhomogeneous external magnetic field superimposed onto the cathode–anode–virtual cathode potential well was studied by methods of computer modeling. It is shown that the application of such additional field allows a significant (almost fivefold) increase in the microwave generation efficiency, which is explained by the gyrotron effect development. © *2001 MAIK "Nauka/Interperiodica".*

Microwave generators with virtual cathodes—vircators, reflex klystrons, and reditrons—are the most popular types of generators employed in the past three decades in high-power relativistic microwave electronics. As pointed out in [1], the maximum generator power increased by one order of magnitude in each decade to reach a colossal value of 22 GW by the beginning of 1990s [2]. The state-of-the-art in this field was reviewed in [3].

However, the past decade revealed some new trends: the rush for record output powers was changed by searching for the ways to increase the efficiency of the microwave generation. This resulted in finding technical means of coherently adding the outputs of a number of vircators operating at a moderate (subgigawatt) power [4].

In this context, we have used numerical modeling methods to check for the idea of increasing the vircator efficiency by using inhomogeneous magnetic fields in the interaction region. Although we proposed this idea almost a decade ago [5] and mentioned this method in [6, 7], the project was studied neither theoretically nor experimentally. Let us briefly cover the idea again.

Kwan and Snell [8] suggested a new vircator concept, called by the authors the reflex electron discrimination tube (reditron), the essence of which was to discriminate electrons reflected from the virtual cathode (VC) so as to exclude the diode perturbation. The reditron creators believed that this would increase the generator efficiency. However, our subsequent investigations [9, 10] showed that the reflex electron discrimination also excluded the feedback in the microwave generator, thus breaking the radiative instability. In development of the reditron concept, we proposed [5] a reditron variant where only "soft" reflex electrons (i.e., those having radiated their energy and losing synchronism) rather than all reflex electrons were discriminated. This "sorting" of electrons in the cathode–anode–VC potential well can be performed by superimposing a longitudinal magnetic field with a minimum strength at the anode grid.

In this study, we aimed at a more profound investigation to establish how the presence of both minimum and maximum magnetic field in the interaction region would affect the vircator characteristics.

The numerical modeling was carried out using a 2*D* (*rz*) variant of the well-known code KARAT (version 70720) [11] representing a fully self-consistent relativistic electromagnetic PIC code. A configuration of the vircator region modeled is schematically depicted and the necessary dimensions are indicated in Fig. 1.

We studied a system with the main axial magnetic field of 5 kOe decaying to zero near the output window ($25 < z < 27$ cm) so as to provide for the transit electron withdrawal onto walls of the vircator drift tube in order to close the reverse current circuit and prevent the output window from being charged and damaged. Using an additional solenoid coil or by some other means, it

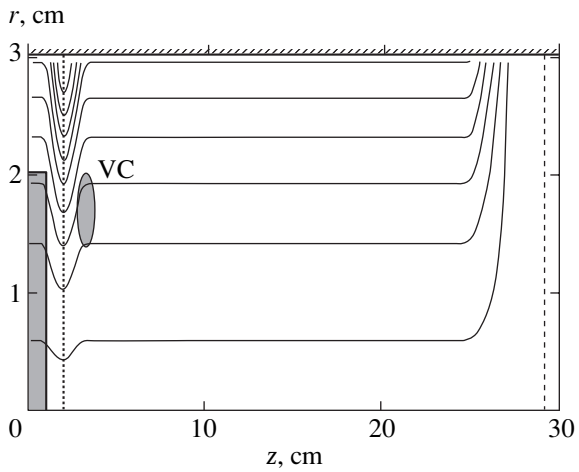

Fig. 1. A schematic diagram of the model vircator configuration.

1063-7850/01/2707-0557$21.00 © 2001 MAIK "Nauka/Interperiodica"

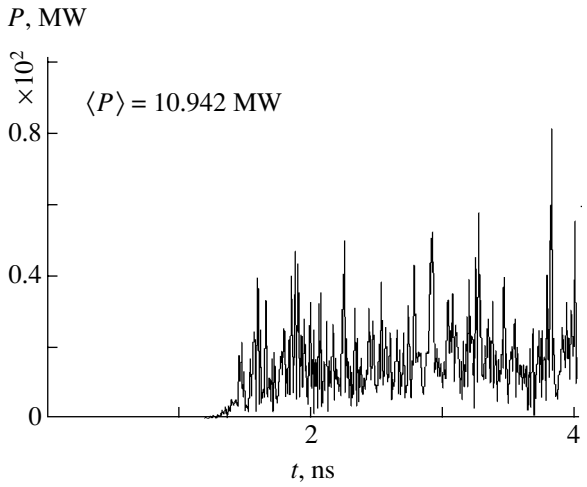

Fig. 2. A typical calculated "oscillogram" of the output microwave signal power.

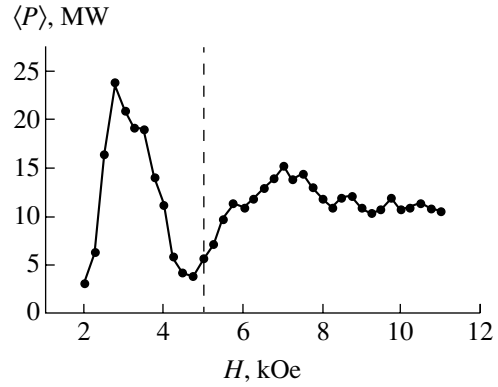

Fig. 3. The plot of average output power versus magnetic field strength at the vircator anode. The dashed line corresponds to the case of a homogeneous field profile.

was possible to provide for the inhomogeneity of the magnetic field in the interaction region between cathode and VC. We selected the following structure of inhomogeneous magnetic field in the cathode–VC region: the field strength on the system axis varied according to a linear law between cathode and anode grid and then also linearly returned to the initial value on the passage from anode to VC.

Using a preset magnetic field configuration on the system axis, the computational program preliminarily calculated the magnetic field distribution in the whole system by numerically solving the equation div**H** = 0. A typical geometry of the magnetic field lines (for an inhomogeneity type with maximum) is presented in Fig. 1.

A positive rectangular high-voltage pulse with an amplitude of 200 kV applied to the cathode produced a 15 kA current,[1] which was sufficient for the VC formation. The output microwave generation was monitored during 4 ns by calculating the Poynting vector flux in a cross section situated between the output window and the site of transit electrons withdrawal onto the drift tube walls (this section is indicated by the dashed line at $z = 29$ cm in Fig. 1). Figure 2 shows a typical calculated "oscillogram" of the output signal power. The microwave generation was calculated for various values of the magnetic field strength (2–11 kOe) at the anode grid. Figure 3 shows the plot of average (over 5 ns) output power versus magnetic field strength at the anode.

An analysis of Fig. 3 shows that creation of an inhomogeneous magnetic field with a minimum of 2–4 kOe at the anode grid increases the output microwave power almost five times as compared to that for a usual vircator with a homogeneous magnetic field. In this case, the inhomogeneous field actually ensures the removal of "soft" reflex electrons to the anode tube (soft electron discrimination reditron mode). In addition, it was established that fast electrons moving in the inhomogeneous magnetic field acquire significant transverse rotational motion component, which favors development of the *TE* mode generation due to the gyrotron effect analogous to that described in [12]. In the case of a still more pronounced decrease in the magnetic field strength at the anode (down to 0–2 kOe), all electrons leave the interaction region without crossing the grid and, hence, the microwave generation ceases.

If the inhomogeneous magnetic field has a configuration with a maximum of 6–8 kOe, the output microwave power is almost three times that for a usual vircator with a homogeneous magnetic field profile. As expected, in this case only the gyrotron effect contributes to the power gain, whereas the loss of soft reflex electrons is not manifested. When the field strength maximum exceeds 8 kOe, no VC is formed in the system and the generator operates in the pure gyrotron regime with an output microwave power about twice that of the homogeneous vircator.

Thus, we have demonstrated that application of an inhomogeneous magnetic field to the interaction region of a vircator increases both the output microwave power and the efficiency of the generator. The increase is observed for inhomogeneous fields with both maximum and minimum at the anode grid.

Acknowledgments. The authors are grateful to V.P. Tarakanov for his help in using the code CARAT and to K.G. Kostov for drawing our attention to the possibility of using the gyrotron effect in vircators.

REFERENCES

1. C. Castro, Defence Electronics **22** (2), 82 (1990).
2. A. Bromborsky, F. Agee, M. Bollen, *et al.*, Proc. SPIE **873**, 51 (1988).
3. A. E. Dubinov and V. D. Selemir, Zarubezhn. Radioélektron., No. 4, 54 (1995).

[1] During the system evolution, the cathode current exhibited a self-consistent variation depending on the space charge in the diode region of the vircator.

4. V. D. Selemir, A. E. Dubinov, N. V. Stepanov, *et al.*, in *Proceedings of the Russian Federal Nuclear Center–All-Russia Research Institute of Experimental Physics* (Sarov, 2000), No. 1.
5. V. D. Selemir, A. E. Dubinov, and N. V. Stepanov, RF Patent No. 2044361, MKI: H01 J 25/68, Byull. Izobret., No. 26 (1995).
6. B. V. Alyokhin, A. E. Dubinov, V. D. Selemir, *et al.*, IEEE Trans. Plasma Sci. **22** (5), 945 (1994).
7. V. D. Selemir, B. V. Alekhin, V. E. Vatrunin, *et al.*, Fiz. Plazmy **20** (7-8), 689 (1994) [Plasma Phys. Rep. **20**, 621 (1994)].
8. T. J. T. Kwan and C. M. Snell, US Patent No. 4730170, H03 B 9/01 (1987).
9. V. E. Vatrunin, A. E. Dubinov, V. D. Selemir, and N. V. Stepanov, in *Fractals in Applied Physics: Collection of Scientific Works*, Ed. by A. E. Dubinov (Arzamas-16, 1995), p. 47.
10. A. E. Dubinov and V. D. Selemir, Pis'ma Zh. Tekh. Fiz. **24** (4), 41 (1998) [Tech. Phys. Lett. **24**, 142 (1998)].
11. V. P. Tarakanov, *User's Manual for Code Karat* (Berkley Research Associate Inc., Springfield, 1992).
12. K. G. Kostov, I. G. Yovchev, and N. A. Nikolov, Electron. Lett. **35** (19), 1647 (1999).

Translated by P. Pozdeev

Technical Physics Letters, Vol. 27, No. 7, 2001, pp. 560–562. Translated from Pis'ma v Zhurnal Tekhnicheskoĭ Fiziki, Vol. 27, No. 13, 2001, pp. 70–75.

The Concept of Elementary Excitations in Classical Statistical Mechanics

A. Yu. Zakharov

Novgorod State University, Novgorod the Great, Russia

e-mail: ayz@novsu.ac.ru

Received February 20, 2001

Abstract—Exact representations of the generating functional of one-component classical systems with a central interatomic interaction potential are obtained in terms of the functional integrals over auxiliary fields determined in the wavevector space. It is proved that the problem of calculating a classical partition function for a system of particles with an arbitrary interatomic interaction potential is equivalent to the problem of calculating a statistical integral for a system of interacting oscillators with a temperature-dependent Hamiltonian. © *2001 MAIK "Nauka/Interperiodica".*

The generating functional of a system of N particles interacting via two-body potential $v(\mathbf{r})$ in the presence of an external field $\varphi(\mathbf{r})$ acquires upon integration with respect to momentum the known form:

$$Z\{\varphi(\mathbf{r})\} = \frac{V^N}{N!\lambda^{DN}} \int\limits_{(V^N)} \cdots \int \left(\prod_{s=1}^{N} \frac{d^D\mathbf{R}_s}{V}\right) \times \exp\left(-\beta \sum_{s=1}^{N} \varphi(\mathbf{R}_s)\right) \exp\left(-\frac{\beta}{2} \sum_{\substack{s,s'=1 \\ s\neq s'}}^{N} v(|\mathbf{R}_s - \mathbf{R}_{s'}|)\right), \quad (1)$$

where $\lambda = (2\pi\hbar^2/mk_BT)^{1/2}$ is the de Broglie thermal wavelength, $\beta = 1/k_BT$ is the reciprocal temperature, V is the system volume, D is the space dimension, and $\hbar$ and k_B are the Planck and Boltzmann constants, respectively.

In Eq. (1), the first exponent term related to the external field represents a product of identical one-atom components of the type $\exp(-\beta\varphi(\mathbf{R}_s))$. The second exponent does not separate into one-atom multipliers because the atomic coordinates $\mathbf{R}_s$ exhibit mutual "entangling" via the interaction potential.

A possible means of "separating" the atomic coordinates in an interatomic potential of the general form consists in using a functional integration technique. There are several variants of this representation [1–4] of the partition function. We will use a variant of the factorization method proposed previously [5] (omitting the ergodic theorem of H. Weyl and the related ergodic approximation) and subsequently developed in [6, 7].

Assuming that the central interatomic potential $v(\mathbf{r})$ admits expansion into the Fourier series, the pairwise energy of interaction between particles in the system can be written as

$$\frac{1}{2} \sum_{\substack{s,s'=1 \\ s\neq s'}}^{N} v(|\mathbf{R}_s - \mathbf{R}_{s'}|) = -\frac{N}{2}v(0) + \frac{1}{2V} \sum_{\mathbf{k}\in\Omega^+} v^+(\mathbf{k})[C^2(\mathbf{k}) + S^2(\mathbf{k})] - \frac{1}{2V} \sum_{\mathbf{k}'\in\Omega^-} v^-(\mathbf{k}')[C^2(\mathbf{k}') + S^2(\mathbf{k}')], \quad (2)$$

where

$$C(\mathbf{k}) = \sum_s \cos(\mathbf{k}\mathbf{R}_s); \quad S(\mathbf{k}) = \sum_s \sin(\mathbf{k}\mathbf{R}_s); \quad (3)$$

the term $-\frac{N}{2}v(0)$ compensates for the terms with $s = s'$ in the right-hand part of Eq. (2); $\Omega^\pm$ denotes the wavevector space parts in which the Fourier-transform $\tilde{v}(\mathbf{k})$ of the interatomic potential is positive and negative, respectively; and $v^\pm(\mathbf{k}) = \pm\tilde{v}(\mathbf{k})$ for $\mathbf{k} \in \Omega^\pm$.

The exponent related to the energy of two-body interactions in the generating functional (1) splits into the product over $\mathbf{k}$ and $\mathbf{k}'$ terms of the type $\exp\left(-\frac{\beta v^+(\mathbf{k})}{2V}[C^2(\mathbf{k}) + S^2(\mathbf{k})]\right)$, $\exp\left(\frac{\beta v^-(\mathbf{k}')}{2V}[C^2(\mathbf{k}') + S^2(\mathbf{k}')]\right)$. Performing the Stratonovich–Hubbard transformation for each of these terms, we obtain a generat-

ing functional representation via the functional integral

$$
\begin{aligned}
Z\{\varphi(\mathbf{r})\} &= \frac{V^N}{N!\lambda^{DN}} e^{\frac{\beta N}{2} v(0)} \\
&\times \int_{-\infty}^{+\infty} \cdots \int \left(\prod_{\mathbf{k} \in \Omega^+} \frac{\beta m \omega^2(\mathbf{k}) dx^+(\mathbf{k}) dy^+(\mathbf{k})}{2\pi} \right. \\
&\left. \times \exp\left\{ -\frac{\beta m \omega^2(\mathbf{k})([x^+(\mathbf{k})]^2 + [y^+(\mathbf{k})]^2)}{2} \right\} \right) \\
&\times \left(\prod_{\mathbf{k}' \in \Omega^-} \frac{\beta m \omega^2(\mathbf{k}') dx^-(\mathbf{k}') dy^-(\mathbf{k}')}{2\pi} \right. \\
&\left. \times \exp\left\{ -\frac{\beta m \omega^2(\mathbf{k}')([x^-(\mathbf{k}')]^2 + [y^-(\mathbf{k}')]^2)}{2} \right\} \right) \\
&\times [\mathcal{F}_1(x^{\pm}(\mathbf{k}), y^{\pm}(\mathbf{k}), \{\varphi(\mathbf{r})\})]^N.
\end{aligned} \tag{4}
$$

Here,

$$
\begin{aligned}
\mathcal{F}_1(x^{\pm}(\mathbf{k}), y^{\pm}(\mathbf{k}), \{\varphi(\mathbf{r})\}) &= \int_{(V)} \left\langle \frac{d\mathbf{R}}{V} e^{-\beta\varphi(\mathbf{R})} \right. \\
&\times \exp\left\{ i\beta \sum_{\mathbf{k} \in \Omega^+} \sqrt{\frac{m v^+(\mathbf{k})}{V}} \omega(\mathbf{k}) \right. \\
&\left. \left. \times [x^+(\mathbf{k}) \cos(\mathbf{kR}) + y^+(\mathbf{k}) \sin(\mathbf{kR})] \right\} \right. \\
&\times \exp\left\{ \beta \sum_{\mathbf{k}' \in \Omega^-} \sqrt{\frac{m v^-(\mathbf{k}')}{V}} \omega(\mathbf{k}') \right. \\
&\left. \left. \times [x^-(\mathbf{k}') \cos(\mathbf{k}'\mathbf{R}) + y^-(\mathbf{k}') \sin(\mathbf{k}'\mathbf{R})] \right\} \right\rangle,
\end{aligned} \tag{5}
$$

$\omega(\mathbf{k})$ is an arbitrary positive function of the wavevector with the dimensionality of the circular frequency; m is an arbitrary parameter with the dimensionality of mass, and $x^{\pm}(\mathbf{k})$ and $y^{\pm}(\mathbf{k})$ are the auxiliary variables appearing as a result of the Stratonovich–Hubbard transformation.

Upon representing Eq. (4) in the form of statistical integral of the system of interacting oscillators with the aid of identity

$$
\frac{\beta}{2\pi m} \int_{-\infty}^{+\infty} \int dp_x dp_y \exp\left[-\beta \left(\frac{p_x^2}{2m} + \frac{p_y^2}{2m} \right) \right] = 1, \tag{6}
$$

we obtain

$$
\begin{aligned}
Z\{\varphi(\mathbf{r})\} &= \frac{V^N}{N!\lambda^{DN}} e^{\frac{\beta N}{2} v(0)} \int_{-\infty}^{+\infty} \cdots \int \left(\prod_{\mathbf{k} \in \Omega^+} \left[\frac{\beta\omega(\mathbf{k})}{2\pi} \right]^2 \right. \\
&\left. \times dx^+(\mathbf{k}) dp_x^+(\mathbf{k}) dy^+(\mathbf{k}) dp_y^+(\mathbf{k}) \right) \left(\prod_{\mathbf{k}' \in \Omega^-} \left[\frac{\beta\omega(\mathbf{k}')}{2\pi} \right]^2 \right. \\
&\left. \times dx^-(\mathbf{k}') dp_x^-(\mathbf{k}') dy^-(\mathbf{k}') dp_y(\mathbf{k}') \right) \\
&\times [\mathcal{F}_1(x^{\pm}(\mathbf{k}), y^{\pm}(\mathbf{k}), \{\varphi(\mathbf{r})\})]^N \\
&\times \exp\left\{ -\beta \sum_{\mathbf{k} \in \Omega^+} \left(\frac{([p_x^+(\mathbf{k})]^2 + [p_y^+(\mathbf{k})]^2)}{2m} \right. \right. \\
&\left. \left. + \frac{m\omega^2(\mathbf{k})([x^+(\mathbf{k})]^2 + [y^+(\mathbf{k})]^2)}{2} \right) \right\} \\
&\times \exp\left\{ -\beta \sum_{\mathbf{k}' \in \Omega^-} \left(\frac{([p_x^-(\mathbf{k}')]^2 + [p_y^-(\mathbf{k}')]^2)}{2m} \right. \right. \\
&\left. \left. + \frac{m\omega^2(\mathbf{k}')([x^-(\mathbf{k}')]^2 + [y^-(\mathbf{k}')]^2)}{2} \right) \right\}.
\end{aligned} \tag{7}
$$

This integral represents a classical partition function of a system described by the Hamiltonian $\mathcal{H}$:

$$
\begin{aligned}
\mathcal{H} &= \sum_{\mathbf{k} \in \Omega^+} \left\{ \left[\frac{[p_x^+(\mathbf{k})]^2}{2m} + \frac{m\omega^2(\mathbf{k})(x^+(\mathbf{k}))^2}{2} \right] \right. \\
&\left. + \left[\frac{[p_y^+(\mathbf{k})]^2}{2m} + \frac{m\omega^2(\mathbf{k})(y^+(\mathbf{k}))^2}{2} \right] \right\} \\
&+ \sum_{\mathbf{k}' \in \Omega^-} \left\{ \left[\frac{[p_x^-(\mathbf{k}')]^2}{2m} + \frac{m\omega^2(\mathbf{k}')(x^-(\mathbf{k}'))^2}{2} \right] \right. \\
&\left. + \left[\frac{[p_y^-(\mathbf{k}')]^2}{2m} + \frac{m\omega^2(\mathbf{k}')(y^-(\mathbf{k}'))^2}{2} \right] \right\} \\
&- \frac{N}{\beta} \ln \mathcal{F}_1(x^{\pm}(\mathbf{k}), y^{\pm}(\mathbf{k}), \{\varphi(\mathbf{r})\}).
\end{aligned} \tag{8}
$$

Note that the term $2\pi/\beta\omega(\mathbf{k})$ in the integrand of Eq. (7) plays the role of a natural elementary cell of the phase space, that is, of the Planck constant, and has the same dimensionality.

Besides the "natural" variables—the generalized coordinates $x^{\pm}(\mathbf{k})$, $y^{\pm}(\mathbf{k})$ and generalized momenta $p_x^{\pm}(\mathbf{k})$, $p_y^{\pm}(\mathbf{k})$—Hamiltonian (8) contains the temperature implicitly entering into the function $\mathcal{F}_1(x^{\pm}(\mathbf{k}), y^{\pm}(\mathbf{k}), \{\varphi(\mathbf{r})\})$.

Thus, a study of the statistical properties of a system of classical particles interacting as described by an arbitrary pairwise potential (admitting expansion into the Fourier series) is equivalent to the study of a system of (quasi)particles (or elementary excitations) described by Hamiltonian $\mathcal{H}$. In this context, it would be of interest to study the systems described by this Hamiltonian.

Acknowledgments. This study was supported by the Federal Program "Universities of Russia," project no. 990019.

REFERENCES

1. D. N. Zubarev, Dokl. Akad. Nauk SSSR **95** (4), 757 (1954).
2. S. F. Edwards, Philos. Mag. **4**, 1171 (1959).
3. J. Hubbard and P. Schofield, Phys. Lett. A **40A** (3), 245 (1972).
4. A. L. Rebenko, Usp. Mat. Nauk **43** (3), 55 (1988).
5. A. Yu. Zakharov, Phys. Lett. A **147** (8/9), 442 (1990).
6. A. Yu. Zakharov and I. K. Loktionov, Teor. Mat. Fiz. **119** (1), 167 (1999).
7. A. Yu. Zakharov, Zh. Fiz. Khim. **74** (1), 48 (2000).

Translated by P. Pozdeev

Technical Physics Letters, Vol. 27, No. 7, 2001, pp. 563–566. Translated from Pis'ma v Zhurnal Tekhnicheskoĭ Fiziki, Vol. 27, No. 13, 2001, pp. 76–83.

Measurement of the Internal Conversion Electron Lines by the Track Counting Technique

T. A. Islamov, V. G. Kalinnikov, N. T. Kambarova, T. M. Muminov, N. A. Lebedev, A. A. Solnyshkin, Yu. D. Aleshin, V. V. Kolesnikov, and V. I. Silaev

Joint Institute for Nuclear Research, Dubna, Moscow oblast, 141980 Russia

Institute of Applied Physics, Tashkent State University, Tashkent, Uzbekistan

Institute of Theoretical and Experimental Physics, State Research Center of the Russian Federation, Moscow, 117259 Russia

Received November 9, 2000

Abstract—The internal conversion electron lines were measured by the method of track counting in a nuclear photoemulsion with the aid of an optical microscope and an MAS-1 automated TV setup. © *2001 MAIK "Nauka/Interperiodica".*

Introduction. An important role in the experimental nuclear spectroscopy belongs to high-precision beta spectrographs using constant magnetic field. Possessing relatively simple design, these instruments are also simple in use and offer a number of advantages in determining the energies, intensities, and multiplicities of nuclear gamma transitions [1].

Owing to the high energy resolution and broad energy range covered in one measurement, beta-spectrographic complexes were widely used in the 1950s–1980s for the nuclear spectrometry of radionuclides [2]. However, a relatively low transmission of beta spectrographs, limited sensitivity of the photographic plates, low accuracy of the photometric measurements, and the requirement of high activity of the sources employed restrict the possibility of using these systems for the investigation of short-living radionuclides and for the measurement of low-intensity electron lines in the internal conversion spectra.

One of the possible ways to increase the sensitivity and accuracy of beta-spectrographic measurements is to use the track-counting technique instead of photometric (optical density) measurements on photographic plates [3–5]. The tracks of focused and scattered electrons possess different shapes, which allows the lines of internal conversion electrons (ICEs) to be distinguished even against a high background level.

A considerable volume of experimental data has been accumulated at the Laboratory of Nuclear Problems of the Joint Institute for Nuclear Research (JINR) over four decades of operation of a beta-spectrographic complex designed at the Tashkent State University. The ICE spectra of more than one hundred radionuclides of rare-earth elements, astatine, and actinium are now stored on the photographic plates. A large proportion of this information is inaccessible for processing the ICE lines by the photometric technique. However, these data can be recovered by the method of electron track counting on the photographic plates.

Below, we describe a procedure developed for the track counting on the ICE beta spectrograms recorded on 400×15 mm photographic plates of the R-50 type.

Experiment. The beta particle spectrograms of various isotopes prepared as thin-film sources were recorded using beta spectrographs with an energy resolution of 0.03–0.06% and a transmission of 0.01% [2]. For this purpose, an isotope of fragments was obtained on Ta, Er, Cd, W, Au, and some other targets spalled in the inner proton beam of the JINR phasotron (E_p = 660 MeV). The corresponding isotope fractions were isolated by radiochemical methods [6]. These isotopes were electrolytically deposited onto platinum wires (10–100 μm in size), which were mounted in the beta spectrograph and used as the sources irradiating photographic plates.

Photographic plate processing. The exposed photographic plates containing data on the weak ICE lines can be successfully processed by the method of track counting in the photoemulsion [3–5]. This technique was used to measure the ICE spectra of ^{137}Cs (T = 30.1 year), ^{198}Tl (T = 5.3 h), ^{206}Tl, and ^{212}Pb radionuclides recorded at a beta spectrograph resolution of 0.02–0.04%. Anton'eva [3] measured the K, L, and M ICE lines of the γ transition with an energy of 661.6 keV. Reitman and Schneider [4] studied the L_1, L_2, and L_3 ICE lines of the 411.8 keV transition in ^{198}Hg. Sevier [5] measured the low-energy $L_{1–3}$ and $M_{1–3}$ ICE lines of the γ transition with an energy of 39.8 keV in ^{208}Tl and the K lines of the 115.7 keV transition in ^{212}Bi. It should be noted that the accuracy of the ICE line intensity determination in these measurements did not exceed 8% [3–5].

1063-7850/01/2707-0563$21.00 © 2001 MAIK "Nauka/Interperiodica"

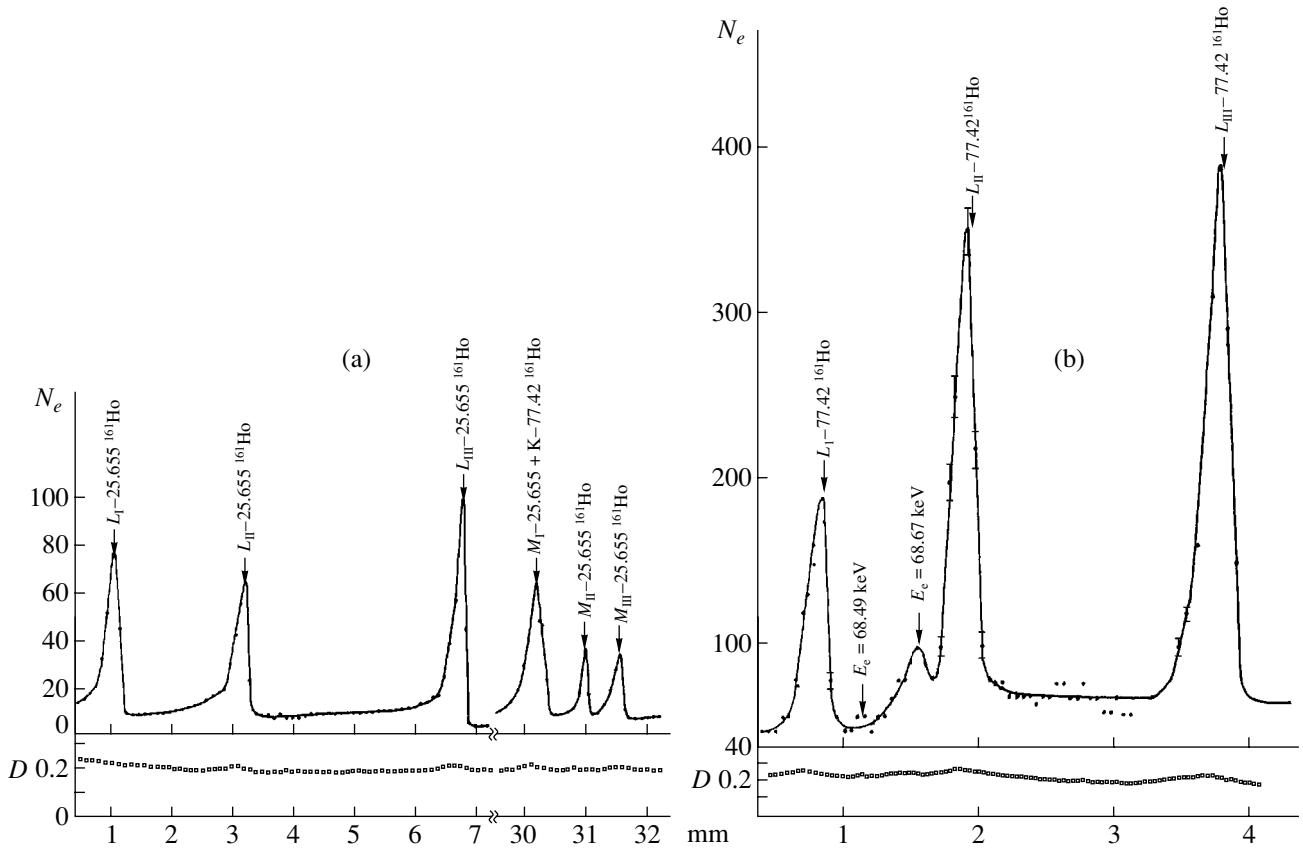

Fig. 1. The ICE spectra of ^{161}Ho obtained by the methods of photometry (symbols *D*, optical density) and track counting (solid curves N_e, track/250 μm^2).

In this study, we counted the ICE tracks in the photoemulsions for $L_{1–3}$, $M_{1–3}$ (25.655 keV) and $L_{1–3}$ (74.42 keV) lines of ^{161}Ho and for some ICE lines of ^{163}Tm, ^{166}Tm, and ^{135}Ce nuclei. The ICE track counting procedure was used to process the photographic plates with a low background level. The data were obtained with the aid of an optical microscope of the MBI-9 type operated at a magnification of 900 and 1350. Figures 1a and 1b shows the regions of the ICE spectrum of ^{161}Ho with a source activity below 1 mCi obtained by the methods of track counting and photometry. Data on the relative intensities of 25.655 and 77.42 keV lines in the spectra of ^{161}Ho are listed in the table in comparison with the results of calculations using the theory [8]. A comparison of these values shows that multiplicities of the 25.655 and 77.42 keV transitions belong to the *E*1 type.

Data on the relative intensities of 25.655 and 77.42 keV ICE lines ($L_{1–3}$) in the γ transition spectra of ^{161}Ho

Energy E_γ, keV	Intensity ratio	Experiment	Theory	Multiplicity assignment
25.655	$L_1 : L_2$	1.40	1.37	*E*1
	$L_2 : L_3$	0.70	0.68	
	$L_1 : L_3$	0.93	0.94	
77.42	$L_1 : L_2$	3.60	3.59	*E*1
	$L_2 : L_3$	0.80	0.80	
	$L_1 : L_3$	2.88	2.86	

Figure 2 shows a curve of the track length versus electron energy plotted using the data from [3–5] and our results. This plot indicates that the ICE track counting must be performed using a microscope magnification of 2700 because electrons with an energy below 16 keV are characterized by a track length shorter than 4 μm. According to the spectral sensitivity characteristic of the R-50 photographic plates, the electron track length increases with the particle energy up to 200 keV [1–2], after which the number of emulsion grains is no longer changing with the electron energy. The tracks of electrons possessing different energies can be distinguished by the number of grains crossed by the track, the track length, and the scattering angle. We used the track counting method to process the ICE lines for the following transitions: ^{166}Tm (*K*–194.8 keV), ^{169}Yb (*K*–197.97 keV), ^{160}Ho (*K*–218.1 keV), ^{135}Cr (L_1, L_2, L_3–59.08 keV, *K*–146.2 keV, *K*–162.1 keV,

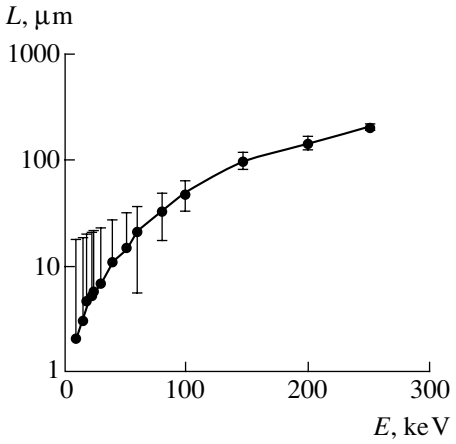

Fig. 2. The plot of track length L in a photoemulsion versus electron energy E.

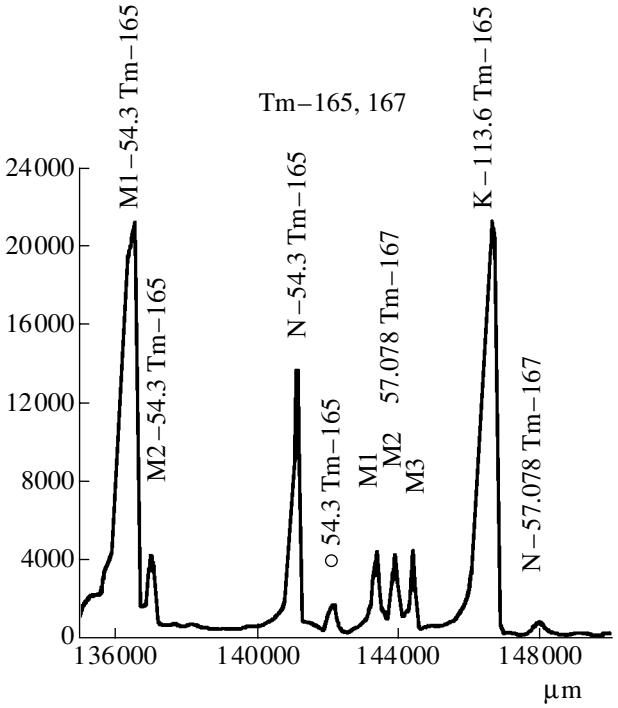

Fig. 3. An ICE spectrum of a radioactive ^{165,167}Tm fraction obtained with the aid of a MAS-1 automated track counting system.

K–572.0 keV, K–665.4 keV, K–783.3 keV, K–828.2 keV), and ^{160}Ho (L_1, L_2, L_3, M_2, M_3, N_-, O_-–86.49 keV).

The track counting method provides interesting results, but the manual data processing on an optical microscope is not a promising course of action. The first task is to develop an automated procedure for the track counting in photoemulsions.

Photographic plate processing on a MAS-1 automated setup. Use of the TV cameras for obtaining digitized images of the nuclear photoemulsions opens new possibilities in the beta-spectrographic data processing. A universal automated setup of the MAS-1 type [7] is based on the principle of TV readout, digitization, and transfer of the data to computer. Subsequent computer processing and filtration of the data array allows the automated determination of the number of black pixels belonging to grains in the exposed emulsion. A TV camera employing a 1/2″ CCD-matrix decomposes a focused image into a pattern of 512 × 512 pixels. A 400 × 400 mm photographic plate is scanned with the aid of a microscope objective lens using a 60- to 300-μm-wide field of vision.

The track point coordinates in a 3D space over the working table are determined to within 1 μm using grating-based position sensors. The positioning accuracy within the same field of vision may reach up to 0.2 μm. Each cell of the image recorded is provided with a value characterizing the brightness (1–256 unit scale). Therefore, each field of vision occupies 256 kB of the computer memory. A field of vision scanned with a 40^x objective covers 100 μm, which corresponds to 5 pixels per micron. At this resolution, a single grain occupies about 20 pixels in the shot. Therefore, a TV camera operated in this regime allows the optical image to be scanned on the grain level. A special filtration procedure involved in the image digitization procedure ensures the obtaining of reliable data.

Figure 3 shows an example of the ICE spectrum of a radioactive ^{165,167}Tm fraction obtained with the aid of an MAS-1 system.

Conclusion. An analysis of various methods used for the beta-spectrographic ICE measurements with the photographic registration reveals the following features.

1. The ICE track counting on photographic plates provides for a significantly higher sensitivity as compared to the photometric measurements, which is related primarily to the possibility of distinguishing ICE tracks from the tracks of scattered electrons.

2. The possibility of processing beta spectrograms implies the use of high-activity sources, which is related to a limited sensitivity of the photometric method (the minimum sensitivity of a photographic plate is 5000 tracks per 0.3 mm line width).

3. During the photometry, the ICE line width additionally increases due to the finite slit width of the entrance aperture of the photometric detector.

4. The method of track counting allows using sources with a specific activity 1000 times lower as compared to the case of photometric processing.

5. Using an automated spectrometric microscope of the MAS-1 type with a TV data readout for the ICE track counting on the photographic plates ensures a still higher accuracy in determining the line position (to within a few microns), while retaining the intensity sensitivity on the level of a few grains.

REFERENCES

1. A. A. Abdurazakov, K. Ya. Gromov, and G. Ya. Umarov, *Beta-Ray Spectrographs with Permanent Magnets* (FAN, Tashkent, 1970).
2. A. A. Abdurazakov, T. A. Islamov, *et al.*, *Atlas of Spectra of Internal Conversion Electrons of Neutron-Deficient Radioactive Nuclides in A=131–172 Interval* (Uzbekistan, Tashkent, 1991).
3. I. A. Anton'eva, Zh. Éksp. Teor. Fiz. **30**, 571 (1956) [Sov. Phys. JETP **3**, 461 (1956)].
4. D. Reitman, H. Schneider, *et al.*, Nucl. Instrum. Methods **22**, 345 (1963).
5. K. D. Sevier, Ark. Fys. **25** (7), 87 (1963).
6. F. Molnar, V. Halkin, and É. Hermann, Fiz. Élem. Chastits At. Yadra **4**, 1077 (1973) [Sov. J. Part. Nucl. **4**, 440 (1973)].
7. Yu. D. Aleshin, V. V. Kolesnikov, and V. I. Silaev, Prib. Tekh. Éksp., No. 2, 49 (1997).
8. R. S. Hager and E. C. Soltzer, Nucl. Data Tables A **6**, 1 (1969).

Translated by P. Pozdeev

Technical Physics Letters, Vol. 27, No. 7, 2001, pp. 567–569. Translated from Pis'ma v Zhurnal Tekhnicheskoĭ Fiziki, Vol. 27, No. 13, 2001, pp. 84–89.

Magnetooptical and Magnetic Properties of Granular Cobalt–Porous Silicon Nanocomposites

A. N. Vinogradov, E. A. Gan'shina, V. S. Guschin, V. M. Demidovich, G. B. Demidovich, S. N. Kozlov*, and N. S. Perov

Moscow State University, Moscow, 119899 Russia

** e-mail: kozlov@vega.phys.msu.su*

Received November 30, 2000

Abstract—The magnetooptical and magnetic properties of porous silicon containing electrochemically incorporated cobalt microgranules were studied. It was found that the granular cobalt–porous silicon nanocomposites exhibit ferromagnetic properties. The nanocomposite with a cobalt content of 10% showed anomalously high magnitude of the equatorial Kerr effect. © *2001 MAIK "Nauka/Interperiodica".*

An important task in the present stage of development of the silicon-based microelectronics is the search for new ways to increase the functional possibilities of semiconductor devices. In particular, good prospects in the development of optoelectronic elements and sensors within the framework of the silicon technology were opened by the discovery of intense luminescence from porous silicon (por-Si) [1]. However, the magnetic and magnetooptical properties of materials compatible with the silicon technology are much less studied and virtually not implemented in practice.

There were a few attempts at studying the magnetic properties of porous silicon [2–4], which led the researchers to rather contradictory conclusions. The results obtained in [2] showed the absence of any significant magnetic effects in porous silicon, while other data [3, 4] showed certain signs of ferromagnetism in this material. At the same time, it is known that low-dimensional composites of the ferromagnetic metal–insulator type exhibit magnetic properties that are of considerable interest in practical applications, such as the giant magnetoresistance, spin-dependent conductivity, and nonlinear magnetooptical effects.

Below, we present the results of our investigations of the magnetic and magnetooptical properties of a new composite material representing a porous silicon matrix with incorporated microgranules of ferromagnetic cobalt.

The layers of porous silicon with a thickness of 5–20 μm, a total porosity of 75–80%, and an average pore size of a few nanometers were created on the surface of (100)-oriented *p*-silicon single crystals anodized in an HF–ethanol (1 : 1) solution at a current density of 20 mA/cm^2. The metal microgranules were electrochemically incorporated into the por-Si layer by processing the samples in an ethanol solution of $CoCl_2$. The total amount of incorporated metal was determined by measuring the charge transferred through the silicon–electrolyte interface. The content of cobalt in the por-Si layer was calculated as a ratio of the total incorporated metal mass to the mass of silicon present in the porous layer.

The magnetooptical (MO) properties of the por-Si–Co nanocomposites were studied by measuring the equatorial (magnetooptical) Kerr effect (EKE), whereby the intensity of light reflected from a sample changes upon magnetization of this sample. The MO spectra were measured for the light quanta with the energies ranging from 1.3 to 3.8 eV at a light incidence angle of 70° and a magnetic field strength of up to 2.5 kOe. The magnetization hysteresis was measured on a vibrating-sample magnetometer-anisometer using a magnetic field strength of up to 8 kOe. All magnetic measurements were conducted at room temperature.

It was found that both the character of the EKE spectra $\delta(h\nu)$ and the magnitude of the Kerr effect strongly depend on the nanocomposite parameters (porous layer thickness and the relative content of the ferromagnetic component). The data presented in Fig. 1 show that the EKE spectra of nanocomposites containing 5–30% Co (curves *1–4*) significantly deviate from the spectrum of pure cobalt (curve *5*). As is seen, the difference is manifested both in shape of the curves and in sign of the Kerr effect (for the samples with small cobalt content). The EKE value exhibits a nonmonotonic variation depending on the metal content: certain compositions (in particular, some samples containing 10% Co) showed anomalously large effect reaching $\delta \cong -10^{-2}$ at a light quantum energy of 2.6 eV (the absolute δ values for pure cobalt measured under analogous conditions were about five times lower).

The MO properties also strongly depend on the technological conditions of the porous silicon preparation and the microgranular metal incorporation. Even small variations in the process parameters such as the anodic current density, temperature, or electrolyte con-

1063-7850/01/2707-0567$21.00

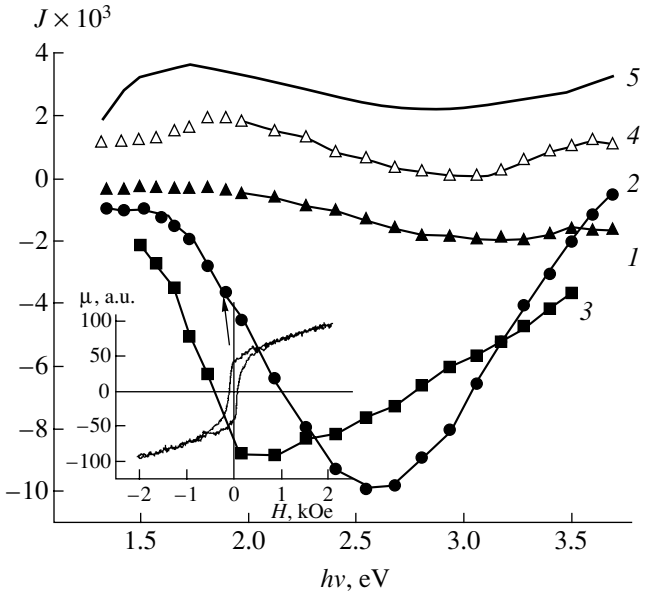

Fig. 1. EKE spectra of porous silicon–cobalt nanocomposites containing (*1*) 5%, (*2*, *3*) 10%, and (*4*) 20% Co in comparison with the spectrum of (*5*) a bulk cobalt sample. The inset shows a plot of the magnetization versus magnetic field strength for sample *2*.

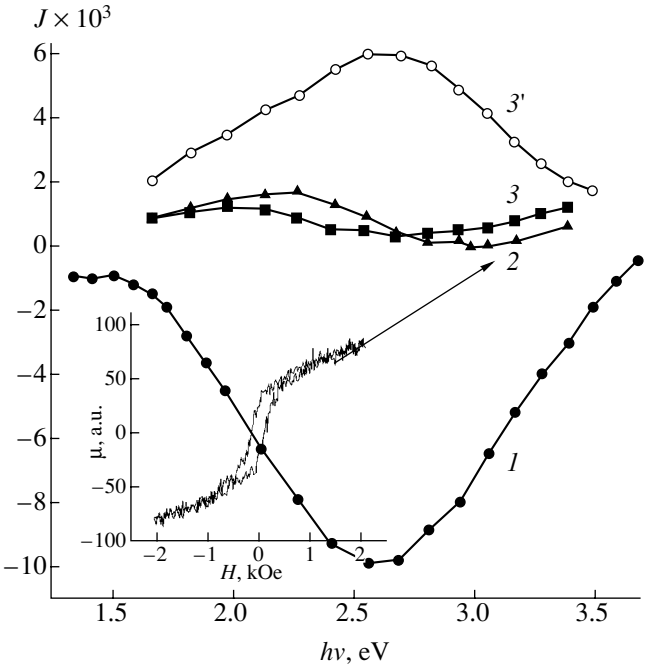

Fig. 2. EKE spectra of porous silicon–cobalt nanocomposite samples with the same (10%) cobalt content prepared in different technological cycles (*1–3*, *3*'). Curves *3* and *3*' were obtained for the same sample measure at the center and at the edge of the plate, respectively. The inset shows a plot of the magnetization versus magnetic field strength for sample *2*.

centration led to significant changes in the MO properties of the nanocomposite. For example, Fig. 2 presents the EKE spectra of several por-Si–10% Co samples prepared in different technological cycles. As is seen, the EKE value in the region of 2.5 eV varies in this series of samples from $+6 \times 10^{-3}$ to -1×10^{-2}. Moreover, the shape of the spectrum may even differ in various areas of the same nanocomposite sample (cf. curves *3* and *3*' in Fig. 2). Measured in the sample areas close to the edge, the EKE spectrum is similar to that of pure cobalt (curve *5* in Fig. 1). This behavior agrees with the tendency of metals to deposit at the substrate edges—a general trend in electrochemical deposition processes.

At the same time, measurements of the volume magnetic properties of samples containing equal amounts of cobalt (even possessing different EKE values) gave virtually identical results. The magnetization hysteresis loops (see insets in Figs. 1 and 2) show that the Co–Si films studied are magnetically hard, possess a coercive force ~100 kOe, and do not exhibit saturated magnetization in the fields up to 2 kOe. These data confirm that an average volume concentration of the magnetic component is the same in all samples irrespective of their MO properties (EKE values).

An apparent discrepancy between the results of magnetic and magnetooptical measurements is evidently explained by the fact that the magnetic properties of nanocomposites are determined by the total cobalt content in the porous silicon matrix, whereas the MO behavior depends on the amount and structure of Co microgranules only in the upper por-Si layer. Taking into account that the optical absorption coefficient of the por-Si based composite in the spectral range studied is not less than 10^3 cm^{-1} [5], the MO measurements in this range characterize the upper layer of the nanocomposite with a thickness on the order of (or less than) one micron. From this we may infer that the distribution of cobalt in the por-Si layer is rather inhomogeneous, with the metal concentration increasing on approaching the inner boundary of the por-Si layer.

Previously, analogous variations of the MO spectra depending on the technological conditions were observed for ultradisperse cobalt [6] and Co_xPd_{1-x} alloy films with low cobalt content [7]. Transformations in the $\delta(h\nu)$ spectra observed in our experiments are typical of the microscopically inhomogeneous magnetic media and are usually observed upon a variation of the parameters such as the volume fraction of a ferromagnetic phase in a composite and the shape and size of the ferromagnetic grains [6, 8, 9]. Note that the MO properties of ferromagnet–insulator composites are determined by the optical characteristics of both the porous matrix and the ferromagnetic component [6], the MO parameters of the ferromagnet, and the sample microstructure (i.e., the size and shape of ferromagnetic particles and their environment) [7].

On the whole, the results of our investigation showed that the proposed method can be used for the synthesis of porous silicon–ferromagnetic metal nanocomposites possessing unusual properties of interest in practical applications. The magnetic and magnetoopti-

cal methods offer an effective tool for the characterization of microstructure and composition of these new composite materials.

REFERENCES

1. L. T. Canham, Appl. Phys. Lett. **57** (10), 1046 (1990).
2. C. Y. Perry, F. Lu, F. Namavar, *et al.*, Appl. Phys. Lett. **60** (25), 3117 (1992).
3. R. Laiho, E. Lahderanta, L. Vlasenko, and M. Afanasiev, J. Lumin. **57** (1–6), 197 (1993).
4. M. E. Kompan, I. Yu. Shibanov, and Ya. Salonen, Fiz. Tverd. Tela (St. Petersburg) **41** (1), 54 (1999) [Phys. Solid State **41**, 45 (1999)].
5. V. Yu. Timoshenko, E. A. Konstantinova, and T. Dittrich, Fiz. Tekh. Poluprovodn. (St. Petersburg) **32** (5), 613 (1998) [Semiconductors **32**, 549 (1998)].
6. L. V. Nikitin, L. S. Mironova, V. V. Litvintsev, and V. V. Katkevich, Fiz. Met. Metalloved., No. 2, 92 (1991).
7. E. Gan'shina, V. Guschin, I. Romanov, and A. Tselev, J. Magn. Magn. Mater. **185** (3), 258 (1998).
8. E. Gan'shina, R. Kumaritova, A. Bogoroditsky, *et al.*, J. Magn. Soc. Jpn. **23**, 379 (1999).
9. E. Gan'shina, A. Granovsky, V. Guschin, *et al.*, Physica A (Amsterdam) **241** (1), 45 (1997).

Translated by P. Pozdeev

Technical Physics Letters, Vol. 27, No. 7, 2001, pp. 570–571. Translated from Pis'ma v Zhurnal Tekhnicheskoĭ Fiziki, Vol. 27, No. 13, 2001, pp. 90–94.

Calculation of the Shear Energy Profile in Alloys with DO_{19} Superstructure

E. V. Chernyh, M. A. Baranov, and M. D. Starostenkov

Altai State Technical University, Barnaul, Russia

e-mail: asba@altline.barrt.ru

Received November 2, 2000

Abstract—The shear energy surfaces in Mg_3Cd and Ti_3Al alloys possessing a DO_{19} superstructure were studied by computer simulation with an allowance of the crystal lattice anisotropy. Stable planar defects in the (0001) basal plane are revealed. © *2001 MAIK "Nauka/Interperiodica".*

Investigation of the energetics of planar defects of the shear type provides very important information about the course of plastic deformation. In recent years, a most effective method for the study of planar defects has been offered by computer simulation of the shear energy profile (γ profile) [1, 2]. Previously, the shapes of γ surfaces were most thoroughly studied in the ordered alloys with superstructures, based on body- (bcc) and face-centered cubic (fcc) crystal lattices [3–5]. At the same time, the defects in alloys with superstructures based on hexagonal close-packed (hcp) structures were basically not studied by computer modeling. The traditional spherically symmetric pairwise interatomic potentials have proved to be inapplicable to modeling the planar defects in hcp lattices: no physically acceptable spectra of the energies of defect formation were obtained using these potentials.

In this study, the planar defect formation was simulated using a semiempirical pairwise interatomic potential for an A–B type bond, which reflects the anisotropy of the hcp crystal:

$$\varphi_{AB}(r, \theta) = (1 + \zeta_{AB}\cos^2\theta)\varphi_{M_{AB}}(r),$$

where φ_M is the spherically symmetric Morse function, θ is the angle measured from the principal crystal axis, and ζ is a parameter. The energy profile was calculated for A_3B alloys with a DO_{19} superstructure, with a semicrystal sliding in the (0001) basal plane. The atomic configuration of this plane comprises four sublattices *1–4* as depicted in Fig. 1, where the positions of lattice sites belonging to these sublattices are indicated by numbers (atoms of the "bottom" layer are shown by smaller circles). The most probable sliding directions in the plane

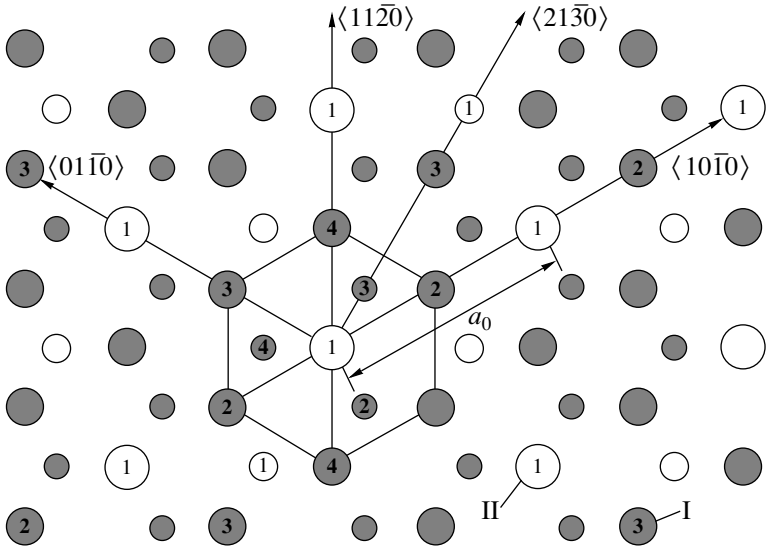

Fig. 1. Projection of a DO_{19} superstructure in an A_3B alloy onto the (0001) plane showing lattice sites occupied by (I) A-type and (II) B-type atoms. Figures in the circles indicate sublattice numbers (*1–4*); a_0 is the lattice parameter.

1063-7850/01/2707-0570$21.00 © 2001 MAIK "Nauka/Interperiodica"

under consideration are $\langle 21\bar{3}0 \rangle$ and $\langle 10\bar{1}0 \rangle$ (indicated by arrows in Fig. 1).

The potential relief was simulated proceeding from a starting defect configuration representing the two semicrystals sheared relative to each other by a preset vector, with the crystal edges being fixed. Atoms in the inner regions were allowed to shift under the action of resultant forces until an equilibrium configuration was attained.

Figure 2 shows a γ surface profile for the $\langle 21\bar{3}0 \rangle$ shear direction in the close-packed sliding system of a Mg_3Cd alloy obtained for the shear vector changing from $-a_0\langle 21\bar{3}0 \rangle$ to $a_0\langle 21\bar{3}0 \rangle$. Owing to the ordered arrangement in the nodes of the DO_{19} superstructure, the energy profile exhibits two quasiperiods corresponding to the semicrystal shift from 0 to $(a_0/2)\langle 21\bar{3}0 \rangle$ and from 0 to $-(a_0/2)\langle 21\bar{3}0 \rangle$. The two quasiperiods differ in magnitude of the energy minima and in height of the potential barriers, which reflects a translational symmetry of this particular superstructure. The starting and final configurations are described by the thin and thick solid profiles, respectively. A shear by the vector $(a_0/6)\langle 21\bar{3}0 \rangle$ into positions *1* and *4* leads to the formation of a local energy minimum, which corresponds to the formation of a superstructural stacking fault (SSF). A deeper minimum, appearing upon a relative shift of the semicrystals by $(a_0/2)\langle 21\bar{3}0 \rangle$ into positions *2* and *5*, corresponds to a stable state of the crystal containing an antiphase boundary (APB). Subsequent shear of the semicrystal from this state by $(a_0/6)\langle 21\bar{3}0 \rangle$ into positions *3* and *6* leads to the formation of a complex stacking fault (CSF). Evidently, a shear by the full vector $\pm a_0\langle 21\bar{3}0 \rangle$ restores the ideal lattice structure. A characteristic feature is that the SSF formation energy (~100 mJ/m^2) is higher than the energies of APB (~20 mJ/m^2) and CSF (~50 mJ/m^2). These estimates agree well with the experimental data for APB (~22 mJ/m^2) in Mg_3Cd [6]. Therefore, the SSF may split with the formation of APB and CSF according to the scheme

$$\frac{1}{6}\langle 21\bar{3}0\rangle \longrightarrow \frac{1}{2}\langle 21\bar{3}0\rangle - \frac{1}{3}\langle 21\bar{3}0\rangle.$$

In Ti_3Al, the calculated formation energies of SSF and CSF are close to ~120 mJ/m^2 and the value for APB is ~60 mJ/m^2. In this alloy, no mutual transformation of the planar defects as a result of the dislocation reactions should be expected.

A simpler shape was obtained for a shear energy profile in the $\langle 10\bar{1}0\rangle$ direction. In this case, the conditions of translational and mirror symmetry are obeyed that is manifested by equal values of the energies corresponding to shear in the opposite directions. The shear by $(a_0/2)\langle 21\bar{3}0\rangle$ in Mg_3Cd leads to the formation of only APBs with an energy of ~17 mJ/m^2; no other minima were obtained in this system. The energies of planar defect formation in the other planes were higher by one order of magnitude, which also agrees with the data reported in [6].

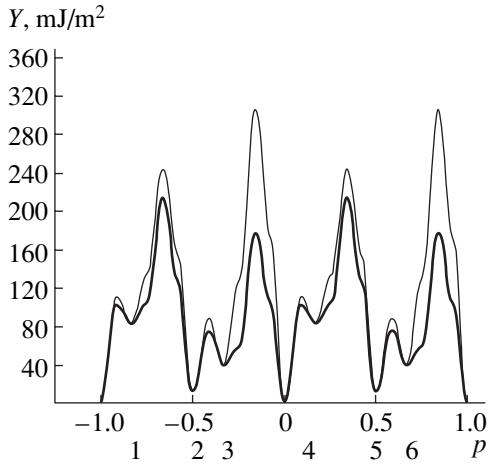

Fig. 2. Dependence of the energy profile on the value of the shear vector $pa_0\langle 21\bar{3}0 \rangle$ in the (0001) plane in Mg_3Cd alloy.

Thus, the aforementioned defects in the (0001) principal sliding plane represent the whole set of stable planar defects possible in superstructures based on the hcp crystal lattice, which is likely to be related to the anisotropy of this structure.

REFERENCES

1. M. Yamaguchi and Y. Umakoshi, in *Materials Science Monographs*, Vol. 20: *The Structure and Properties of Crystal Defects*, Ed. by V. Paidar and L. Lejcek (Elsevier, Amsterdam, 1984), p. 131.
2. *Materials Science Monographs*, Vol. 20: *The Structure and Properties of Crystal Defects*, Ed. by V. Paidar and L. Lejcek (Elsevier, Amsterdam, 1984), p. 463.
3. T. I. Novichikhina, M. A. Baranov, and M. D. Starostenkov, Pis'ma Zh. Tekh. Fiz. **22** (5), 81 (1996) [Tech. Phys. Lett. **22**, 218 (1996)].
4. M. A. Baranov, A. G. Nikiforov, and M. D. Starostenkov, Pis'ma Zh. Tekh. Fiz. **24** (12), 68 (1998) [Tech. Phys. Lett. **24**, 485 (1998)].
5. M. D. Starostenkov and V. V. Romanenko, Izv. Vyssh. Uchebn. Zaved., Chern. Metall., No. 6, 46 (1993).
6. L. S. Bushnev and L. P. Kitaeva, Kristallografiya **9** (6), 879 (1964) [Sov. Phys. Crystallogr. **9**, 740 (1964)].

Translated by P. Pozdeev

Technical Physics Letters, Vol. 27, No. 7, 2001, pp. 572–574. Translated from Pis'ma v Zhurnal Tekhnicheskoĭ Fiziki, Vol. 27, No. 14, 2001, pp. 1–5.

Envelope Shock Waves in Nonlinear Systems with Mode Coupling

I. O. Zolotovskiĭ and D. I. Sementsov

Ul'yanovsk State University, Ul'yanovsk, Russia

e-mail: sdi@sdi.ulsu.ru

Received November 23, 2000

Abstract—It is shown that the dispersion of nonlinearity in waveguide structures admitting strong linear coupling between two unidirectional waves significantly affects the dynamics of the wave packet propagation. In a nonamplifying medium, there is a principal possibility (not inherent in one-wave structures) that an envelope shock wave would form on the leading front of the wave packet. *© 2001 MAIK "Nauka/Interperiodica".*

Among the problems of nonlinear fiber optics actively discussed in recent years, a special place belongs to the properties of waves propagating in distributed-coupling systems. This is explained by broad prospects in the practical application of such systems [1–3]. Such coupled wave formations usually appear in tunnel-coupled, anisotropic or periodic optical waveguide (OWG) structures [1, 4]. In this context, it is important to study the dynamics of short pulse propagation in such OWGs with an allowance for various nonlinear effects [5–7].

One of the practically significant nonlinear effects taking place in singe-mode OWGs is the trailing front "steepening" and the envelope shock wave formation on the pulse "tail," which is related to the group velocity dependence on the pulse intensity [8]. In amplifying media, the envelope steepening may also take place on the leading front due to its predominant amplification [9]. However, no evidence of the possible shock wave formation on the leading front was reported in the literature. Below we demonstrate for the first time the principal possibility of the shock wave formation on the leading front of a wave packet in a nonamplifying OWG admitting the propagation of two unidirectional linearly coupled waves.

The system of equations describing time-dependent envelopes of the two coupled waves forming a wave packet (in terms of the current time $\tau = t - z/u$, where u is the group velocity of the wave packet) with an allowance for the mode mismatch of the group velocities and the nonlinear effects of the phase self- and cross-modulation is as follows:

$$\frac{\partial A_j}{\partial z} + \frac{(-1)^j}{v}\frac{\partial A_j}{\partial \tau} = -i\sigma A_{3-j} - iR(\gamma_s|A_j|^2 + \gamma_c|A_{3-j}|^2)A_j - \frac{2R}{\omega_0}\frac{\partial}{\partial \tau}[(\gamma_s|A_j|^2 + \gamma_c|A_{3-j}|^2)A_j], \quad j = 1, 2. \tag{1}$$

Here, $v^{-1} = (u_1 - u_2)/2u^2$, $u_j = (\partial\beta_j/\partial\omega)^{-1}_{\omega_0}$ is the group velocity of the jth mode, $2u = u_1 + u_2$; R is the OWG nonlinearity parameter; ω_0 is the wave packet carrier frequency; σ is the mode coupling coefficient; γ_s and γ_c are the self- and cross-modulation parameters, respectively [8]. Equations (1) must be solved jointly with the initial conditions for the time-dependent mode envelopes A_j. These conditions can be written in the general form $A_2(\tau, 0) = \psi A_1(\tau, 0)$, where ψ is a parameter determining the OWG excitation type. In particular, $\psi = \pm 1$ corresponds to symmetric and antisymmetric fiber excitation, respectively. In the strong mode coupling approximation, a solution to system (1) can be represented as a sum of two partial pulses (PPs):

$$A_j = (-1)^{j+1}a_1(\tau, z)\exp(i|\sigma|z) + a_2(\tau, z)\exp(-i|\sigma|z), \tag{2}$$

where a_f are the PP amplitudes slowly varying with the z coordinate.

If the initial conditions correspond to symmetric or antisymmetric OWG excitation, the amplitude of one PP is zero: $a_1 = 0$ in the symmetric and $a_2 = 0$ in the antisymmetric case [7, 10]. The general system of two equations for PPs degenerates into a single equation

$$\frac{\partial a_f}{\partial z} + iR(\gamma_c + \gamma_s)|a_f|^2 a_f + \chi_1\frac{\partial}{\partial \tau}(|a_f|^2 a_f) + (-1)^f\chi_2 a_f\frac{\partial}{\partial \tau}|a_f|^2 = 0, \tag{3}$$

where $\chi_1 = 2R(\gamma_c + \gamma_s)/\omega_0$ and $\chi_2 = R(\gamma_c + \gamma_s)/2v|\sigma|$. A solution to this equation can be written in the form of

$a_f = \rho_f \exp(i\phi_f)$, where ρ_f and ϕ_f are real pulse amplitudes and phases, respectively. Substituting this expression into Eq. (3) and separating the real and imaginary parts in the initial equation, we obtain an equation for the PP amplitude describing the pulse shape:

$$\frac{\partial \rho_f}{\partial z} + (3\chi_1 + (-1)^f 2\chi_2)\rho_f \frac{\partial \rho_f}{\partial \tau} = 0. \quad (4)$$

Let us consider a Gaussian pulse entering an optical fiber. For $z = 0$, this pulse obeys the relationship

$$\rho_f(\tau; 0) = \rho_{f0} \exp(-\tau^2/2\tau_0^2), \quad (5)$$

where τ_0 is the initial pulse duration. A solution to this equation for the amplitude $\rho_f(\tau, z)$ can be written in an implicit form

$$\rho_f(\tau; z) = \rho_{f0} \times \exp(-[\tau - (3\chi_1 + (-1)^f 2\chi_2)\rho_f^2(\tau; z)z]^2/2\tau_0^2). \quad (6)$$

According to relationship (6), the pulse envelope maximum propagates in the OWG at a velocity of

$$u_m = \frac{u}{1 + (3\chi_1 + (-1)^f 2\chi_2)u\rho_{f0}^2}. \quad (7)$$

For $3\chi_1 + (-1)^f 2\chi_2 > 0$, the pulse maximum propagates at a velocity that is smaller than the group velocity of the wave packet in a given medium. As a result, the maximum shifts toward the trailing front and the pulse tail exhibits steepening. This leads eventually to the appearance of a discontinuity ($\partial\rho/\partial\tau \longrightarrow \infty$) and the formation of an envelope shock wave. In the case of $3\chi_1 + (-1)^f 2\chi_2 < 0$ (which is possible for the antisymmetric OWG excitation), the pulse maximum propagates at a velocity exceeding that of the pulse wings. In this case, the steepening followed by the discontinuity formation ($\partial\rho/\partial\tau \longrightarrow -\infty$) takes place on the leading front. The propagation length at which the envelope shock wave is formed in both cases is given by the formula

$$L_p = \frac{(e/2)^{1/2}\tau_0}{|(3\chi_1 + (-1)^f 2\chi_2)|\rho_{f0}^2}. \quad (8)$$

For a pulse with the initial duration $\tau_0 \cong 1$ ps, intensity $\rho_{f0}^2 \cong 10^{10}$ W/cm^2, and carrier frequency $\omega_0 = 10^{15}$ s^{-1} entering the fiber with the parameters $v^{-1} = 6 \times 10^{-13}$ s/m, $\sigma = 4.5$ m^{-1}, $R(\gamma_s + \gamma_c) = 1.5 \times 10^{-14}$ W^{-1} m^{-1}, we obtain $\chi_1 = 3 \times 10^{-29}$ (s m)/W and $\chi_2 = 10^{-27}$ (s m)/W which yields $L_p \cong 5$ m.

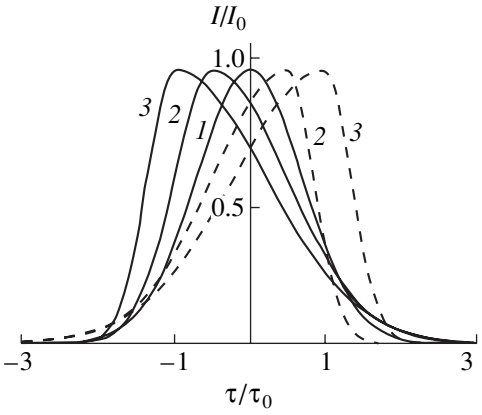

Variation of the shape of a Gaussian pulse propagating in a nonlinear two-mode OWG: $z = 0$ (*1*); 2.5 (*2*); 5 m (*3*). See the text for explanations.

For a graphical analysis revealing the character of the pulse shape variation in a given fiber waveguide, the solution (6) is conveniently presented in an explicit form in terms of $\tau(\rho_f)$:

$$\frac{\tau}{\tau_0} = \frac{\rho_f^2 z}{\tau_0}(3\chi_1 + (-1)^f 2\chi_2) \mp \left(2\ln\frac{\rho_{f0}}{\rho_f}\right)^{1/2}, \quad (9)$$

where the plus and minus signs at the second term refer to the leading and trailing front, respectively. The pattern of shape variation for a pulse propagating in a waveguide with the parameters indicated above is illustrated in the figure for $z = 0$, 2.5, and 5 m (curves *1–3*, respectively) for the cases of antisymmetric (solid curves) and symmetric (dashed curves) fiber excitation. As can be seen, a change in the type of excitation results in the passage of the steepening effect from the trailing to leading front of the pulse. In this wave packet, comprising unidirectional strongly coupled modes, the trailing front steepening is related both to the dispersion of phase self- and cross-modulation and to the mode coupling; the later contribution is determined by the parameter χ_2. The inequality $|\chi_2/\chi_1| \gg 1$, which may be valid in a broad range of pulse and medium parameters, indicates that the propagation length L_p corresponding to the envelope shock wave formation in the fibers under consideration is significantly smaller than the analogous value for single-mode fibers.

An analysis of the values of waveguide and radiation parameters given above together with the corresponding lengths of the envelope shock wave formation demonstrates the necessity of taking the dispersion of nonlinearity into account in the study of nonlinear systems with strong linear mode coupling. This analysis also indicates the real possibility of using such systems for the development of purely optical logic element.

REFERENCES

1. A. A. Maĭer, Usp. Fiz. Nauk **165** (9), 1037 (1995) [Phys. Usp. **38**, 991 (1995)].
2. Y. Chen, J. Opt. Soc. Am. B **8** (5), 986 (1991).
3. F. Kh. Abdullaev and R. Gulyamov, Pis'ma Zh. Tekh. Fiz. **18** (20), 10 (1992) [Sov. Tech. Phys. Lett. **18**, 653 (1992)].
4. S. A. Vasil'ev, E. M. Dianov, A. S. Kurkov, *et al.*, Kvantovaya Élektron. (Moscow) **24** (2), 151 (1997).
5. V. A. Vysloukh and L. P. Gevorkyan, Izv. Akad. Nauk SSSR, Ser. Fiz. **55** (2), 322 (1991).
6. F. Kh. Abdullaev, R. M. Abrarov, V. I. Goncharov, and S. A. Darmanyan, Zh. Tekh. Fiz. **64** (9), 102 (1994) [Tech. Phys. **39**, 916 (1994)].
7. I. O. Zolotovskiĭ and D. I. Sementsov, Opt. Spektrosk. **88** (4), 620 (2000) [Opt. Spectrosc. **88**, 560 (2000)].
8. S. A. Akhmanov, V. A. Vysloukh, and A. S. Chirkin, in *The Optics of Femtosecond Pulses* (Nauka, Moscow, 1988), p. 312.
9. A. N. Oraevskiĭ, Usp. Fiz. Nauk **168** (12), 1311 (1998) [Phys. Usp. **41**, 1199 (1998)].
10. I. O. Zolotovskiĭ and D. I. Sementsov, Opt. Spektrosk. **85** (2), 304 (1998) [Opt. Spectrosc. **85**, 281 (1998)]; Opt. Spektrosk. **86** (5), 786 (1999) [Opt. Spectrosc. **86**, 737 (1999)].

Translated by P. Pozdeev

Technical Physics Letters, Vol. 27, No. 7, 2001, pp. 575–578. Translated from Pis'ma v Zhurnal Tekhnicheskoĭ Fiziki, Vol. 27, No. 14, 2001, pp. 6–15.

The Effect of the Absolute Phase on the Spectrum of a Femtosecond Pulse Propagating in a Nonlinear Medium

D. K. Skripov and V. A. Trofimov

Moscow State University, Moscow, 119899 Russia

e-mail: vatro@cs.msu.su

Received February 2, 2001

Abstract—It is shown that the spectrum of a femtosecond light pulse propagating in a nonlinear medium depends on the absolute phase. As the propagation distance increases, the effect of the absolute phase of the light pulse on its spectrum may either decrease or increase. © *2001 MAIK "Nauka/Interperiodica".*

Following the development of lasers capable of generating radiation pulses with a duration of tens of femtoseconds (or even less), the question has arisen as to how the absolute phase of such a pulse can influence its interaction with the medium. Tempea *et al.* [1] considered the problem of measuring the absolute phase of a visible light pulse with a duration of 10 fs. Korolkov *et al.* [2] showed that the absolute phase of a subpicosecond IR pulse affects the dissociation yield of diatomic molecules. It should be noted that the possible effect of a nonlinear medium response on the pulse propagation was not even mentioned in these papers, where the analysis was performed within the framework of a preset field approximation.

Below we will demonstrate, based on the nonlinear Maxwell equations, that the absolute phase of a light pulse propagating in an optically extended medium affects the spectrum. The effect depends both on the propagation distance and on the duration and amplitude of the radiation pulse. Note that previously [3, 4] we demonstrated that the position of a maximum spectral component of a light pulse depends on its duration.

Let us describe propagation of a light pulse along the z axis within the framework of one-dimensional Maxwell equations written (in terms of dimensionless variables) for the strengths of the electric E and magnetic H field with saturating restoring force

$$\frac{\partial H}{\partial z} = -\frac{\partial D}{\partial t}, \quad \frac{\partial E}{\partial z} = -\frac{\partial H}{\partial t},$$

$$D = E + 4\pi P, \quad -L_i \le z \le L_z, \quad 0 \le t \le L_t,$$

$$\frac{\partial^2 P}{\partial t^2} + \delta\frac{\partial P}{\partial t} + \frac{P}{1+|P|^n} = \alpha E(z,t), \tag{1}$$

$$z > 0, \quad P = 0, \quad z \le 0$$

with the initial and boundary conditions

$$E_{|z=-L_i} = H_{|z=-L_i} = P_{|t=0} = \frac{\partial P}{\partial t}_{|t=0} = 0,$$
$$E_{|t=0} = E_0(z), \quad H_{|t=0} = H_0(z). \tag{2}$$

The initial pulse is set on the interval $[-L_i, 0]$:

$$E(0,z) = E_0(z)$$
$$= \begin{cases} E_0 \exp\left(-\dfrac{(z+0.5L_i)^2}{\tau^2}\right)\cos\left(\omega\left(z+\dfrac{L_i}{2}\right)+\varphi\right), \\ -L_i \le z < 0, \\ 0, \quad 0 \le z \le L_z, \end{cases} \tag{3}$$
$$H(0,z) = E_0(z).$$

In Eqs. (1)–(3), z is the spatial coordinate; L_i, L_z are the lengths of linear and nonlinear media; $L_t = L_i + L_z$ is the domain length with respect to the dimensionless time coordinate t; ω is the "filling" frequency of the incident Gaussian pulse; τ is the pulse duration; δ is a coefficient characterizing polarization damping in the medium; α is a quantity proportional to the dipole moment of an atom or molecule; and φ is the absolute phase of the light pulse, which characterizes asymmetry of the pulse filling relative to the center of the its envelope.

By selecting the initial magnetic field distribution equal to the electric field, we ensure that the electromagnetic wave propagates in vacuum only in the positive direction of the z axis. The cross section $z = 0$ corresponds to an interface between linear and nonlinear media; accordingly, we set $P = 0$ for $z \le 0$.

Note that the term "linear medium" implies a medium with the corresponding instantaneous response, while the nonstationary response processes are ignored. This is the main condition used in writing the equation for polarization in the region of z up to $z = 0$. Another condition

1063-7850/01/2707-0575$21.00

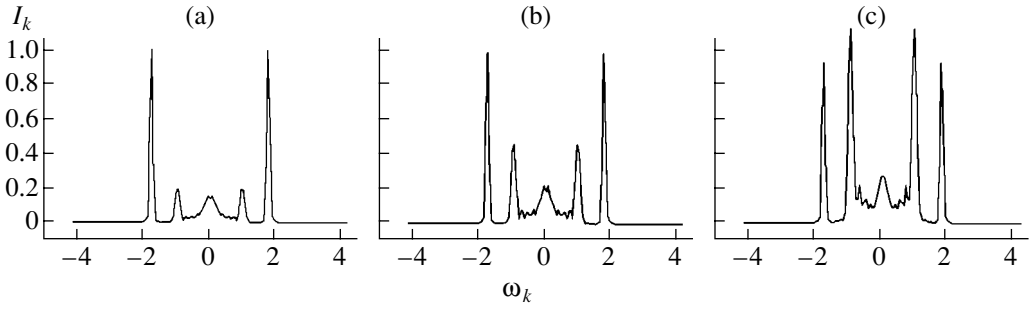

Fig. 1. Effect of the absolute phase φ of an incident light pulse on the output pulse spectrum $I_k = \left|D_{\omega_k}\right|^2$ at the exit from an optically thin medium. The model calculation was performed for τ = 15; ω = 1.8; E_0 = 22; α = 0.3; δ = 10^{-4}; L_t = 100; and φ = −0.02π (a), 0 (b), 0.02π (c). The spectral frequency was calculated by the formula $\omega_k = \frac{2\pi}{L_t} k$, $k = 0, \pm1, \pm2, \ldots$.

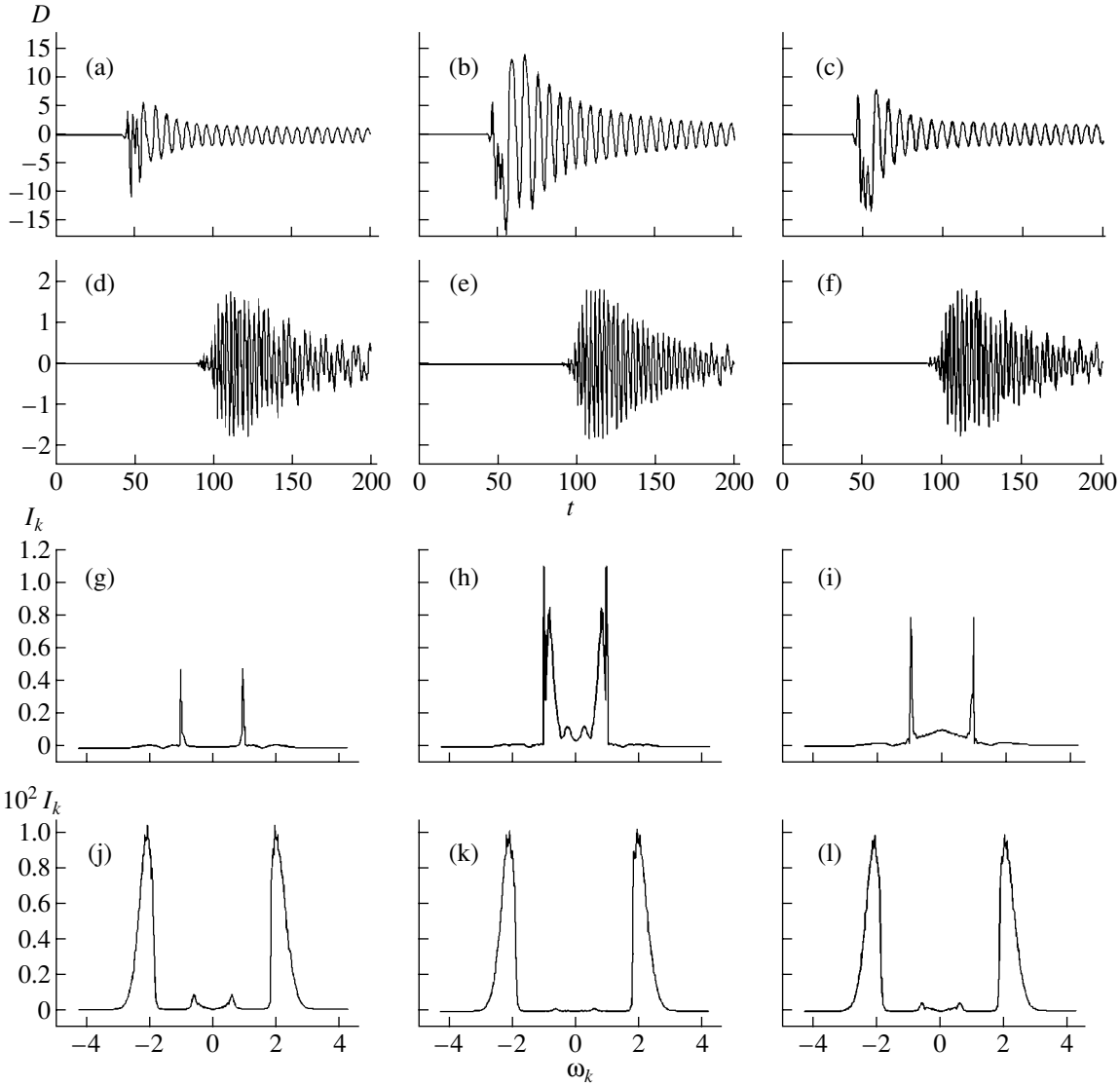

Fig. 2. Evolution of (a–f) the electric induction $D(z, t)$ and (g–l) its spectral composition $I_k = |D_{\omega_k}(z)|^2$ in the cross sections near (a–c, g–i) $z \sim 0$ and (d–f, j–l) $z = 40$ depending on the absolute phase of the incident pulse $\varphi = -\frac{\pi}{4}$ (a, d, g, j); 0 (b, e, h, k); $\frac{\pi}{4}$ (c, f, i, l). The model calculation was performed for α = 0.16; ω = 1.8; δ = 0.001; E_0 = 18; L_i = 100; L_z = 100; and τ = 3. The spectral frequency was calculated by the formula $\omega_k = \frac{2\pi}{L_i} k$, $k = 0, \pm1, \pm2, \ldots$.

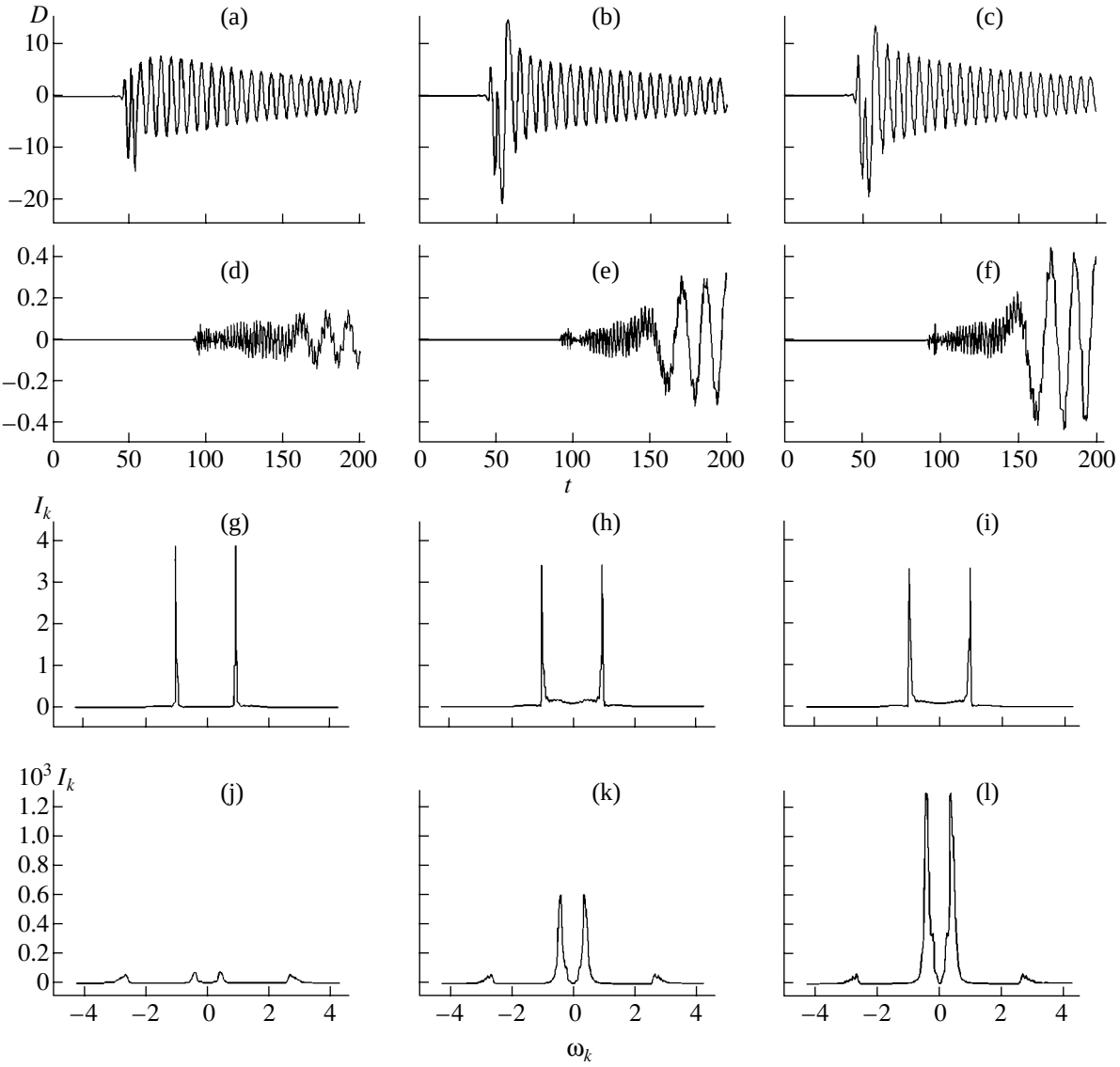

Fig. 3. Evolution of (a–f) the electric induction $D(z, t)$ and (g–l) its spectral composition $I_k = |D_{\omega_k}(z)|^2 (g - l)$ in the cross sections near (a–c, g–i) $z \sim 0$ and (d–f, j–l) $z = 40$ depending on the absolute phase of the incident pulse $\varphi = -\frac{\pi}{4}$ (a, d, g, j); 0 (b, e, h, k); $\frac{\pi}{4}$ (c, f, i, l). The model calculation was performed for $\alpha = 0.4$; $\omega = 1.8$; $\delta = 0.001$; $E_0 = 10$; $L_i = 100$; $L_z = 100$; and $\tau = 3$. The spectral frequency was calculated by the formula $\omega_k = \frac{2\pi}{L_i} k$, $k = 0, \pm 1, \pm 2, \ldots$.

($P = 0$) does not restrict the generality of the analysis, since a relationship between polarization and electric field strength in the form $P = \alpha E$ (in the above dimensionless equations) only means a change in velocity of the electromagnetic wave propagation. An appropriate renormalization of the variables allows the Maxwell equations to be written in the form of (1) with $P = 0$.

In terms of the variables employed, the linear oscillator frequency is unity. The parameter n will be taken equal to 4, which corresponds to the case of a field interacting with a dipole [5]. It should be emphasized that a description of the interaction between laser radiation and a molecule in [2] employed a dipole moment representation in the form of $r\exp(-r/r_0)$, which also implies saturation of the interaction upon strong deformation of the molecule. Below we will consider the action of fields not leading to the ionization of an atom (the calculations were performed to check for the validity of the condition $|P| < 10$).

Optically thin layer. The results of computer modeling showed that an optically thin layer is characterized by a strong dependence of the medium response to

the absolute phase φ of the incident pulse. In this case, all processes in any cross sections exhibit the same character. Accordingly, we have to solve a single equation for polarization at a preset electric field pulse $E = E(t)$:

$$\frac{d^2P}{dt^2} + \delta\frac{dP}{dt} + \frac{P}{1+|P|^n} = \alpha E(t),$$

$$E(t) = E_0\cos(\omega t + \varphi)\exp\left(-\frac{(t-0.5L_t)^2}{\tau^2}\right), \quad (4)$$

$$0 \le t \le L_t.$$

In order to compare the results obtained for thin and thick layers, we retain the parameters α and E_0 in Eq. (4).

An example is represented in Fig.1, from which it follows that an absolute phase increment as small as 0.01 of the period changes the spectral composition of even a relatively large pulse ($\tau = 15$), whereby the energy is redistributed between frequencies.

Optically extended medium. In an optically thick medium, the spectrum of a pulse may exhibit a significantly weaker dependence on the absolute phase. For example, Figs. 2 and 3 show evolution of the electric induction and its spectral composition for two cross sections (near $z \sim 0$ and at $z = 40$) in the case of a strong light reflection from the interface (about 40 and 95% of the incident light energy reflected in Figs. 2 and 3, respectively).

As can be seen in Fig. 2 for a medium with moderate nonlinearity (less that 40% of the incident light energy is reflected), a maximum effect of the absolute phase of the light pulse is observed at the interface, where the spectral composition exhibits a qualitative variation depending on φ. Since the incident pulse is rather short, the response frequency in the beginning of the nonlinear medium is close to the intrinsic frequency [4]. As the pulse propagates further, the spectrum is enriched with high-frequency harmonics and the absolute phase effect is manifested only in the region of low-frequency spectral components.

In the case of a strong excitation of the medium (see Fig. 3 where more than 80% of the incident energy is reflected), the absolute phase influence on the pulse spectrum grows with increasing propagation distance. As a result, the light pulse splits into subpulses.

Note also that the interaction of a light pulse with a medium in which less than 10% of the incident energy is reflected (weak interaction), a change in the absolute phase of the initial pulse virtually does not influence the pulse envelope variation in the medium.

Thus, an analysis of the results of our model calculations lead to the following conclusions. The possible effect of the initial absolute phase on the pulse spectrum depends significantly on the light–medium interaction parameters. For a moderate excitation of the medium, the absolute phase effect is most pronounced at the entrance cross section. Penetrating deep into the medium, the pulse "forgets" the initial phase. In a medium featuring strong excitation, the dependence of the pulse spectrum composition on the absolute phase increases with the propagation distance. Here, a situation is possible when the absolute phase effect is manifested deep in the medium, on the final propagation segment.

Acknowledgments. This study was supported by the Russian Foundation for Basic Research (project no. 99-01-01233) and "Russian Universities. Fundamental Research" Program (project no. 99-01-01233).

REFERENCES

1. G. Tempea, A. Roppe, A. Mueller, *et al.*, in *Technical Program of the International Conference LO'10, St. Petersburg, 2000*, p. 40.
2. M. V. Korolkov, Y. Manz, and G. K. Paramonov, Chem. Phys. **217**, 341 (1997).
3. D. K. Skripov and V. A. Trofimov, Proc. SPIE **4002**, 34 (2000).
4. D. K. Skripov and V. A. Trofimov, in *Fiber-Optic Technologies, Materials and Devices: Collection of Works of the Educational and Scientific Center of Fiber-Optic Materials and Devices* (UNTs Volokonno-Optich. Mater. i Ustroĭstv, Moscow, 2000), No. 3, pp. 83–92.
5. S. M. Gladkov and N. I. Koroteev, Usp. Fiz. Nauk **160** (7), 105 (1990) [Sov. Phys. Usp. **33**, 554 (1990)].

Translated by P. Pozdeev

Technical Physics Letters, Vol. 27, No. 7, 2001, pp. 579–580. Translated from Pis'ma v Zhurnal Tekhnicheskoĭ Fiziki, Vol. 27, No. 14, 2001, pp. 16–20.

A Model of Weakly Nonlinear Stages for the Periodic Structure Formation on the Charged Surface of a Conducting Liquid

N. M. Zubarev and O. V. Zubareva

Institute of Electrophysics, Ural Division, Russian Academy of Sciences, Yekaterinburg, Russia

e-mail: nick@ami.uran.ru

Received February 2, 2001

Abstract—Effects of the four-wave processes on the dynamics of the charged boundary of a conducting liquid are compared for the cases of plane and square symmetry of the problem. Considering a slit liquid-metal electrode, whose special feature is a possible degeneration of the nonlinear three-wave interaction, we propose a model of the initial stage in the formation of a periodic system of cusps on its surface. © *2001 MAIK "Nauka/Interperiodica".*

As is well known [1], the surface of a conducting liquid exposed to a sufficiently strong electric field is unstable. Interaction of the field with the induced surface charges leads to the formation of a single cone-shaped cusp or a system of such cusps. The field enhancement at the cusp apex gives rise to intense emission processes, which accounts for a wide practical use of liquid-metal emitters as the sources of charged particles. The pattern of instability development on a conducting liquid surface is determined by two principal factors: the general laws of electrohydrodynamic processes and the system geometry.

Let us consider a liquid-metal electrode of the elongated slit type, in which the liquid surface is infinite in one direction (along the slit corresponding to the y axis) and finite in the perpendicular direction (x axis). Conditions on the slit boundaries (in particular, the wetting conditions) determine the initial system configuration possessing a plane symmetry. Upon the external electric field application, this configuration is no longer in equilibrium and instabilities can develop in the x direction. However, a plane symmetry of the surface perturbations is broken as well [2] and a chain of equidistant emitting cusps is formed in the y direction. The characteristic size of the system is determined by the most rapid spatial harmonic. If the electric field strength E is close to a threshold value for the instability development $E_c = (64\pi^2 g\alpha\rho)^{1/4}$ (where g is the acceleration of gravity, α is the coefficient of surface tension, and ρ is the density of the medium), the system features increasing perturbations along the y axis with the wavenumbers close to $k_0 = \sqrt{g\rho/\alpha}$ [1].

Thus, the system exhibits a tendency to develop perturbations with wavevectors in two orthogonal directions (along the x and y axes). Now we will demonstrate that, in the case of a small critical parameter $\varepsilon = (E^2 - E_c^2)/E_c^2$ ($\varepsilon \ll 1$), the nonlinear interaction of perturbations leads to the explosion-like growth of the surface perturbations and the formation of a periodic system of cusps.

Consider a potential motion of the ideal conducting liquid possessing infinite depth in an external electric field. Let the field vector be directed along the z axis of our coordinate system. The electric field potential φ and the velocity potential Φ (for the incompressible liquid) obey the Laplace equations

$$\nabla^2\varphi = 0, \quad \nabla^2\Phi = 0, \tag{1}$$

that have to be solved jointly with the conditions

$$\Phi_t + \frac{(\nabla\Phi)^2}{2} = \frac{(\nabla\varphi)^2 - E^2}{8\pi\rho} + \frac{\alpha}{\rho}\nabla_\perp\frac{\nabla_\perp\eta}{\sqrt{1+(\nabla_\perp\eta)^2}} - g\eta,$$

$$z = \eta, \tag{2}$$

$$\eta_t = \Phi_z - \nabla_\perp\eta\nabla_\perp\Phi, \quad z = \eta, \tag{3}$$

$$\varphi = 0, \quad z = \eta, \tag{4}$$

$$\Phi \longrightarrow 0, \quad z \longrightarrow -\infty, \tag{5}$$

$$\varphi \longrightarrow -Ez, \quad z \longrightarrow \infty, \tag{6}$$

where $\eta(x, y, t)$ is a function determining the liquid surface shape. Relationship (2) is a nonstationary Bernoulli equation taking into account the field of gravity and the electrostatic and capillary pressures; Eq. (3) expresses the condition of the boundary when impenetrable for liquid; relationship (4) is the condition of the liquid surface when equipotential; condition (5) shows that the liquid motions decay at an infinite depth; and condition (6) expresses the field homogeneity at an infinite distance from the surface.

1063-7850/01/2707-0579$21.00

For simplicity, we will assume that the slit width is $2\pi/k_0$ and the conditions on the slit boundaries are periodic. In this system, only the perturbation modes can develop for which the wavevector projections on the x axis are multiples of k_0. For small values of the critical parameter, this implies that only harmonics with the wavevectors $\mathbf{k}_1 = \{k_0, 0\}$ and $\mathbf{k}_2 = \{0, k_0\}$ will be unstable, which corresponds to a square lattice symmetry. Note that on the infinite plane liquid surface all modes with $|\mathbf{k}| = k_0$ are unstable and the nonlinear three-wave interactions between waves with the wavevectors rotated by $2\pi/3$ relative to each other lead to the development of surface perturbations possessing a hexagonal symmetry [3]. A special feature of the problem under consideration is that the three-wave processes are degenerated and the character of the electrohydrodynamic instability development in the weakly nonlinear stage is determined by the four-wave interactions.

The state of the system is uniquely determined by the functions $\eta(\mathbf{r}, t)$ and $\psi(\mathbf{r}, t) = \Phi|_{z=\eta}$ [4]. Let us represent perturbations of the surface shape η as

$$\eta(\mathbf{r}, t) = A_1(t)e^{i\mathbf{k}_1\mathbf{r}} + A_2(t)e^{i\mathbf{k}_2\mathbf{r}} + A_1'(t)e^{2i\mathbf{k}_1\mathbf{r}} + A_2'(t)e^{2i\mathbf{k}_2\mathbf{r}} + A_1''(t)e^{i(\mathbf{k}_1+\mathbf{k}_2)\mathbf{r}} + A_2''(t)e^{i(\mathbf{k}_1-\mathbf{k}_2)\mathbf{r}} + \text{c.c.},$$

and those of the velocity potential ψ at the liquid boundary as

$$\psi(\mathbf{r}, t) = B_1(t)e^{i\mathbf{k}_1\mathbf{r}} + B_2(t)e^{i\mathbf{k}_2\mathbf{r}} + B_1'(t)e^{2i\mathbf{k}_1\mathbf{r}} + B_2'(t)e^{2i\mathbf{k}_2\mathbf{r}} + B_1''(t)e^{i(\mathbf{k}_1+\mathbf{k}_2)\mathbf{r}} + B_2''(t)e^{i(\mathbf{k}_1-\mathbf{k}_2)\mathbf{r}} + \text{c.c.},$$

where the nonlinear interactions of the dominant spatial harmonics k_0 with the second harmonics $2k_0$ and with the combination harmonics $\sqrt{2}\,k_0$ are taken into account.

Substituting these expressions into the initial equations and taking into account the smallness of the ε value, we obtain amplitudes of the $2k_0$ and $\sqrt{2}\,k_0$ harmonics as functions of the order parameters A_1 and A_2:

$$k_0 B_j = A_{jt}, \quad 2k_0 B_j' = A_{jt}', \quad \sqrt{2}k_0 B_j'' = A_{jt}'',$$

$$A_j' = 2k_0 A_j^2, \quad A_1'' = k_0 \alpha A_1 A_2, \quad A_2'' = k_0 \alpha A_1 A_2^*,$$

where $j = 1, 2$ and $\alpha = 8\sqrt{2} + 10$. In this case, the liquid surface dynamics is determined by the following amplitude equations

$$A_{1tt} = \varepsilon A_1 + sA_1|A_1|^2 + \sigma A_1|A_2|^2, \tag{7}$$

$$A_{2tt} = \varepsilon A_2 + sA_2|A_2|^2 + \sigma A_2|A_1|^2. \tag{8}$$

Here, we passed to dimensionless variables by substituting $A_j \longrightarrow A_j/k_0$, $t \longrightarrow t/\sqrt{2gk_0}$ and introduced the notation $s = 11/4$, $\sigma = 32\sqrt{2} + 65/2$. These amplitude equations were derived with an allowance for the quadratic and cubic nonlinearities in the equations of motion (1)–(6).

A remarkable feature is that the coefficient σ at the cross terms in Eqs. (7) and (8) exceeds the coefficient s at the homogeneous terms ($\sigma/s \approx 28.3$) by more than one order of magnitude. This implies that the contribution due to nonlinear interactions $\mathbf{k}_1 \longleftrightarrow \mathbf{k}_1$ and $\mathbf{k}_2 \longleftrightarrow \mathbf{k}_2$ responsible for the development of one-dimensional structures is negligibly small as compared to the contribution of $\mathbf{k}_1 \longleftrightarrow \mathbf{k}_2$ interactions. As a result, the square structure of surface perturbations in the nonlinear stage of instability development is more favorable than the one-dimensional structure corresponding to the condition $A_1 = 0$ or $A_2 = 0$.

As can be seen from Eqs. (7) and (8), the presence of four-wave processes imparts an explosion-like character to the temporal evolution of the amplitudes A_1 and A_2, which grow infinitely over a finite time with certain asymptotics:

$$|A_1| \longrightarrow |A_2| \longrightarrow \frac{\sqrt{2}}{\sqrt{s+\sigma}(t_c - t)}, \quad t \longrightarrow t_c,$$

where t_c corresponds to the moment of explosion. Thus, even the simplest model described by Eqs. (7) and (8), where the nonlinearity is taken into account only in the first nonvanishing order, reveals a tendency to develop singularities in solutions of the electrohydrodynamic equations.

We have constructed a model describing the development of electrohydrodynamic instabilities of the charged surface of a liquid metal in a slit emitter. According to this model, a nonlinear interaction between the surface waves parallel and perpendicular to the slit gives rise to an explosion-like development of a periodic system of surface perturbations, which subsequently grow to form a chain of equidistant emitting cusps observed in experiment [2].

Acknowledgments. The authors are grateful to V.G. Suvorov for kindly indicating the relevant publication [2] and to N.B. Volkov for his interest in this study.

The study was supported by the Russian Foundation for Basic Research (project no. 00-02-17428) and by the INTAS Foundation (grant no. 99-1068).

REFERENCES

1. Ya. I. Frenkel', Zh. Éksp. Teor. Fiz. **6** (4), 350 (1936).
2. J. Mitterauer, Appl. Surf. Sci. **87**/**88**, 79 (1995).
3. N. M. Zubarev and O. V. Zubareva, Phys. Lett. A **272**, 119 (2000).
4. V. E. Zakharov, Prikl. Mekh. Tekh. Fiz. **2**, 86 (1968).

Translated by P. Pozdeev

Technical Physics Letters, Vol. 27, No. 7, 2001, pp. 581–582. Translated from Pis'ma v Zhurnal Tekhnicheskoĭ Fiziki, Vol. 27, No. 14, 2001, pp. 21–24.

A Bolometric Detector Built into the Diamond Bulk

A. Yu. Klokov, A. I. Sharkov*, T. I. Galkina, R. A. Khmel'nitskii, V. A. Dravin, and A. A. Gippius

Lebedev Physical Institute, Russian Academy of Sciences, Moscow, 117924 Russia

** e-mail: shark@sci.lebedev.ru*

Received January 23, 2001

Abstract—Since diamond can be used as both the substrate and the active medium in electronic devices, it is very important to obtain information concerning the temperature variations in the immediate vicinity of active elements and the conditions of heat removal from such elements. This task is solved by a bolometer built into a diamond plate, which is capable of measuring temperature increments induced by laser pulses in the diamond or in the diamond-supported surface structures. The bolometer, representing a buried graphitized layer formed by helium ion implantation with subsequent annealing, has a characteristic response time of ~10 ns. © *2001 MAIK "Nauka/Interperiodica".*

As is well known, the prospects of using diamonds in electronics are determined by the unique thermal properties of this crystal: the room temperature thermal conductivity of diamond exceeds that of copper. Using diamond substrates in transistors, lasers, etc., allows a severalfold increase in the device threshold characteristics, while the thermal stability of diamond-based lasers increases by several orders of magnitude [1].

The degree of overheating in diamond-based devices pumped by laser pulses or in pulsed micro- and optoelectronic structures on diamond substrates are frequently measured by thermocouples possessing a significant response time (reaching fractions of a second) [2]. Moreover, thermometers of any type are usually glued to a sample, this contact introducing unavoidable error into the results of temperature measurements. Apparently, a temperature sensor built into the material lattice would minimize all these disadvantages.

We have previously designed and manufactured a phonon generator for diamond, based on a buried (implanted) graphitized layer [3]. It was demonstrated that such a photosensitive layer allows a good acoustic matching with the diamond matrix lattice. Being conductive ($\rho \sim 10^{-2}$ Ω cm), this layer can be used as a

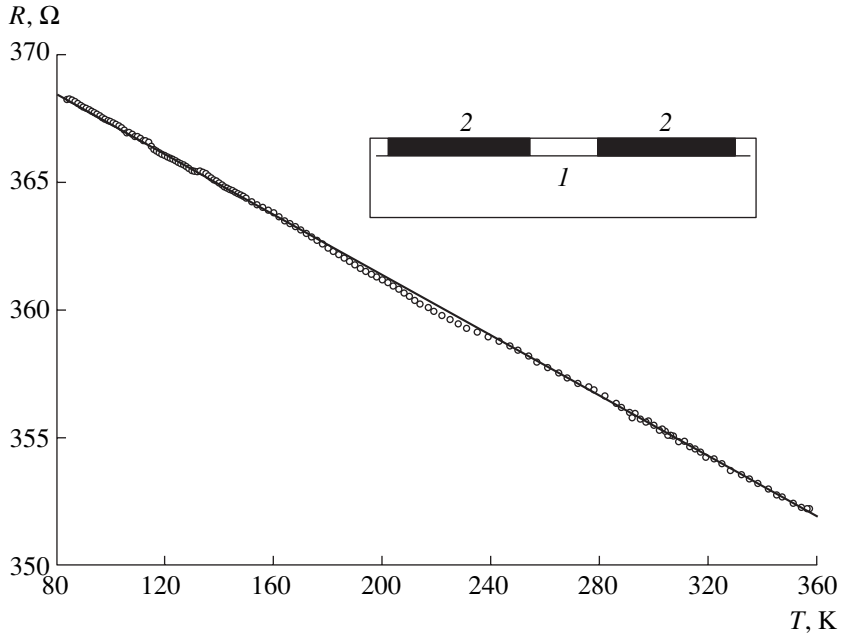

Fig. 1. An experimental plot of the bolometer resistance R versus temperature T (open circles); solid line shows a linear approximation. The inset shows a schematic diagram of the bolometric structure with (*1*) buried graphitized layer and (*2*) graphite contact channels.

1063-7850/01/2707-0581$21.00 © 2001 MAIK "Nauka/Interperiodica"

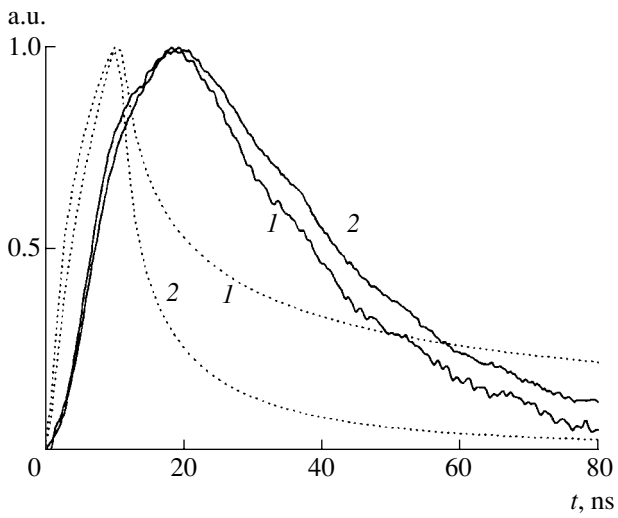

Fig. 2. The normalized experimental photoresponse of a bolometric structure irradiated with nitrogen laser pulses (λ = 337 nm; τ = 7.5 ns) at temperatures T = 300 (*1*) and 90 K (*2*); solid curves *1* and *2* show the corresponding normalized kinetics of the average bolometer overheating calculated for the same temperatures.

phonon detector (bolometer) possessing very short response time.

The built-in bolometer was prepared as follows. A single crystal plate of natural diamond (type IIa) was implanted with 350-keV He^+ ions to a dose of 4×10^{16} cm^{-2} and annealed for 1 h at 1400°C. As a result, a graphitized layer *1* (see the inset in Fig. 1) with a thickness of ~150 nm was formed at a depth of ~700 nm in the crystal. The contacts to this buried layer were provided by graphite columns *2* formed by helium implantation in an energy-distributed dose regime [2]. Gold conductors with a diameter of 30 μm were glued to these columns with a silver-based epoxy composition (EMS 12640) and used for the four-point-probe electrical measurements. This bolometric structure had a detector area of 70×70 μm.

Figure 1 (open circles) shows a plot of the bolometer resistance R versus temperature T measured in the range from 80 to 360 K. The room-temperature resistance was 356 Ω at a current of 2 mA. As can be seen from Fig. 1, the $R(T)$ plot is linear in the entire temperature range studied and the temperature coefficient of resistance is –0.06 Ω/K.

The bolometer response to irradiation with pulses of a nitrogen laser (LGI-21, wavelength λ = 337 nm, pulse duration τ = 7.5 ns) was amplified by a broadband low-noise preamplifier with a high input impedance (100 kΩ) and registered using a system based on a stroboscopic voltage converter of the V9-5 type. Figure 2 presents the normalized experimental photoresponse of this structure for two temperatures, T = 300 and 90 K (solid curves *1* and *2*, respectively). As can be seen, the response pulse decay duration at half height is $\Delta\tau_{1/2}$ = 10–12 ns. Note also that the response pulse shape remained unchanged in the range of laser pulse energies from 0.1 to 1 μJ.

The experimental data were analyzed by comparing them with the results of model calculation of the dynamics of temperature variation in a diamond/graphite/diamond layer structure. The calculation was based on the solution of a system of three three-dimensional linear equations of thermal conductivity describing the temperature distribution in each layer.

Dotted curves in Fig. 2 show the normalized curves of the average overheating kinetics of the buried graphite calculated for the conditions close to experimental. Since the actual structure of a buried graphitized layer is insufficiently clear, the thermal parameters of this layer were taken equal to the reference values for graphite.

As is seen, the calculated curves are significantly narrower than the experimental plots. However, the integration constant of an input circuit in the experimental setup was τ ~10 ns ($\tau = R_{bol}C_{in}$ = 360 Ω × 30 pF). Thus, the experimental bolometer response time ~12 ns estimated as the pulse decay duration is virtually the instrumental response time; this value should be considered as an estimate from above for the true bolometer response time.

Acknowledgments. This study was supported by the Russian Foundation for Basic Research, project no. 98-02-16892.

REFERENCES

1. V. B. Kvaskov, in *Russia's Natural Diamonds*, Ed. by V. B. Kvaskov (Polyaron, Moscow, 1997), pp. 148–194.
2. A. A. Gippius, R. A. Khmelnitsky, V. A. Dravin, *et al.*, Diamond Relat. Mater. **8**, 1631 (1999).
3. T. I. Galkina, A. I. Sharkov, A. Yu. Klokov, *et al.*, Pis'ma Zh. Éksp. Teor. Fiz. **64** (4), 270 (1996) [JETP Lett. **64**, 298 (1996)].

Translated by P. Pozdeev

Technical Physics Letters, Vol. 27, No. 7, 2001, pp. 583–585. Translated from Pis'ma v Zhurnal Tekhnicheskoĭ Fiziki, Vol. 27, No. 14, 2001, pp. 25–29.

A Hybrid Microwave Generator Based on a Vircator–TWT (Virtode) System

V. D. Selemir, A. E. Dubinov, E. E. Dubinov, I. V. Konovalov, and A. V. Tikhonov

Institute of Experimental Physics, Russian Federal Nuclear Center, Sarov, Russia

Received November 13, 2000; in final form, February 2, 2001

Abstract—Various schemes of microwave generators (TWT, vircator, and a vircator–TWT hybrid virtode) were studied in operation under the same power supply conditions. It is demonstrated that the virtode offers the most efficient solution. *© 2001 MAIK "Nauka/Interperiodica".*

As is well known, an oscillating virtual cathode modulates the electron beam transit current [1]. This circumstance allows the electron beams with virtual cathodes to be used both in microwave generators [2, 3] and in collective ion accelerators [4]. The microwave generators employing virtual cathodes (called vircators) are among the most promising devices of relativistic electronics.

An interesting approach to the development of vircators consists in creating a hybrid generator [5] in which the electron transit current modulated by a virtual cathode is fed into a retarding system operating in the backward-wave tube (BWT) mode. An SHF wave excited in BWT returns back to the virtual cathode region (thus allowing a feedback) where the microwave radiation can be extracted from the device. This generator, representing a vircator–BWT hybrid system, is called virtode.

In this study, we have designed and constructed a hybrid microwave generator of the virtode type based on the combination of a vircator and a traveling-wave tube (TWT). The virtode system consists in the idea that a modulated electron beam is fed into a TWT retarding system. As a result, the retarding system (in comparison to that in a usual TWT) is pumped with this electron beam and a microwave radiation of the vircator representing a high-Q resonator.

The virtode was supplied from a two-stage linear induction accelerator (linac) of the I-3000 type described elsewhere [6]. The pulsed electron beam parameters used in our experiments were as follows: electron energy, 2.4 MeV; beam current, 12 kA; pulse duration 20 ns.

The electrodynamic TWT system structure comprised an open cavity representing a section of ridged round waveguide with an external diameter of 67 mm, a corrugation period and profile depth of 16 and 7 mm, respectively, and the number of periods equaled 18. The corrugation profile shape represented matched semicircles. The electrodynamic system was placed inside a solenoid generating a magnetic field of up to 3 kOe.

A relativistic TWT configuration depicted in Fig. 1a is analogous to that studied previously [6]. Optimized with respect to the system geometry parameters, diode impedance, and magnetic field configuration, the TWT-based microwave generator operated at 10 GHz with a 10% efficiency [6]. The results of measurements of the spatial and temporal far-zone structure of the extracted radiation showed evidence of a narrowband and coherent character of the microwave emission. In this study, the optimum TWT configuration was used as a reference system.

Figure 1b shows a vircator configuration based on a smooth drift tube with an internal diameter coinciding with that of the corrugated TWT waveguide structure. The diode part of the vircator was separated from the drift tube by a metal grid with a geometric transparency of 90% (made of 0.1-mm-diameter tantalum wire); the cathode–grid spacing was 60 mm. This vircator system was also used for the comparison.

Figure 1c presents the geometry of a virtode based on a vircator–TWT hybrid system. It should be emphasized that both the TWT and vircator, as well as the virtode, were designed so as to operate in the microwave generation regime: in contrast to the microwave amplification mode, no external microwave signals were applied to the input of these devices. This circumstance justifies the comparison of the output radiation power of the microwave generators studied.

Figure 1d shows a magnetic field strength profile in the configurations studied. In addition, we also studied a smooth waveguide configuration without a grid (in contrast to the vircator). All the aforementioned systems were tested using identical high-voltage linac supply regimes and the same magnetic field configuration. The output microwave emission power level in the far zone (~10 m) was measured with the aid of hot-carrier germanium detectors mounted in 23×10 mm waveguides.

Typical normalized oscillograms of the microwave pulse envelopes are presented in Fig. 1 on the right of each configuration diagram. For comparison, all values

1063-7850/01/2707-0583$21.00 © 2001 MAIK "Nauka/Interperiodica"

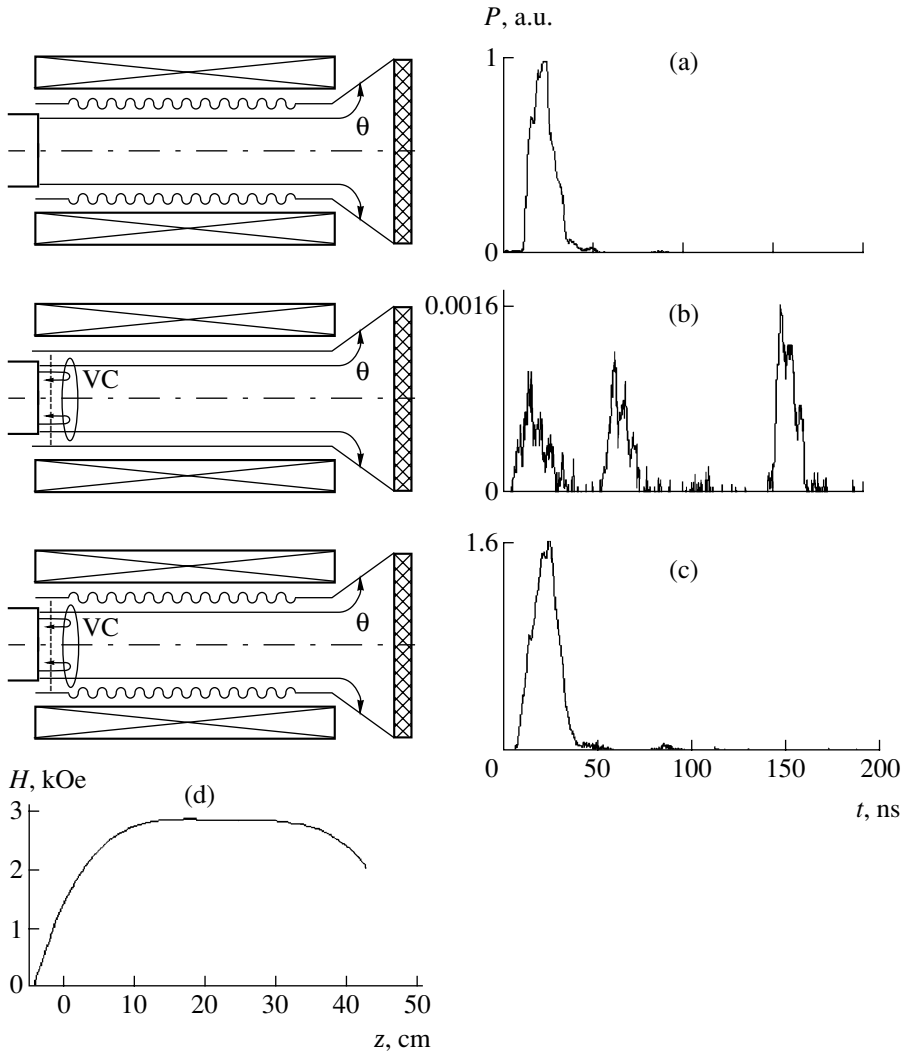

Fig. 1. Schematic diagrams of the microwave generators studied (left) and normalized oscillograms of the output microwave pulse envelopes (right): (a) TWT; (b) vircator; (c) virtode; (d) axial magnetic field strength profile matched to the waveguide configurations; VC—virtual cathode.

were normalized to the TWT peak power density (taken to be unity). As can be seen, the vircator emission power is markedly lower as compared to that of TWT; at the same time, the virtode power markedly exceeds the total power of both the TWT and vircator. The smooth waveguide gridless configuration exhibited no microwave emission at all. Thus, the virtode is the most effective microwave generator among the systems studied.

It should be noted that the vircator produces three sequential microwave pulses, the third carrying a maximum power. The formation of several pulses is explained by the fact that, in a regime of unmatched load, linacs employing the lines with distributed parameters generate a sequence of decaying high-voltage echo pulses. Such a multipulse operation regime was previously also observed in a relativistic TWT system with an I-3000 linac [6]. The maximum power observed for the third vircator pulse is consistent with the fact that a vircator-based generator operates most effectively at a supply voltage of 100–500 kV, the efficiency dropping sharply in the range of ultrarelativistic electron energies. Note that this circumstance is not manifested in the virtode generator where a virtual cathode operates only as a beam modulator.

Thus, a TWT with an anode grid analogous to that described in [6] exhibits an increase in the microwave generation efficiency up to 16%, which is explained by the system operating in a virtode mode. It should be noted that the grid arbitrarily positioned in the TWT does not always allow an increase in the operation efficiency. The grid position has to be adjusted so as to ensure that (i) the virtual cathode will form in the drift tube and (ii) the virtual cathode oscillation frequency will be equal to the intrinsic TWT frequency.

REFERENCES

1. V. I. Kurilko and Ya. B. Faĭnberg, Pis'ma Zh. Tekh. Fiz. **2** (9), 397 (1976) [Sov. Tech. Phys. Lett. **2**, 154 (1976)].
2. V. D. Selemir, B. V. Alekhin, V. E. Vatrunin, *et al.*, Fiz. Plazmy **20** (7-8), 689 (1994) [Plasma Phys. Rep. **20**, 621 (1994)].
3. A. E. Dubinov and V. D. Selemir, Zarubezhn. Radioélektron., No. 4, 54 (1995).
4. V. A. Balakirev, A. M. Gorban', I. I. Magda, *et al.*, Fiz. Plazmy **23** (4), 350 (1997) [Plasma Phys. Rep. **23**, 323 (1997)].
5. N. P. Gadetskiĭ, I. I. Magda, S. I. Naĭsteter, *et al.*, Fiz. Plazmy **19** (4), 530 (1993) [Plasma Phys. Rep. **19**, 273 (1993)].
6. A. I. Pavlovskiĭ, V. S. Bosamykin, V. D. Selemir, V. S. Gordeev, A. E. Dubinov, V. V. Ivanov, A. P. Klement'ev, V. G. Kornilov, V. E. Vatrunin, V. S. Zhdanov, I. V. Konovalov, I. G. Prikhod'ko, V. G. Suvorov, and K. V. Shibalko, in *Relativistic High-Frequency Electronics: Collection of Scientific Works* (Inst. Prikl. Fiz. Akad. Nauk, Nizhni Novgorod, 1992), Vol. 7, p. 81.

Translated by P. Pozdeev

Technical Physics Letters, Vol. 27, No. 7, 2001, pp. 586–588. Translated from Pis'ma v Zhurnal Tekhnicheskoĭ Fiziki, Vol. 27, No. 14, 2001, pp. 30–35.

Solid-State Reactions in TiB_x–GaAs Contact Structures upon Rapid Thermal Annealing

V. V. Milenin and R. V. Konakova

Institute of Semiconductor Physics, National Academy of Sciences of Ukraine, Kiev, Ukraine

Received February 13, 2001

Abstract—Solid-state phase reactions in the initial and vacuum-annealed (T = 500°C, 1 h) TiB_x–GaAs junctions were studied. Thermal treatment of the samples leads to changes in a transition layer structure, with the formation of $B_xGa_{1-x}As$ and $Ti_xGa_{1-x}As$ ternary phases. A physical mechanism explaining these structural transformations is proposed. © *2001 MAIK "Nauka/Interperiodica".*

The increasing level of requirements for the stability of metal–GaAs contacts in devices operating under high-temperature conditions is stimulating a search for new materials that can be used for creating barrier layers. A monoelement metallization cannot solve this task, since almost all metals react with GaAs substrates on heating [1]. The reaction products, formed at the metal–GaAs interface under conditions of deviation from the thermodynamic equilibrium of the contact structure, typically represent two- and three-component phases which are usually unstable. The subsequent conversion or decomposition of these phases lead to the deterioration of the contact parameters.

A promising way to increase the thermal stability of metal-semiconductor contacts consists in using barrier layers of metal compounds, the structure of which can be controlled within broad limits. Such barrier materials include TiB_x films, which combine high chemical and thermal stability with a conductivity approaching that of pure metals. This study was devoted to assessing the possibility of using TiB_x films as barrier layers in metallization contacts for GaAs-based microwave devices.

The experiments were performed with TiB_x–n-n^+-GaAs structures, in which TiB_x layers with a thickness of ~500 Å were obtained by magnetron sputtering of a pressed powder target [2]. The dopant concentration in the n-GaAs film was 10^{16} cm^{-3}; the n-GaAs layer thickness was ~5 μm. The dopant concentration in the n^+-GaAs substrate did not exceed 2×10^{18} cm^{-3}; the substrate thickness was ~300 μm. The sample structures were annealed at T = 500°C for 1 h at a residual pressure of ~10^{-6} torr.

The products of interphase reactions in the contact were studied by Auger electron spectroscopy (AES) and secondary-ion mass spectrometry (SIMS). Before and after thermal treatment, the samples were characterized by measuring their current–voltage characteristics.

Figure 1 shows the elemental depth profiles of the TiB_x–GaAs contact determined before and after annealing (T = 500°C, t = 1 h) by AES in combination with layer removal by ion sputtering. As can be seen from these data, the deposited boride layer has a composition close to TiB_2 and contains a sufficiently small amount of oxygen. Previously [2, 3], we have studied the degradation processes in contacts based on quasi-amor-

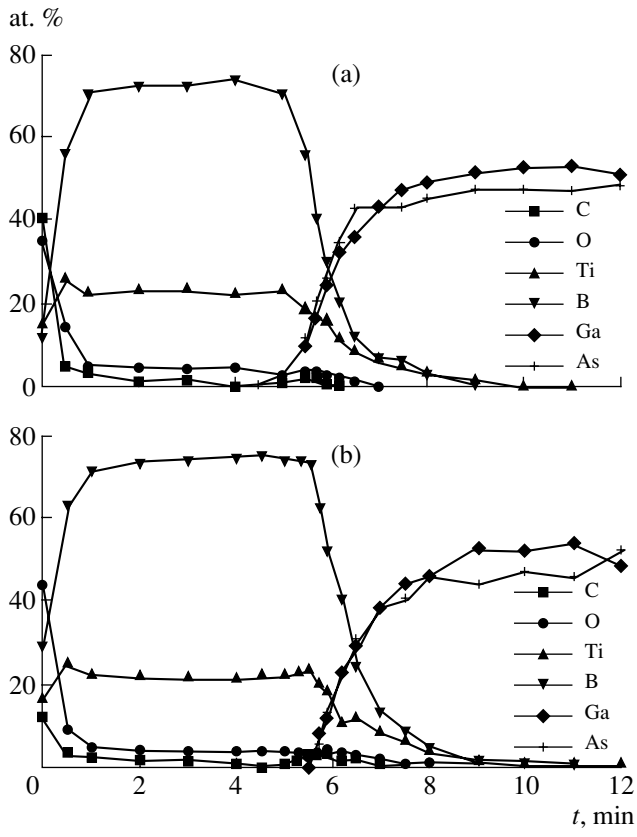

Fig. 1. Elemental composition profiles of a TiB_x–GaAs contact measured (a) before and (b) after annealing

phous titanium boride with high oxygen content. It was found that the thermal degradation in that system was caused by the structural and chemical transformation of deposited TiB_x layers, in which the dominating role belonged to Ti–B–O phases with variable compositions.

In the samples studied, the effect of thermal treatment is significantly different from that observed in [3]. Indeed, the profiles presented in Fig. 1 show that the thickness and atomic composition of the transition layer observed after annealing are virtually the same as those in the initial structures. At the same time, some changes in the elemental profiles of the contact indicate that certain phase transformations may take place in the transition layer as a result of thermal treatment.

The phase composition of the transition layer in the contact structure before and after annealing was studied by SIMS. Figure 2 shows the variation of the current of some polyatomic ions in the depth of the transition layer. Note that the secondary ion spectra contain the components with m/z = 155 and 192, which can be interpreted as representing ternary phases with the compositions $B_xGa_{1-x}As$ and $Ti_xGa_{1-x}As$. As can be seen, the annealing leads to a decrease in the content of $B_xGa_{1-x}As$ and a sharp increase in the content of $Ti_xGa_{1-x}As$, which is explained by thermostimulated reactions in the near-contact region of GaAs.

The formation of a $B_xGa_{1-x}As$ solid solutions in the initial stages of a titanium boride film growth and the behavior of this phase in the course of annealing was studied previously [2, 3]. Let us consider in more detail the $Ti_xGa_{1-x}As$ ternary phase, the formation of which in a contact structure is observed, to our knowledge, for the first time.

The interphase reactions in Ti–GaAs contacts, including those taking place at elevated temperatures, have been studied by many researchers in sufficient detail [4–6]. It has been established that an intense reaction between titanium and the semiconductor in the temperature interval from 380 to 500°C leads to the formation of a multiphase transition layer. The layer formed at 480°C is composed of TiAs and Ti_2Ga_3 phases, which transform on subsequent heating into Ti_5As_3 and Ti_5Ga_4, respectively. The compounds with arsenic appear at the initial Ti–GaAs interface, while the intermetallic Ga-containing phases grow on the arsenide front. No ternary phases were reported. Apparently, the formation of solid solutions in the Ti–GaAs system is also unlikely taking into account the sharp difference in the electron structure and the atomic radii of components in this heterocouple [7].

In order to explain the results obtained, we have to admit the possibility that solid solutions are formed on the basis of intermetallic compounds. This would remove the geometric and electrochemical restrictions on the phase formation [7].

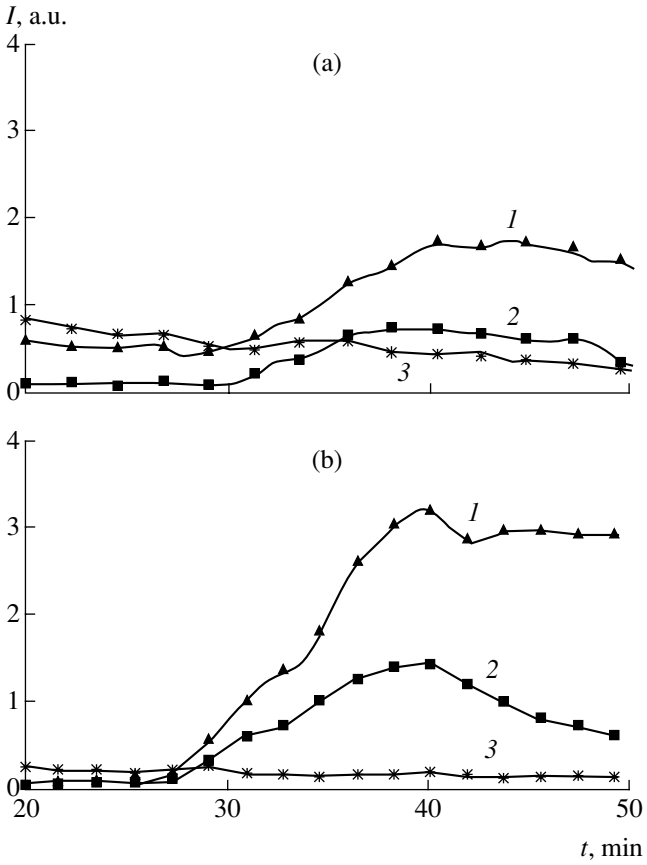

Fig. 2. Variation of the current of some polyatomic secondary ions in the depth of a transition layer in the TiB_x–GaAs contact measured (a) before and (b) after annealing: (*1*) GaAs; (*2*) $B_xGa_{1-x}As$; (*3*) $Ti_xGa_{1-x}As$.

We propose the following mechanism of the transition layer formation in the TiB_x–GaAs contact. In the initial structure, the contact interface comprises a thin layer of a $B_xGa_{1-x}As$ solid solution, while the Ti–As and Ti–Ga phase nuclei of subcritical size are situated below this layer. Occurring under the conditions of a sharp chemical potential gradient, these nuclei are unstable and their growth involves an increase in the free energy. Therefore, further evolution is related to the interaction between nuclei. A thermodynamically favorable pathway consists in suppressing the growth of subcritical nuclei by their merging together with the formation of a ternary phase, followed by the growth of this phase. If the collisional processes lead to the appearance of aggregates with dimensions exceeding a critical level (e.g., upon merging subcritical nuclei of the Ti–As and Ti–Ga phases with the formation of a supercritical ternary phase nucleus), the thermodynamic restrictions on further growth will be removed. An increase in the temperature would intensify this process. This course of events by no means imply that the growth of some binary phase (in addition to the ternary phase) is prohibited, because the fluctuational pro-

cesses may lead to the appearance of binary critical nuclei as well.

An analysis of the above data shows evidence of a sufficiently high thermal stability of the TiB_x–GaAs interface, which indicates the possibility of creating thermostable diodes with Schottky barriers employing such contacts. The results of measurements of the current–voltage characteristics of TiB_x–GaAs structures before and after annealing showed that the Schottky barrier height amounts to $\varphi_B = 0.78 \pm 0.02$ eV and is not affected by the treatment. The ideality factor calculated using the forward branch of the characteristic was even improved, to reach 1.15 upon annealing instead of 1.2 for the initial structures. The annealed samples also exhibited a significant decrease in reverse current.

REFERENCES

1. E. F. Venger, R. V. Konakova, G. S. Korotchenkov, V. V. Milenin, É. V. Russu, and I. V. Prokopenko, *Interphase Interactions and Mechanisms of Degradation in Structures of InP and GaAs Metals* (KTNK, Kiev, 1999).
2. I. B. Ermolovich, R. V. Konakova, V. V. Milenin, and A. I. Senkevich, Pis'ma Zh. Tekh. Fiz. **25** (19), 71 (1999) [Tech. Phys. Lett. **25**, 789 (1999)].
3. E. F. Venger, V. V. Milenin, I. B. Ermolovich, *et al.*, Fiz. Tekh. Poluprovodn. (St. Petersburg) **33** (8), 948 (1999) [Semiconductors **33**, 865 (1999)].
4. O. Wada, S. Yanagisawa, and H. Takanashi, Appl. Phys. Lett. **29** (4), 263 (1976).
5. C. E. MaCants, T. Kendelewicz, P. H. Mahowald, *et al.*, J. Vac. Sci. Technol. A **6** (3), 1466 (1988).
6. Ki Bum Kim, M. Kniffin, R. Sinclair, and C. R. Helms, J. Vac. Sci. Technol. A **6** (3), 1473 (1988).
7. B. F. Ormont, *Introduction to Physical Chemistry and Crystal Chemistry of Semiconductors* (Vysshaya Shkola, Moscow, 1968).

Translated by P. Pozdeev

Technical Physics Letters, Vol. 27, No. 7, 2001, pp. 589–591. Translated from Pis'ma v Zhurnal Tekhnicheskoĭ Fiziki, Vol. 27, No. 14, 2001, pp. 36–41.

Surface Carbides in the Sequence of Phase Equilibria in a Binary (Tungsten–Carbon) System

N. R. Gall'

Ioffe Physicotechnical Institute, Russian Academy of Sciences, St. Petersburg, 194021 Russia

Received September 29, 2000

Abstract—The place of surface carbides in the sequence of phase equilibria is considered as reflected by the tungsten–carbon equilibrium phase diagram. It is shown that the temperature dependence of the critical concentration of dissolved carbon, at which the surface carbide formation on the (100)W single crystal face is completed, is described by a curve lying in the bulk-single-phase region of the W–C solid solutions and dividing this region into two parts (α phase vs. α + surface carbide). An approximated formula is suggested that describes the critical concentration–temperature relationship. *© 2001 MAIK "Nauka/Interperiodica".*

Previously, we reported on the surface carbides observed in a series of refractory metals including (100)W [1], (100)Re [2], (100)Mo [3], and (111)Ni [4]. The physicochemical properties of surface carbides are much like those of the analogous bulk compounds, differing significantly from the properties of reagents (pure metal surfaces and adsorbed carbon). The surface carbide composition is characteristic of a given surface, usually being stoichiometric with respect to metal atoms in the uppermost surface layer (WC, MoC, …), that is, representing daltonides. At present, the concept of the surface compound formation on refractory metals is commonly accepted [1–6]. However, despite wide occurrence of the surface carbides, their place in the hierarchy of solid-state metal–carbon reaction products (and in the corresponding binary phase diagrams) is not yet completely clear.

The formation and properties of surface carbides. Let us consider the laws of the surface carbide formation in a thoroughly studied C-W(100) system. As was demonstrated previously [1], upon the adsorption of carbon atoms at an amount of 1×10^{15} cm^{-2} on a thoroughly decarbonized (100) single crystal tungsten surface at 1500 K, only a small fraction of the adsorbate remains on the surface while most of the above amount dissolves in the bulk. In the experiments, carbon was deposited by 5×10^{14} cm^{-2} portions from an absolutely calibrated flux of C atoms under ultrahigh vacuum conditions ($P \sim 10^{-10}$ Torr) excluding both the surface contamination with carbon and the loss of adsorbed carbon. After depositing each portion of the adsorbate, the sample was annealed at temperatures gradually increasing (at an increment of 100 K) up to 2500 K. The state of the surface in the course of annealing was monitored by Auger electron spectroscopy (AES). When the total deposited carbon dose reaches $\sim 3 \times 10^{15}$ cm^{-2}, carbon begins to accumulate on the surface. At a total dose of $\sim 5 \times 10^{15}$ cm^{-2}, the sample shows evidence of the surface carbide formation with a WC stoichiometry relative to the density of surface metal atoms, the concentration of carbon atoms in this state being 1×10^{15} cm^{-2}. The remainder of the deposited carbon occurs in the bulk of tungsten.

Cooling the system to 800 K (at this temperature, the diffusion of carbon in the metal bulk is frozen) and to still lower temperatures does not affect the surface carbide composition. On the contrary, heating the samples to 2100–2200 K leads to a reversible removal of carbon from their surface; on subsequent cooling to $T < 1500$ K, the surface carbide builds up on the surface again [1].

The results of direct AES measurements [1] showed that, under the deposition conditions indicated above, carbon penetrates through a ~10-μm-thick ribbon tungsten sample over ~10 s, after which the surface carbide forms simultaneously on both sides of the ribbon. If the deposition is continued, at least up to a dose of $\sim 10^{18}$ cm^{-2}, all the carbon atoms reaching the surface dissolve in the bulk of tungsten, not changing the surface carbide composition. However, as the volume concentration of carbon increases, the beginning and end of the temperature interval corresponding to dissolution of the surface carbon in the bulk shift by ~200 K toward higher temperatures, although the process of carbon dissolution and withdrawal still remains reversible. This reversibility, as well as the fact that the whole metal volume is involved in the carbon dissolution and withdrawal process, indicate that the surface carbide is in equilibrium with the metal bulk.

Let us estimate the bulk concentration of carbon atoms n_C in a sample at the end of the surface carbide formation. Let $N_S = 1 \times 10^{15}$ cm^{-2} be the surface concentration of carbon (in the surface carbide), N_{tot} is the deposited dose, and $\underline{L} = 0.01$ mm $= 1 \times 10^5$ Å is the

1063-7850/01/2707-0589$21.00

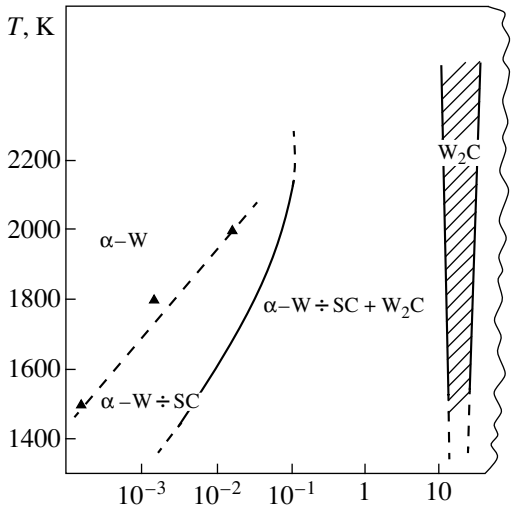

A fragment of the solidus domain of the equilibrium phase diagram of the W–C system [8] (replotted on a semilogarithmic scale) showing the region of existence of a surface carbide (SC) on the (100)W single crystal face: the solid curve represents the $n_{\text{lim}} = f(T)$ relationship (plotted by data from [7]); triangles (and the approximating dashed line) show the $n_{\text{cr}} = f(T)$ relationship.

sample thickness. The sample volume V_b per unit surface area (cm^2) is

$$V_b = 1\ \text{cm}^2\ 0.001\ \text{cm} = 0.001\ \text{cm}^3. \quad (1)$$

The amount of carbon atoms N_b (per unit surface area) dissolved in this volume with an allowance for the surface carbide formation on both sides of the tungsten ribbon is

$$N_b = N_{\text{tot}} - 2N_S = 5 \times 10^{15} - 2 \times 1 \times 10^{15} = 3 \times 10^{15}. \quad (2)$$

Assuming the sample to be homogeneous, we may expect that the equilibrium concentration of carbon throughout the volume is constant and equal to

$$n_C = N_b/V_b = 3 \times 10^{18}\ \text{cm}^{-3}, \quad (3)$$

which is equivalent to $\sim 1.5 \times 10^{-2}$ at. %.

The place of surface carbides in the sequence of phase equilibria in the C–W system. Now let us find the place of surface carbides in the sequence of phase transformations. Consider a fragment of the phase diagram of the W–C system depicted in the figure (taken from [8] and replotted for convenience on a semilogarithmic scale). Dependence of the limiting solubility on the temperature at $T > 1500$ K is described by the formula [7]

$$\log n_{\text{lim}} = 2.03 - 6510/T, \quad (4)$$

where T is the absolute temperature and n_{lim} is the limiting concentration of carbon (expressed in at. %). As can be seen, the limiting solubility of carbon in tungsten in the temperature interval from 1500 to 2000 K amounts to 0.07–0.3 at. %. The region on the left from this curve corresponds to the bulk-single-phase states representing a solid solution of carbon in tungsten (α phase), while the region on the right represents two-phase states (α-W + W_2C).

As can be seen, the concentrations of dissolved carbon at which the surface carbide phase is stable ($\sim 1.5 \times 10^{-2}$ at. %) are significantly lower than the limiting solubility. Previously [1], we measured a change in the equilibrium surface concentration of carbon on (100)W depending on the amount of carbon dissolved in the bulk. Using this dependence, we determined the temperature corresponding to the onset of the surface carbide degradation as a function of the bulk concentration of carbon dissolved in tungsten. These concentrations are also plotted in the W–C phase diagram presented in the figure. As can be seen, this plot divides the region of the α phase into two parts representing α-W with the (100)W face free of the surface carbide and α-W + surface carbide, in addition to the curve of limiting concentrations dividing the phase diagram. By analogy, the former values are called the "critical" concentrations for the surface carbide formation and are denoted by n_{cr}.

Using the experimental data, the temperature variation of n_{cr} can be approximated by a linear function. Using the least squares method, we obtained an expression for this approximation

$$n_{\text{cr}} = -4.7 + T/250, \quad (5)$$

where the values are expressed in the same units as in formula (4).

Discussion of results. The notion of the "surface phases" and "surface compounds" was introduced into modern thermodynamics by Prigogine [9], after which Guttmann and McLean [10] showed that the surface phases are equivalent to the bulk ones, for example, with respect to the Gibbs phase rule applied to systems with surfaces. The surface carbide considered in this study is a typical surface compound. Therefore, a relationship between this surface phase and the equilibrium bulk phases is important, especially in the systems where the surface plays a significant role (thin films, small metal clusters, nanosized objects, etc.).

It must be specially noted that speaking of a purely "surface" phase diagram (e.g., of the C–(100)W system, as it was proposed in [11]) seems to be unjustified since the very existence of the surface carbide and the region of its stability depend significantly on the bulk concentration of carbon present in the sample in the form of a solid solution. In equilibrium, the surface of a pure tungsten sample will expose different single crystal faces [12], including (experimentally proven) the (100) face. As for the equilibrium habit of tungsten crystals formed in the presence of a small amount of carbon, no data in this respect are available (to the author's knowledge). However, our experimental data

also indicate that the (100) with surface carbide certainly enters into the faceting pattern. At present, it is unknown how the character of the $n_{cr} = f(T)$ curve will change over the passage to other single crystal faces; moreover, it is not even known whether the equilibrium surface carbides may exist at all on the other faces of tungsten.

Conclusions. It is demonstrated that the region of existence of a solid solution in the solidus domain of the W–C equilibrium phase diagram can be conventionally divided into two parts representing an α phase with the surface free of surface carbide and the states of α + surface carbide. The temperature dependence of the critical concentration of carbon in the bulk necessary for the existence of equilibrium surface carbide on the (100)W face is determined. Apparently, analogous modifications can be introduced into the phase diagrams of other metals capable of forming surface carbides, such as Mo, Re, and Ni.

Acknowledgments. This study was supported by the Ministry of Science of the Russian Federation within the framework of the "Surface Atomic Structures" Program (project no. 4.6.99).

REFERENCES

1. N. R. Gall', E. V. Rut'kov, and A. Ya. Tontegode, Izv. Akad. Nauk, Ser. Fiz. **62** (10), 1980 (1998).
2. N. R. Gall, S. N. Mikhailov, E. V. Rut'kov, and A. Ya. Tontegode, Surf. Sci. **191**, 185 (1987).
3. E. V. Rut'kov, A. Ya. Tontegode, M. M. Usufov, and N. R. Gall, Appl. Surf. Sci. **78**, 179 (1994).
4. E. V. Rut'kov, A. Ya. Tontegode, and M. M. Usufov, Izv. Akad. Nauk, Ser. Fiz. **58** (10), 102 (1994).
5. C. H. Peterson and R. M. Lamber, Surf. Sci. **187**, 339 (1987).
6. K. Schwaha, N. D. Spencer, and R. M. Lambert, Surf. Sci. **81**, 273 (1979).
7. E. Fromm and E. Gebhardt, *Gase und Kohlestoff in Metalen* (Springer-Verlag, Berlin, 1976).
8. L. Toth, *Transition Metal Carbides and Nitrides* (Academic, New York, 1971; Mir, Moscow, 1974).
9. R. Defay, I. Prigogine, A. Bellmans, and D. H. Everett, *Surface Tension and Adsorption* (Wiley, New York, 1966).
10. M. Guttmann and D. McLean, in *Interfacial Segregation*, Ed. by W. C. Johnson and J. M. Blakely (American Society for Metals, Metal Park, 1979), pp. 261–347.
11. J. M. Blakely and H. V. Thapliyal, in *Interfacial Segregation*, Ed. by W. C. Johnson and J. M. Blakely (American Society for Metals, Metal Park, 1979), pp. 137–174.
12. C. Herring, in *Structure and Properties of Solid Surfaces*, Ed. by R. Gomer and C. S. Smith (Univ. of Chicago Press, Chicago, 1953), pp. 5–72.

Translated by P. Pozdeev

Technical Physics Letters, Vol. 27, No. 7, 2001, pp. 592–593. Translated from Pis'ma v Zhurnal Tekhnicheskoĭ Fiziki, Vol. 27, No. 14, 2001, pp. 42–45.

The Fractal Analysis of a Porous Material Structure

V. V. Polyakov* and S. V. Kucheryavskiĭ

Altaĭ State University, Barnaul, Russia

** e-mail: polyakov@phys.dcn-asu.ru*

Received March 7, 2001

Abstract—The structure of porous copper and iron materials with a porosity ranging from 5 to 45% was studied by fractal analysis. A relationship between the fractal dimension of the porous space boundary and the porosity value is established. A correlation between topological features of the porous material structure and the fractal dimension of the interface is revealed. © *2001 MAIK "Nauka/Interperiodica".*

Porous materials represent a special class of disordered media possessing certain features hindering the application of the traditional methods of structure description [1]. An effective tool for the investigation of such materials is offered by the fractal geometry formalism. This approach provides for an adequate description of a porous structure and allows a relationship to be established between the structural parameters and physicochemical characteristics of a given material [2, 3]. The purpose of this study was to use fractal analysis for the description of a porous space structure in copper and iron powder-based materials.

The samples for investigation were prepared by pressing metal copper and iron powders with an average particle size of 25 μm (Cu) and 80 μm (Fe) to a preset porosity, followed by sintering in vacuum at 1100 K (Cu) and 1300 K (Fe). The conditions of sintering were selected so as to ensure the formation of metal–metal bonds between powder particles before the onset of melting. The sample porosity P was varied between 5 and 45%, which allowed various topologies of the porous strictures to be studied. For the P values below ~10%, the porous space consisted of isolated "clusters" representing intra- and intergranular pores. For $P \sim$ 10–15%, which corresponds to a percolation threshold, the intergranular pores formed an "infinite" cluster. As the porosity level was increased further up to $P \sim 30\%$ and above, the metal framework and intergranular space rearranged itself so as to represent geometrically equivalent interpenetrating clusters. The volume of isolated intragranular pores remained unchanged, while their relative contribution to the total porosity decreased with increasing P.

The fractal analysis of the porous structure was performed by the method of cut islands [4]. Using this technique, it is possible to pass from studying a complicated three-dimensional porous surface to the analysis of a planar system of self-similar curves formed upon cutting the sample with a horizontal sectioning plane. The cross section plane image observed in an optical microscope was fed via an interface into a computer. The fractal dimension D of the porous space boundary (interface) was determined by a special program based on calculating the ratio of the perimeter L to the area S of the curves representing the interface in the sample section. Data on the perimeter to area ratios were presented in the following form:

$$L(\delta) = \delta^{1-D}[S(\delta)]^{D/2},$$

where δ is the linear size of a standard cell used in the measurements. In iron samples, the fractal dimension was calculated both for the whole porous space and separately for the inter- and intragranular pores. In copper, the D values were determined only for the whole porous space.

Figure 1 shows the fractal dimension D of the boundaries of inter- and intragranular pores in iron plotted versus the sample porosity P. As can be seen, the D values for intragranular pores are close to unity in the entire porosity range studied. From this we infer that the boundaries of these pores (formed primarily in the course of obtaining the initial powder) are relatively "smooth."

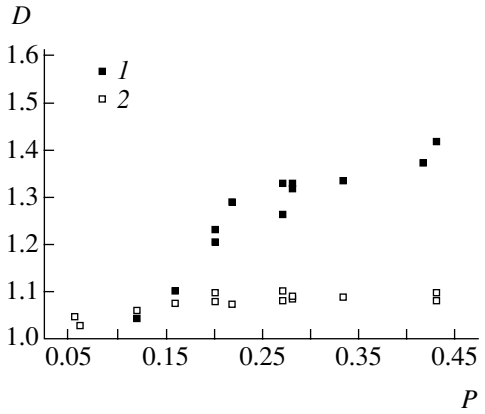

Fig. 1. The plot of fractal dimension D versus porosity P for the (*1*) intergranular and (*2*) intragranular pore boundaries in iron samples.

1063-7850/01/2707-0592$21.00 © 2001 MAIK "Nauka/Interperiodica"

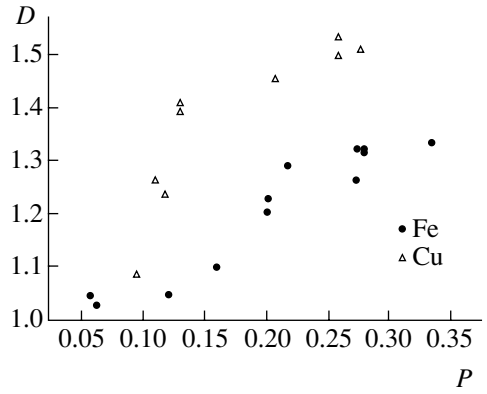

Fig. 2. The plot of fractal dimension *D* versus porosity *P* for the pore space boundaries in iron and copper samples.

The plot of *D* versus *P* for the intergranular pores exhibits a more complicated shape. According to Fig. 1, the pore boundary dimension is close to unity for *P* values below the percolation threshold. In the porosity interval from 10 to 20%, the fractal dimension exhibits a jump evidencing a significant complication of the boundary shape in these samples. This is related to the formation of an "infinite" porous cluster from separate intergranular pores. At high porosities (~30% and above), corresponding to the coexistence of geometrically equivalent porous and metal framework clusters, the fractal dimension also remains almost unchanged with increasing porosity.

Figure 2 shows the plots of the fractal dimension (determined for the whole porous space) versus porosity for the iron and copper samples. As can be seen, these data reveal qualitatively the same behavior in both metals. The experimental points for copper lie above those for iron at the same porosity. This is explained by a somewhat different structure of the porous space formed as a result of sintering in a more finely dispersed copper powder. The copper samples were characterized by a distribution of numerous small pores among coarse pores. This type of structure is closer to ideal self-similar objects such as the Menger sponge [5], which is manifested by greater *D* values.

Thus, the results of our investigation showed that a fractal dimension of the porous space boundary depends significantly on the porosity and topological features of the structure of porous materials. These results can be used for the description of porous structures and for the interpretation of structure–property relationships in porous materials.

REFERENCES

1. V. V. Polyakov and A. V. Golovin, Pis'ma Zh. Tekh. Fiz. **20** (11), 54 (1994) [Tech. Phys. Lett. **20**, 452 (1994)].
2. J. Feder, *Fractals* (Plenum, New York, 1988; Mir, Moscow, 1991).
3. A. B. Mosolov and O. Yu. Dinariev, Zh. Tekh. Fiz. **58** (2), 233 (1988) [Sov. Phys. Tech. Phys. **33**, 145 (1988)].
4. V. S. Ivanov, A. S. Balankin, I. Zh. Bunin, and A. A. Oksogoev, *Synergetics and Fractals in Materials Science* (Nauka, Moscow, 1994).
5. B. B. Mandelbrot, *The Fractal Geometry of Nature* (Freeman, New York, 1983).

Translated by P. Pozdeev

Technical Physics Letters, Vol. 27, No. 7, 2001, pp. 594–595. Translated from Pis'ma v Zhurnal Tekhnicheskoĭ Fiziki, Vol. 27, No. 14, 2001, pp. 46–50.

Stable Thermomagnetic Waves in Hard Superconductors

N. A. Taylanov* and U. T. Yakhshiev

Institute of Applied Physics, Department of Theoretical Physics,
National University of Uzbekistan, Tashkent, Uzbekistan
** e-mail: taylanov@iaph.silk.org*

Received January 30, 2001

Abstract—The problem of the stability of a nonlinear thermomagnetic wave with respect to small thermal and electromagnetic perturbations in hard superconductors was studied. It is shown that spatially bounded solutions may correspond only to the perturbations decaying with time, which implies stability of the nonlinear thermomagnetic wave. © *2001 MAIK "Nauka/Interperiodica".*

Previously [1], it was demonstrated that, depending on the surface conditions, stationary nonlinear thermomagnetic waves of two types, **E** and **H**, may exist in a superconductor. However, the problem of stability of the nonlinear waves with respect to small thermal and electromagnetic perturbations in superconductors is insufficiently studied.

We will consider the stability of a nonlinear thermomagnetic wave with respect to small thermal and electromagnetic perturbations in a superconductor occurring in the critical state. It will be demonstrated that spatially bounded solutions may correspond only to the perturbations decaying with time.

The evolution of the thermal (T) and electromagnetic (**E** and **H**) perturbations in a superconductor is described by a nonlinear thermal conductivity equation [1–4]

$$\nu(T)\frac{dT}{dt} = \Delta[\kappa(T)\Delta T] + \mathbf{jE}, \tag{1}$$

in combination with the Maxwell equations

$$\mathrm{rot}\mathbf{E} = -\frac{1}{c}\frac{d\mathbf{H}}{dt}, \quad \mathrm{rot}\mathbf{H} = \frac{4\pi}{c}\mathbf{j} \tag{2}$$

and the critical state equation

$$\mathbf{j} = \mathbf{j}_c(T, \mathbf{H}) + \mathbf{j}_r(\mathbf{E}), \tag{3}$$

where $\nu = \nu(T)$ and $\kappa = \kappa(T)$ are the heat capacity and thermal conductivity coefficients, respectively; $\mathbf{j}_c$ is the critical current density; and $\mathbf{j}_r$ is the resistive current density.

Let us consider a plane semiinfinite sample ($x > 0$) exposed to an external magnetic field $\mathbf{H} = (0, 0, H_e)$ increasing with time at a constant rate $\frac{d\mathbf{H}}{dt} = \text{const}$. According to the Maxwell equation (2), the sample will feature a vortex electric field $\mathbf{E} = (0, E_e, 0)$ parallel to the current density vector: $\mathbf{E} \parallel \mathbf{j}$.

In order to describe the $j_c(T, H)$ function, we will use the Bean–London equation of the critical state $\left(\frac{dj_c}{dH} = 0\right)$ [5]. According to this model, the $j_c(T)$ function can be presented as $j(T) = j_c(T_0)\left[1 - \frac{T - T_0}{T_c - T_0}\right]$, where $j_0 = j_c(T_0)$ is the equilibrium current density, T_c is the critical temperature, and T_0 is the cooler temperature.

The characteristic form of $j_r(E)$ in the region of sufficiently strong electric fields ($E > E_f$) can be approximated by a piecewise linear function $j_r \approx \sigma_f E$. In the region of small field strengths ($E < E_f$), the $j_r(E)$ function exhibits a nonlinear character related to a thermoactivated flux creep [6].

For an automodel solution of the type $\xi = x - vt$ describing a wave propagating at a constant velocity v along the x axis, the system of Eqs. (1)–(3) acquires the following form:

$$-v[N(T) - N(T_0)] = \kappa\frac{dT}{d\xi} - \frac{c^2}{4\pi v}E^2, \tag{4}$$

$$\frac{dE}{d\xi} = -\frac{4\pi v}{c^2}j, \tag{5}$$

$$E = \frac{v}{c}H, \tag{6}$$

where $N(T) = \int_0^T \nu(T)dT$. Excluding variables T and H with the aid of expressions (4) and (6) and taking into account the boundary condition $E(z \longrightarrow -\infty) = E_e$, we arrive at a differential equation describing the distribution $E(\xi)$:

$$\frac{d^2E}{dz^2} + \beta\tau\frac{dE}{dz} + \frac{4\pi v^2}{c^2 E_\kappa}[N(T) - N(T_0)] - \frac{E^2}{2E_\kappa} = 0. \tag{7}$$

Here, $z = \frac{\xi}{L}$ and $\beta = \frac{\nu t_\kappa}{L}$ are dimensionless parameters, $L = \frac{cH_e}{4\pi j_0}$ is the magnetic field penetration depth into the superconductor, $\tau = \frac{D_t}{D_m}$ is the ratio of the coefficients of thermal ($D_t = \frac{\kappa}{\nu}$) and magnetic ($D_m = \frac{c^2}{4\pi\sigma_f}$) diffusion, $t_\kappa = \frac{\nu L^2}{\kappa}$ is the thermal diffusion time, and $E_\kappa = \frac{\kappa}{aL^2}$ is a constant parameter.

In the approximation of a weakly heated superconductor ($(T - T_0) \ll T_0$), the heat capacity ν and thermal conductivity κ coefficients are weakly dependent on the temperature profile. As is well known (see, e.g., [6]), the magnetic flux variations in a hard superconductor occur at a much greater rate as compared to those of the heat transfer, so that $\tau \ll 1$ or $D_t \ll D_m$. In this approximation, we may neglect the terms related to dissipative effects in Eq. (7), after which a solution to this equation can be presented in the following form [7]:

$$E(z) = \frac{E_1}{2}\left[1 - \tanh\frac{\beta\tau}{2}(z - z_0)\right]. \quad (8)$$

Relationship (8) describes the profile of a thermomagnetic shock wave propagating into the superconductor.

In order to study the stability of a nonlinear wave with respect to small perturbations, it is convenient to write a solution to Eqs. (1)–(3) in the following form:

$$\begin{aligned} T(z, t) &= T(z) + \delta T(z, t)\exp\left[\frac{\lambda t}{t_\kappa}\right], \\ E(z, t) &= E(z) + \delta E(z, t)\exp\left[\frac{\lambda t}{t_\kappa}\right], \end{aligned} \quad (9)$$

where $T(z)$, $E(z)$ are the stationary solutions and δT, δE are small perturbations. Substituting expressions (9) into Eqs. (1)– (3), assuming δT, $\delta E \ll T$, E in the limit of $\tau \ll 1$ (this corresponds to a "fast" instability, $\lambda \gg \frac{\nu v^2}{\kappa}$ [6]), we obtain an equation for determining the eigenvalues of λ [8]:

$$\frac{d^2\epsilon}{dz^2} + \left[\frac{2}{ch^2} - \Lambda\right]\epsilon = 0. \quad (10)$$

Using the substitution of variables of the type $\xi = \tanh y$, $1 - \xi = 2s$, and $\epsilon(\xi) = (1 - \xi^2)^{\frac{\Omega}{2}}\Phi(\xi)$, Eq. (10) can be reduced to a standard hypergeometric equation

$$\begin{aligned} s(1-s)\frac{d^2\Phi}{ds^2} - [\Omega + 1 - 2s(\Omega + 1)]\frac{d\Phi}{ds} \\ - [\Omega(\Omega - 1) - p(p - 1)]\Phi = 0. \end{aligned} \quad (11)$$

Here, the even and odd integrals can be presented as

$$\Phi_1 = F(\epsilon - 1, \epsilon + 2, \epsilon + 1, s), \quad (12)$$

$$\Phi_2 = s^{-\epsilon}F(-1, 2, 1 - \epsilon, s), \quad (13)$$

where F is the hypergeometric function [9]. The function Φ must be finite at the singular point $s = 1$. The ϵ values for which Φ_1 is finite evidently correspond to a discrete spectrum: $\epsilon_i = 0.1$ or $\lambda_i = -\tau^{-1}$, 0. The function Φ_2 is finite only for $\epsilon = 0$.

Any solution in the form of a running wave is characterized by translational symmetry, which implies that a "perturbed" stationary profile $E(z)$ determined by Eq. (8) corresponds to the eigenvalue of the ground state $\lambda_0 = 0$. Differentiating Eq. (7) with respect to z, one may readily see that $\frac{dE_0}{dz}$ is an eigenfunction corresponding to $\lambda_0 = 0$. Indeed, the perturbation $\delta E = \frac{dE_0}{dz}$ essentially represents a small wave displacement. Thus, we may suggest that the function $\frac{dE_0}{dz}$ exponentially tends to zero for $z \longrightarrow +\infty$ and the corresponding eigenvalue is zero. Therefore, the problem cannot possess positive eigenvalues and $\mathrm{Re}\lambda_i < 0$. This result implies that the wave is stable with respect to relatively small thermal (δT) and electromagnetic (δE) fluctuations. The analysis of the second linearly-independent solution leads to the same conclusion.

REFERENCES

1. I. L. Maksimov, Yu. N. Mastakov, and N. A. Taylanov, Fiz. Tverd. Tela (Leningrad) **28** (8), 2323 (1986) [Sov. Phys. Solid State **28**, 1300 (1986)].
2. N. A. Taylanov, Metallofizika **13** (9), 713 (1991).
3. N. A. Taylanov and S. Kuchkarov, Zh. Tekh. Fiz. **61** (7), 197 (1991) [Sov. Phys. Tech. Phys. **36**, 838 (1991)].
4. N. A. Taylanov and S. Kuchkarov, Fiz. Tverd. Tela (Leningrad) **33** (6), 1873 (1991) [Sov. Phys. Solid State **33**, 1052 (1991)].
5. C. P. Bean, Phys. Rev. Lett. **8** (6), 250 (1962).
6. R. G. Mints and A. L. Rakhmanov, *Instabilities in Superconductors* (Nauka, Moscow, 1984).
7. V. I. Karpman, *Nonlinear Waves in Dispersive Media* (Nauka, Moscow, 1973; Pergamon, Oxford, 1975).
8. L. D. Landau and E. M. Lifshitz, *Quantum Mechanics: Nonrelativistic Theory* (Fizmatgiz, Moscow, 1963; Pergamon, New York, 1977).
9. D. S. Kuznetsov, *Special Functions* (Vysshaya Shkola, Moscow, 1965).

Translated by P. Pozdeev

Technical Physics Letters, Vol. 27, No. 7, 2001, pp. 596–598. Translated from Pis'ma v Zhurnal Tekhnicheskoĭ Fiziki, Vol. 27, No. 14, 2001, pp. 51–55.

Parametric Amplification of Vortex Waves in an Acoustically Active Medium

N. E. Molevich

Samara State Aerospace University, Samara, Russia

e-mail: molevich@mb.ssau.ru

Received December 28, 2000

Abstract—The parametric interaction of acoustic waves with vortex waves in a gaseous medium is considered. It is shown that the parametric increment may become exponential in a thermodynamically nonequilibrium medium. © *2001 MAIK "Nauka/Interperiodica".*

As is known, the scattering of an acoustic wave on a vortex wave can take place even in a resting homogeneous medium. The induced scattering of sound on fluctuational vortices was originally described by Pushkina and Khokhlov in [1], where the scattering regime was assumed to be stationary and the initial equations did not take into account the second (volume) viscosity.

Below we will consider for the first time the case of nonstationary scattering and determine the time of attaining the stationary regime. It will be demonstrated that the second viscosity may significantly affect the process of scattering in a thermodynamically nonequilibrium gas.

For definiteness, consider the induced scattering of a high-frequency sound ($\omega\tau \gg 1$) on vortex waves in a vibrationally-excited gas in which the vibrational relaxation of molecules is described by a simple exponential model:

$$\frac{dE}{dt} = \frac{E_{eq} - E}{\tau(T, \rho)} + Q, \tag{1}$$

where E and E_{eq} are the vibrational energy per molecule and its equilibrium value, respectively; τ is the vibrational relaxation time; Q is the power of a pumping source maintaining a stationary degree of nonequilibrium; $S = Q\tau_0/T_0$; $\tau_0 = \tau(T_0, \rho_0)$; T, ρ, and T_0, ρ_0 are the gas temperature and density and their stationary values, respectively.

The sound fields can be represented as a superposition of the pumping wave (Π_0) and the Stokes scattered wave (Π_1):

$$\Pi = \frac{\Pi_0}{2}\exp[i(\mathbf{k}_0\mathbf{r} - \omega_0 t)] + \frac{\Pi_1}{2}\exp[i(\mathbf{k}_1\mathbf{r} - \omega_1 t)] + \text{c.c.}, \tag{2}$$

where $\Pi = P'/\rho_0 u_\infty^2$, P' is a pressure perturbation in the acoustic wave, u_∞ is the frozen velocity, and c.c. denotes the complex conjugate.

The vortex mode ($\mathbf{W} = \text{rot}\,\mathbf{V}$, where $\mathbf{V}$ is the velocity perturbation) will be represented by a running wave with the frequency $\Omega = \omega_0 - \omega_1$ ($\Omega \ll \omega_0, \omega_1$) and the wavevector $\mathbf{q} = \mathbf{k}_0 - \mathbf{k}_1$:

$$\mathbf{W} = \frac{1}{2}\mathbf{W}_0\exp[i(\mathbf{q}\mathbf{r} - \Omega t)] + \text{c.c.} \tag{3}$$

The standard procedure [1, 2] of truncating the initial system of the relaxation gasodynamic equations leads to the following set of equations describing the amplification of the scattered acoustic wave and the vortex wave in the field of a preset dissipative pumping wave (propagating along the X axis):

$$\frac{\partial \Pi_1}{\partial t} + u_\infty \cos\theta \frac{\partial \Pi_1}{\partial x} + g_1 u_\infty \Pi_1 = AW_0^* \cos\theta \Pi_0,$$

$$\frac{\partial W_0^*}{\partial t} + \alpha_W W_0^* = -iBu_\infty \Pi_1 \Pi_0^*, \tag{4}$$

$$\Pi_0 = \Pi^{(0)}\exp(-g_0 x).$$

Here, θ is the angle of scattering of the acoustic wave; $\mathbf{A} = [\mathbf{k}_0 \times \mathbf{k}_1]/2q^2$; $\mathbf{B} = [\mathbf{k}_0 \times \mathbf{k}_1](k_0 + k_1)g_1 u_\infty^3/\omega_1^2$; $\alpha_W = i\Omega + \nu q^2$; $g_1 = \alpha_\infty + \delta(\omega_1)$; $g_0 = \alpha_0 + \delta(\omega_0)$; $\delta(\omega) = \omega^2(2\nu/3 + \chi/2C_{V\infty})/u_\infty^3$ is the coefficient of sound absorption related to viscosity and thermal conductivity; ν and χ are the kinematic viscosity and thermal diffusivity coefficients, respectively; $\alpha_\infty = C_{V0}^2 \xi_0/2\rho_0 C_{V\infty}^2 \tau_0^2 u_\infty^3$ is the coefficient of sound absorption (for $\alpha_\infty > 0$) caused by relaxation processes in the medium related to the second viscosity; $\xi_0 = \tau_0(u_\infty^2 -$

$u_0^2)\rho_0 C_{V\infty}/C_{V0}$ is the low-frequency coefficient of the second viscosity; $C_{P\infty}$ and $C_{V\infty}$ are the frozen (high-frequency) heat capacities at constant pressure and volume, respectively; $C_{P0} = C_{P\infty} + C_K + S(\tau_T - \tau_\rho)$ and $C_{V0} = C_{V\infty} + C_K + S\tau_T$ are the equilibrium (low-frequency) heat capacities in the vibrationally-excited gas with a relaxation process described by Eq. (1) [3]; $\tau_T = \partial \ln \tau_0/\partial \ln T_0$; $\tau_\rho = \partial \ln \tau_0/\partial \ln \rho_0$; $C_K = dE_e/dT$; $u_0 = (C_{P0}T_0/C_{V0}m)^{1/2}$ is the equilibrium velocity of sound; and m is the molecular mass. All values are expressed in energy units.

In a vibrationally-excited gas, the second viscosity coefficient ξ_0 becomes negative for $S(C_{V\infty}\tau_\rho + \tau_T) + C_K < 0$ [3]. As a result, the coefficient α_∞ also changes sign and the medium becomes acoustically active for $g_0, g_1 < 0$, which implies that the sound wave is amplified rather than absorbed.

In the case of scattering at an angle of $\theta < \pi/2$, the boundary conditions for Eqs. (4) will be set in the form $\Pi^{(0)} = \text{const}$, $\Pi_1(0, t) = P_1(t)$, $W(x, 0) = 0$, and $\Pi_1(x, 0) = 0$. Upon applying double Laplace's transformation with respect to t and x to system (4), we eventually obtain

$$\Pi_1(x, t) = P_1(y)\exp(-g_1 x/\cos\theta)\eta(y) - \frac{1}{2}\int_0^t P_1(t-t')\frac{Z(x, t')}{y'} \times \exp(-\alpha_W y' - g_1 x/\cos\theta) J_1[Z(x, t')]\eta(y')dt', \quad (5)$$

$$\mathbf{W}_0^* = -i\mathbf{B}u_\infty \Pi^{(0)*}\int_0^t P_1(t-t') \times \exp(-\alpha_W y' - g_1 x/\cos\theta - g_0 x) J_0[Z(x, t')]\eta(y')dt', \quad (6)$$

where $y = t - x/u_\infty\cos\theta$; $y' = y(x, t')$; $Z(x, t) = \{2i\mathbf{BA}|\Pi^{(0)}|^2 y[1 - \exp(-2g_0 x)]/g_0\}^{1/2}$; J_n is the nth-order Bessel function of the first kind; and η is the Heaviside unit function.

A stationary scattering regime is established for $t \geq |t_{St}|$, where

$$t_{St} = -\frac{i\mathbf{BA}|\Pi^{(0)}|^2}{2\alpha^2 w g_0}[1 - \exp(-2g_0 x)] + \frac{x}{u_\infty \cos\theta} \quad (7)$$

is a complex time at which the integrand in (5) acquires a maximum value.

Substituting formula (7) into integrands of Eqs. (5) and (6) and using the steepest descent method (for $Z \gg 1$), we obtain the following expressions for the stationary increments of amplification of the vortex and Stokes scattered sound wave components:

$$G_1 = -\frac{2g_1 x}{\cos\theta} - \frac{|\mathbf{AB}||\Pi^{(0)}|^2 \Omega[1 - \exp(-2g_0 x)]}{(\Omega^2 + \nu^2 q^4)g_0}\operatorname{sgn} g_1, \quad (8)$$

$$G_W = G_1 - 2g_0 x.$$

For $g_0 x \ll 1$ and $g_1 > 0$, relationship (8) coincides with an expression derived in [1] by merely putting $g_1 = \delta$. In such a medium, no Stokes scattering in the forward direction takes place. It can be shown that, provided $|\Pi^{(0)}|^2$ is sufficiently large, the Stokes scattering is possible only in the reverse direction ($\pi/2 < \theta < \pi$), while the anti-Stokes scattering takes place in the forward direction ($\theta < \pi/2$). In an absorbing medium, the parametric increment is linear, while the nonlinear interaction length is restricted to $x \sim g_0^{-1}$.

The presence of a negative second viscosity dramatically changes the properties of the scattering process under consideration. According to Eqs. (8), the scattering process in an acoustically active medium has no threshold. For high pumping intensities (or large x values) the parametric increment of the Stokes scattering in the forward direction becomes exponential, rather than linear. The same is valid for the parametric increment of the anti-Stokes scattering (in the reverse direction).

Let us estimate G_W for a set of characteristic parameters of the problem under consideration: pumping wave intensity $I_0 = 10\ \text{W/m}^2$; $\theta = 15°$; $\nu = 2 \times 10^{-5}\ \text{m}^2/\text{s}$; $k_0 = 300\ \text{m}^{-1}$; gaseous medium under normal conditions. The calculation yields $G_W = 30$ for $g_0 x \approx -2.4$. With this parametric increment, the intensity of the vor-

tex component (arising from a thermal noise) becomes comparable with I_0. Thus, propagation of a high-power sound wave in an acoustically active medium may be accompanied by intense vortex formation.

In conclusion, we note that the process of stimulated sound scattering on the temperature waves is described by equations similar (to within the notation) to system (4) [2]. Therefore, the features of the process of stimulated scattering in the acoustically active medium revealed above must be manifested for the temperature waves as well. This problem will be considered in a separate paper.

REFERENCES

1. N. I. Pushkina and R. V. Khokhlov, Akust. Zh. **17** (1), 167 (1971) [Sov. Phys. Acoust. **17**, 144 (1971)].
2. F. V. Bunkin, K. I. Volyak, and G. A. Lyakhov, Akust. Zh. **28** (5), 607 (1982) [Sov. Phys. Acoust. **28**, 360 (1982)].
3. E. Ya. Kogan and N. E. Molevich, Zh. Tekh. Fiz. **56** (5), 941 (1986) [Sov. Phys. Tech. Phys. **31**, 573 (1986)].

Translated by P. Pozdeev

Technical Physics Letters, Vol. 27, No. 7, 2001, pp. 599–601. Translated from Pis'ma v Zhurnal Tekhnicheskoĭ Fiziki, Vol. 27, No. 14, 2001, pp. 56–62.

Buffer Layers for the Growth of $YBa_2Cu_3O_{7-x}$ Films on Silicon

S. V. Razumov and A. V. Tumarkin

St. Petersburg State Electrotechnical University, St. Petersburg, Russia

e-mail: thinfilm@eltech.ru

Received February 28, 2001

Abstract—Experimental structural characteristics of the $SrTiO_3$, $NdGaO_3$, and CeO_2 buffer films obtained by ion-plasma sputter deposition on silicon substrates are presented. It is demonstrated that the phase composition and the level of internal stresses in the films strongly depend on the deposition temperature. Optimum technological conditions for the growth of oriented $SrTiO_3$, $NdGaO_3$, and CeO_2 films on silicon are determined. The structural perfection of the buffer layers thus obtained is sufficient to provide for the subsequent growth of high-quality $YBa_2Cu_3O_{7-x}$ films on silicon substrates. © *2001 MAIK "Nauka/Interperiodica".*

The films of a high-T_c superconductor $YBa_2Cu_3O_{7-x}$ (YBCO) have proved to be a promising material for applications in both microwave and dc devices. At present YBCO films are already employed in various devices such as phase shifters, filters, and current limiters [1–4]. The technical characteristics of these high-T_c devices are comparable with (and sometimes even exceed) those of their semiconductor counterparts. However, the high-T_c devices are still not widely used in commercial devices, mostly because of the complicated technology and the need for high-cost substrate materials.

In order to increase the use of high-T_c materials in technology, it is necessary to develop methods for the growth and processing of such films that would be compatible with the semiconductor technologies. One of the possible ways consists in using common substrates employed in the semiconductor technologies—in particular, silicon—for the growth of high-T_c films.

The YBCO films grown by the existing methods directly on silicon possess a relatively low superconducting transition temperature (T_c), which can be explained by chemical interactions between the film and substrate at high deposition temperatures the required to obtain high-quality YBCO films. In order to avoid undesired interactions, it is necessary to introduce a buffer layer that would be a barrier against oxygen diffusion and provide for a structural matching of the film and substrate crystal lattices. From the standpoint of structural matching with YBCO, the best buffer layers are provided by $SrTiO_3$, $NdGaO_3$, and CeO_2 films. The first two of these materials are widely used for the growth of high-quality YBCO films [1, 4]. The lattice mismatch between the crystal structures of $SrTiO_3$ and $NdGaO_3$, on the one hand, and YBCO, on the other hand, amounts to 0.5 and 0.04%, respectively [5]. The buffer films of CeO_2 allow structurally perfect *c*-oriented YBCO films with high electrical properties to be obtained on sapphire substrates [6, 7]. The lattice mismatch between the CeO_2 and YBCO crystal structures amounts to 0.7% [5].

The results of our previous investigations [7–9] showed a strict correlation between the structural perfection of YBCO films and the phase composition of buffer layers. As for the sapphire substrates, a single-phase character of the buffer layer is a necessary condition to obtain oriented YBCO films possessing high electrical properties [7]. Thus, we may expect that the phase composition and internal stresses in buffer layers are factors of primary importance for the possibility of obtaining YBCO films with the characteristics acceptable for electronic device applications on silicon substrates.

We report on the results of investigating the structural characteristics of $SrTiO_3$, $NdGaO_3$, and CeO_2 buffer films on silicon substrates. Based on these data, the technological conditions needed to obtain single-phase buffer layers with minimum internal stresses were determined.

The films were prepared by ion-plasma sputtering of ceramic targets in a Leybold Z-400 system. The substrates represented (*h*00)-oriented silicon plates 10 × 10 mm in size. The oxygen pressure in the working chamber was 10 Pa and the substrate temperature T_s, monitored by a thermocouple, could be varied from 750 to 950°C. The discharge power was about 120 W. The time of deposition was 2 h. After termination of the process, the films were allowed to cool in an oxygen atmosphere at a rate of 2–3 K/min.

The structures of sputter-deposited films were studied by X-ray diffraction on a Geigerflex Rigaku-D/max diffractometer using monochromated Cu$K\alpha$ radiation. We established a correlation between the deposition (synthesis) temperature and phase composition of the deposit. The interplanar distances $d(h00)$ decreased

1063-7850/01/2707-0599$21.00 © 2001 MAIK "Nauka/Interperiodica"

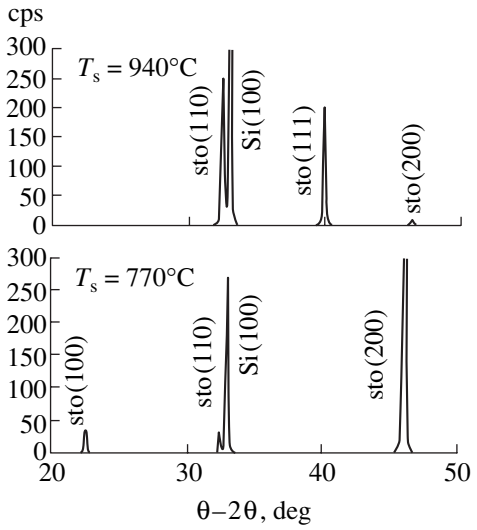

Fig. 1. X-ray diffractograms showing the effect of the substrate temperature on the phase composition of $SrTiO_3$ films grown on silicon.

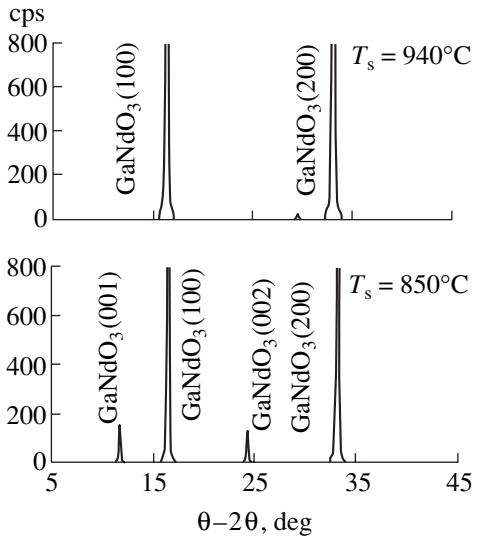

Fig. 2. X-ray diffractograms showing the effect of the substrate temperature on the phase composition of $NdGaO_3$ films grown on silicon.

with increasing deposition temperature for all the materials studied.

$SrTiO_3$ films. The phase composition of $SrTiO_3$ films on silicon is strictly determined by the temperature of synthesis as demonstrated in Fig. 1. For example, the $SrTiO_3$ film obtained at 940°C predominantly contains grains with the (*hkl*) and (*hk*0) orientations relative to the substrate surface, while the growth of (*h*00) blocks is suppressed. At the same time, X-ray diffractograms of the films deposited at 770°C contain the (100) and (200) reflections corresponding to the (*h*00) orientation, at a minimum level of signals due to inclusions of other phases. The interplanar distance *d*(200) decreases from 1.967 Å at 770°C to 1.951 at 940°C. Thus, the $SrTiO_3$ films deposited at 770°C possess predominantly the (*h*00) orientation, while a difference of the interplanar distance *d*(200) from that in the powder material (1.953 Å for a volume sample) is less than 2%.

$NdGaO_3$ films. In contrast to the case of $SrTiO_3$, increasing the temperature of $NdGaO_3$ synthesis leads to the growth of (*h*00)-oriented films (Fig. 2). However, single-phase $NdGaO_3$ films with this orientation grown under the conditions studied possess a lattice which somewhat contracted (as compared to the bulk sample) in the direction perpendicular to the substrate. Indeed, the interplanar spacing *d*(100) in the film synthesized at 940°C is 5.381 Å, while a volume sample has *d*(100) = 5.42 Å.

CeO_2 films. The interval of temperatures ensuring the growth of single-phase CeO_2 films on silicon is much narrower than the analogous temperature range for the growth of oriented $SrTiO_3$ and $NdGaO_3$ films. The CeO_2 films deposited at temperatures above 900 or below 800°C possess a polycrystalline structure with inclusions of the (*hkl*)- and (*h*00)-oriented grains. Single-phase (*h*00)-oriented CeO_2 films were obtained at 870°C (Fig. 3). The width (FWHM) of the (200) reflection peak was 0.24°, which is evidence of a well ordered coarse-block structure. The interplanar distance *d*(200) of the films grown at 780°C (2.706 Å) is close to that in the volume material (2.703 Å), which is indicative of the absence of internal stresses. An important fact is that the optimum temperature found in this study for the growth of single-phase CeO_2 films on silicon coincides with that for the growth of such films on sapphire substrates [8].

The results of our investigation showed that the growth of single-phase $SrTiO_3$, $NdGaO_3$, and CeO_2

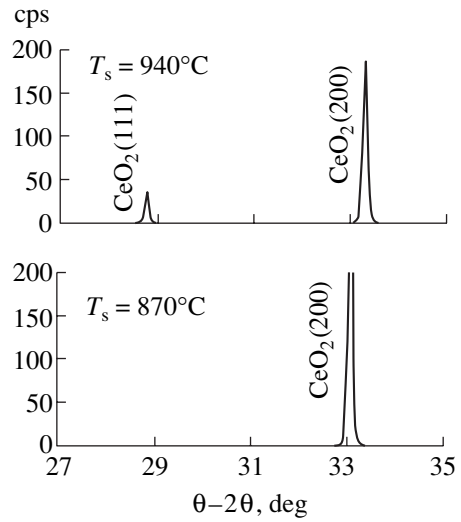

Fig. 3. X-ray diffractograms showing the effect of the substrate temperature on the phase composition of CeO_2 films grown on silicon.

buffer films with minimum internal stresses on silicon is possible provided that the optimum synthesis temperatures are employed. The high structural perfection of the films obtained gives us hope that the these buffer layers will provide for the subsequent growth of structurally perfect YBCO films. This will allow high-quality YBCO films on silicon substrates to be obtained for wide technical applications.

REFERENCES

1. O. G. Vendik, E. K. Hollmann, A. G. Zaitsev, *et al.*, J. Phys. D **28**, 1457 (1995).
2. V. Meerovich, V. Sokolovsky, G. E. Shter, *et al.*, Physica C (Amsterdam) **275**, 119 (1997).
3. O. G. Vendik, A. B. Kozyrev, T. B. Samoilova, *et al.*, J. Supercond. **10**, 63 (1997).
4. E. K. Hollmann, A. V. Ivanov, A. B. Kozyrev, *et al.*, in *Microwave Physics and Technique*, Ed. by H. Groll and I. Nedkov (Kluwer, Dordrecht, 1997), pp. 339–344.
5. E. K. Hollmann, O. G. Vendik, B. T. Melekh, *et al.*, Supercond. Sci. Technol. **7**, 609 (1994).
6. E. K. Hollmann, D. A. Plotkin, and S. V. Razumov, Zh. Tekh. Fiz. **69** (9), 132 (1999) [Tech. Phys. **44**, 1119 (1999)].
7. E. K. Hollmann, S. V. Razumov, and A. V. Tumarkin, Physica C (Amsterdam) **338**, 246 (2000).
8. E. K. Hollmann, S. V. Razumov, and A. V. Tumarkin, Pis'ma Zh. Tekh. Fiz. **25** (11), 47 (1999) [Tech. Phys. Lett. **25**, 440 (1999)].
9. V. V. Afrosimov, E. K. Gol'man, R. N. Il'in, *et al.*, Pis'ma Zh. Tekh. Fiz. **24** (1), 91 (1998) [Tech. Phys. Lett. **24**, 41 (1998)].

Translated by P. Pozdeev

Technical Physics Letters, Vol. 27, No. 7, 2001, pp. 602–604. Translated from Pis'ma v Zhurnal Tekhnicheskoĭ Fiziki, Vol. 27, No. 14, 2001, pp. 63–67.

The Interaction of Indocyanine Green Dye with the Human Epidermis Studied *in vivo*

É. A. Genina[a]*, A. N. Bashkatov[a], V. I. Kochubeĭ[a], V. V. Tuchin[a], and G. B. Al'tshuler[b]

[a] *Saratov State University, Saratov, Russia;*

** e-mail: eagenina@optics.sgu.ru*

[b] *Laser Research Center, Institute of High-Precision Mechanics and Optics, St. Petersburg, Russia*

Received December 5, 2000

Abstract—A shift of the light wavelength corresponding to the optical absorption peak of Indocyanine Green used for staining the horny layer of the human epidermis was measured *in vivo*. It is established that the dye molecules occur in both free and chemically bound state at the skin surface and only in the bound state at a depth of ~5 μm. *© 2001 MAIK "Nauka/Interperiodica".*

Indocyanine Green is a biologically active dye which is widely used in various fields of medicine owing to a strong optical absorption in the near IR range, low toxicity, and rapid elimination from the human organism. For a long time this compound was used only for diagnostic purposes [1–6]. However, in recent years the field of application has increased to include the phototherapy of tumors [7–11], photocoagulation [12] and repair (welding) [13] of tissues, and the treatment of skin and hair folliculi disorders [14], which is related to a significant optical absorption in the region of wavelengths generated by high-power diode lasers.

Indocyanine Green is a tricarbocyanine dye exhibiting a clearly pronounced absorption peak in the near IR range (~790 nm) and virtually not absorbing in the visible range. The compound corresponds to the empirical formula $C_{43}H_{47}N_2O_6S_2Na$ and has a molecular weight of 775. A relatively small width of the absorption peak allows this dye to be used in the selective laser thermolysis process, but the interaction with biological tissues leads to a change in the absorption spectrum of Indocyanine Green.

The interaction of Indocyanine Green dye (IGD) with cell proteins was experimentally studied. It was established that binding of the dye molecules to various organic molecules in biological tissues leads to a shift of the absorption peak toward longer wavelengths. The absorption peak maximum was observed at 805 nm in the human blood [15] and human skin *in vivo* [16] and at 810 nm in the epidermal cell cultures [17]. It should be noted that the reflected signal observed in [16] was formed predominantly in a deep layer of the skin characterized by a high blood supply. This circumstance explains the identical positions of the IGD absorption peak observed in the human blood and skin. Refinement of the wavelength corresponding to the maximum absorption of IGD interacting with the human skin *in vivo* is very important for correctly choosing the operating laser wavelength used for the selective laser thermolysis.

The purpose of this study was to determine *in vivo* a shift of the absorption maximum of IGD solutions used in the laser thermolysis process, which takes place as a result of the dye interaction with a horny layer (stratum corneum) of the human epidermis.

The experiments were performed with thin pieces of human skin stained with IGD solutions. The samples were obtained by layer-by-layer removal of the skin with the aid of a sticky ribbon (Multi-Film, Tesa, Biersdorf, Hamburg) from the same area (on the inner forearm surface). The absorption spectra of the samples attached to microscope glasses were measured in a wavelength range from 350 to 1200 nm using a CARY-2415 spectrophotometer equipped with an integrating sphere. We employed two dye solutions based on glycerol and ethyl alcohol. The first solution contained an additional component—dimethylsulfoxide (DMSO); the second solution contained a greater proportion of ethyl alcohol.

Figures 1 and 2 show the absorption (optical density) spectra of three sequentially separated skin layers stained with IGD solutions. The thickness of each layer was about 3–5 μm. As can be seen, the IGD absorption peak maximum in the skin is shifted toward longer wavelengths as compared to the peak in solution (the latter is shown for comparison in each figure with an intensity reduced by a factor of five). The shift is indicative of the fact that IGD molecules occur in a horny layer of the human epidermis in a chemically bound state.

In the spectra of samples prepared using the first solution (Fig. 1), the absorption peak shift amounts to 11 nm. In this experiment, the dye solution was thoroughly washed from the skin prior to sampling. The coincidence of the peak positions in the spectra of the

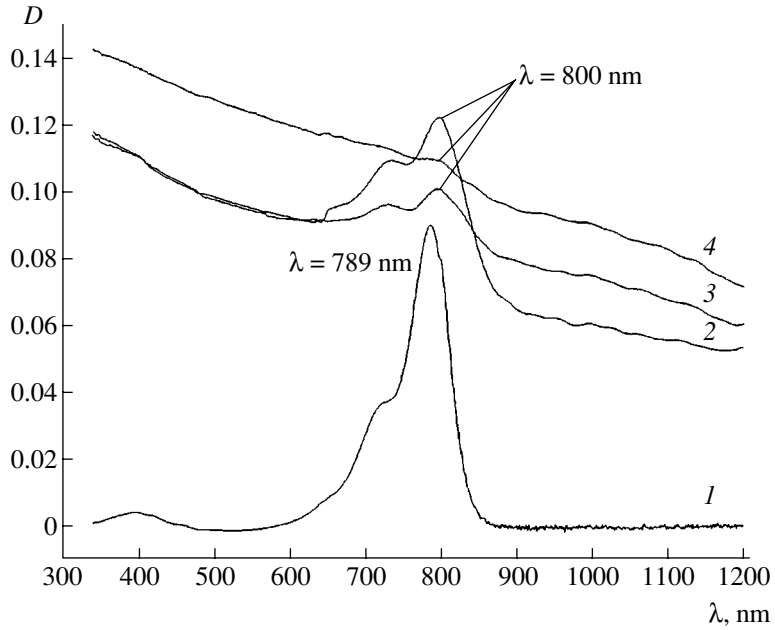

Fig. 1. Optical density spectra of Indocyanine Green (*1*) in a glycerol–ethanol–DMSO solution and (*2–4*) in three sequentially separated layers (first, second, and third, respectively) of the human skin stained with this solution.

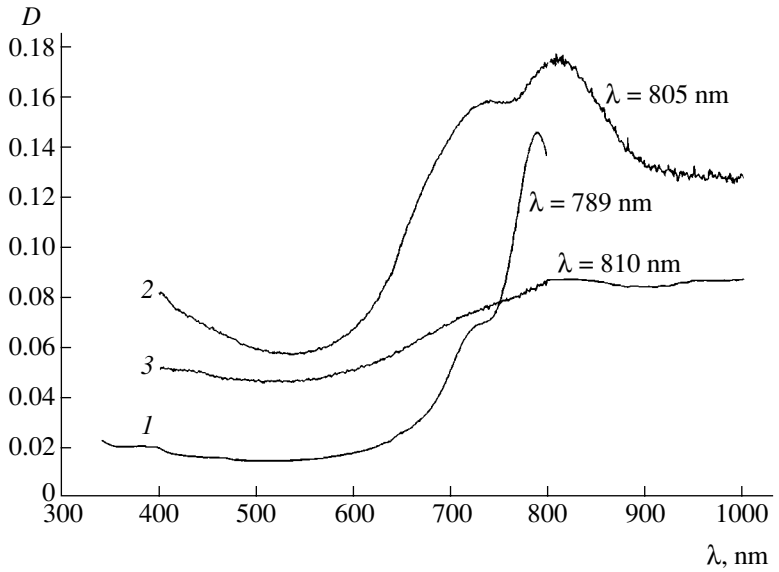

Fig. 2. Optical density spectra of Indocyanine Green (*1*) in a glycerol–ethanol solution and (*2*, *3*) in two sequentially separated layers (first and second, respectively) of the human skin stained with this solution.

first and second layers indicates that no free IGD molecules were present on the skin surface. In Fig. 2, the positions of maximum absorption in the spectra of the first and second layers are different: the latter peak is still longer wavelengths (by 21 nm) than the former one (16 nm). This difference suggests that the surface layer contains both free and bound dye molecules, whereas only the bound IGD is present at a depth of ~5 μm.

An analysis of the absorption spectra of IGD in solutions and tissues also revealed a change in shape of the spectra. The main peak significantly decreases in relative intensity and becomes comparable with the second peak observed at ~715 nm. This shape of the IGD spectrum is typical of the dye molecules in water, blood plasma, and albumin solutions [18]. Since a major protein in the human epiderm is keratin, the shift of the absorption peak position and the change in shape of the spectrum are most likely explained by the dye binding to keratin.

Thus, we have determined for the first time *in vivo* a shift of the absorption maximum of Indocyanine Green dye used to stain a horny layer of the human epidermis.

This change in the optical absorption spectrum of the dye widely used in selective laser thermolysis must be taken into account in choosing radiation sources ensuring the most effective removal of skin tumors, treatment of skin disorders, hair depilation, etc.

Acknowledgments. This study was supported by Palomar Medical Technologies Inc., the Russian Foundation for Basic Research ("Leading Scientific Schools" Program, project no. 00-15-96667), and the United States Civilian Research and Development Foundation for Independent States of the Former Soviet Union (CRDF).

REFERENCES

1. E. C. Bradley and J. W. Barr, Life Sci. **7**, 1001 (1968).
2. I. J. Fox and E. N. Wood, Mayo Clin. Proc. **35** (25), 732 (1960).
3. C. M. Leevy, F. Smith, J. Longueville, *et al.*, JAMA, J. Am. Med. Assoc. **200**, 236 (1967).
4. R. W. Flower and B. F. Hochheimer, Johns Hopkins Med. J. **138**, 33 (1976).
5. G. Monata, M. Brulisauer, K. Jager, *et al.*, Int. J. Microcirc. Clin. Exp. **6**, 25 (1987).
6. B. Riefke, K. Licha, W. Semmler, *et al.*, Proc. SPIE **2927**, 199 (1996).
7. W. R. Chen, R. L. Adams, S. Heaton, *et al.*, Cancer Lett. **88**, 15 (1995).
8. W. R. Chen, R. L. Adams, K. E. Bartels, *et al.*, Cancer Lett. **94**, 125 (1995).
9. W. R. Chen, R. L. Adams, A. K. Higgins, *et al.*, Cancer Lett. **98**, 169 (1996).
10. W. R. Chen, R. L. Adams, R. Carubelli, *et al.*, Cancer Lett. **115**, 25 (1997).
11. W. R. Chen, W.-G. Zhu, J. R. Dynlacht, *et al.*, Int. J. Cancer **81**, 808 (1999).
12. E. Reichel, C. A. Puliafito, J. S. Duker, *et al.*, Ophthalmic Surg. **25**, 195 (1994).
13. S. D. DeCoste, W. Farinelli, T. Flotte, *et al.*, Lasers Surg. Med. **12**, 25 (1992).
14. E. A. Genina, A. N. Bashkatov, Yu. P. Sinichkin, *et al.*, Proc. SPIE **4142**, 63 (2000).
15. C. Ciamberlini, V. Guarnieri, G. Longobardi, *et al.*, J. Biomed. Opt. **2**, 218 (1997).
16. R. A. Weersink, J. E. Hayward, K. R. Diamond, *et al.*, J. Photochem. Photobiol. **66**, 326 (1997).
17. S. Fickweiler, R.-M. Szeimies, W. Baumler, *et al.*, J. Photochem. Photobiol. B **38**, 178 (1997).
18. S. L. Lacques's website: www.omlc.ogi.edu

Translated by P. Pozdeev

Technical Physics Letters, Vol. 27, No. 7, 2001, pp. 605–607. Translated from Pis'ma v Zhurnal Tekhnicheskoĭ Fiziki, Vol. 27, No. 14, 2001, pp. 68–73.

Experimental Study of the Sound Amplification in a Vibrationally Excited Nonequilibrium Gas Plasma

G. A. Galechyan and A. R. Mkrtchyan

Institute of Applied Physical Problems, National Academy of Sciences of Armenia, Yerevan, Armenia

e-mail: malpic@iapp.sci.am

Received February 1, 2001

Abstract—The experimental study of the process of sound propagation along a positive column showed that the sound amplification in a stationary diffuse discharge in nitrogen obeys a linear theory. However, the discharge column contraction leads to a jumplike increase in the gain, in agreement with a nonlinear theory of the sound amplification in a vibrationally excited nonequilibrium molecular gas. *© 2001 MAIK "Nauka/Interperiodica".*

A linear theory of the sound wave amplification in a vibrationally nonequilibrium molecular gas was developed in [1–3]. The problems of nonlinear sound amplification at high gain levels, related to a sharp change in the temperature of medium and an explosive character of the wave propagation, were analyzed in [4, 5].

Below we report on the results of measurements of the sound wave amplification in a stationary diffuse discharge, upon the positive column contraction (pinching), in the continuous pinching regime, and in a sound-expanded discharge in nitrogen at a pressure of 78 Torr (the discharge pinching in nitrogen takes place at pressures $P \geq 78$ Torr).

The experiments were performed in a discharge tube with an internal diameter of 9.8 cm and a length of 52 cm, containing grid electrodes spaced 27 cm apart. A sound wave in the discharge tube was produced by an electrodynamic radiator mounted on the tube edge. A microphone mounted on the opposite edge was used to monitor the sound wave parameters. The sound frequency was controlled by a master oscillator, and the amplitude was controlled by an amplifier. A signal detected by the microphone was fed to an oscilloscope. The signal was calibrated with the aid of a spectrum analyzer. The measurements were performed in a range of discharge currents from 40 to 120 mA for the first resonance frequency f_1 = 170 Hz corresponding to a quarter wave (one edge flange was connected to a cavity with a diameter greater than the inner tube diameter [6, 7]). The tube was filled with nitrogen containing up to 0.07% water vapor and no more than 0.4% oxygen.

The current–voltage characteristics of discharge in a sound wave field measured at a nitrogen pressure of 78 Torr and a discharge current varied from 40 to 120 mA were reported previously [8]. According to those data, increasing the current from I_{d0} = 40 mA is accompanied by a decrease in the discharge voltage in the diffuse regime and the pinching effect is observed at a certain value of current (I_{d1}). For the discharge in nitrogen at P = 78 Torr, the pinching in the absence of a sound wave is observed at I_{d1} = 70 mA. The sound wave generation in the discharge shifts I_{d1} toward higher values. The discharge pinching consists in a jumplike decrease in diameter of the positive column and is accompanied by a ~1 kV drop in the interelectrode voltage and an increase in the current up to I_{d2}. The measurements were carried out at various initial sound wave intensities J_0 (for I_{d0} = 40 mA) varied from 66 to 88 dB. When the current was varied from 40 to 120 mA, the sound intensity was not maintained constant.

The plots of sound amplification coefficient K_i versus discharge current measured for various initial sound intensities J_0 are presented in the figure. In the interval from I_{d0} = 40 mA to I_{d1} = 73 mA (i.e., to the onset of pinching) at a sound intensity of J_0 = 68 dB (curve *1*), the discharge has a diffuse character. An increase in the current is accompanied by a gradual increase in the gain, which reaches $K_{i1} = 2.2$ m^{-1} at I_d = 73 mA. The amplification coefficient was determined as $K_{i1} = (\ln A_1/A_0)/L$, where A_0 and A_1 are the sound wave amplitudes at I_{d0} = 40 mA and I_{d1} = 73 mA, respectively, and L is the plasma column length. Upon the discharge pinching, the gain increases in a jumplike manner up to $K_{i2} = 5.2$ m^{-1} (i.e., by a factor of 2.4). The discharge current at the end of the pinching development is I_{d2} = 77 mA. This process is also accompanied by a jumplike decrease in position of the visible column boundary (from 5 to 0.5 cm). Subsequent increase in the discharge current from I_{d2} to I_{d3} = 120 mA in the pinching regime is accompanied by a monotonic growth in the sound amplitude, whereby the amplification coefficient also increases to $K_{i3} = 5.8$ m^{-1}.

1063-7850/01/2707-0605$21.00 © 2001 MAIK "Nauka/Interperiodica"

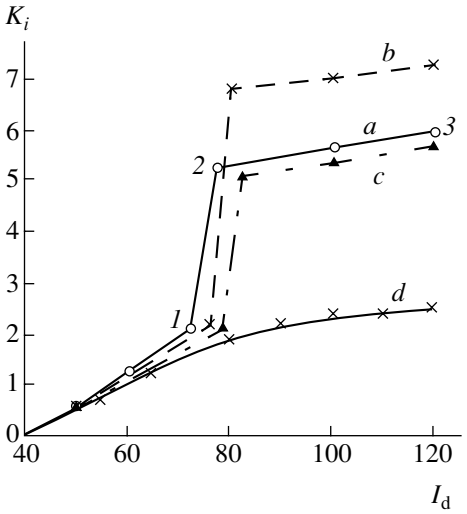

The plots of sound wave amplification coefficient K_i versus discharge current in nitrogen at a pressure of 78 Torr measured at a sound frequency of f_1 = 170 Hz and various initial intensities J_0 (dB): (*a*) 66; (*b*) 72; (*c*) 76; (*d*) 88 (unpinched discharge).

The results of our experiments showed that an increase in the sound intensity J_0 from 66 to 72 dB led to a growth in the magnitude of the gain jump upon the discharge pinching. A maximum jump in the gain was observed for J_0 = 72 dB. This case is illustrated by curve *b* in the figure: during the discharge pinching (for the current increasing from I_{d1} = 76 mA and I_{d2} = 80 mA), the gain increases up to K_{i2} = 6.6 m^{-1} (a threefold growth). The maximum sound amplification coefficient in the pinched discharge at I_{d3} = 120 mA was 7.2 m^{-1}. The gain level at I_{d1} in the diffuse discharge was identical for all initial sound intensities. In the pinched discharge, an increase in the gain observed for the current growing from I_{d2} to I_{d3} = 120 mA is approximately the same for all curves in the figure. An increase in the sound intensity up to J_0 = 88 dB leads to expansion (unpinching) of the positive column, which is explained by an acoustic vortex flow arising in the discharge tube under these conditions [7, 9]. As a result, the diameter of the visible discharge column exhibits a tenfold increase. In the unpinched discharge, the sound gain observed for the current increasing from I_{d0} 40 to I_{d3} = 120 mA is K_{i3} = 2.5 m^{-1}, with no jump in the sound amplitude as a result of the column contraction.

A mechanism of the sound amplification in a molecular gas (nitrogen) is related to the *V–T* relaxation of the vibrationally-excited states of molecules. The relaxation constant τ_{VT} depends on the gas temperature. For this reason, an increase in the current (leading to a growth in the plasma temperature) is accompanied by an increase in the *V–T* relaxation frequency and in the sound wave amplification coefficient. This behavior is consistent with the linear theory of sound amplification for a stationary discharge in a molecular gas [1–3].

The discharge pinching, accompanied by an increase in the gas temperature, changes the ratio of volume to wall deactivation of the vibrationally-excited molecules in favor of the former contribution. This transition may take the form of instability of the thermal explosion type caused by a strong temperature dependence of the vibrational relaxation constant. This instability development occurs provided that the characteristic time of the *V–T* relaxation at a temperature on the axis is comparable with the time of heat removal to the wall. The vibrational relaxation proceeds in an avalanche mode and the discharge passes to a stationary pinching regime. Here, virtually all the vibrationally excited molecules formed in the discharge are deactivated and a considerable proportion of energy supplied to the discharge is converted into heat. This leads to inhomogeneous temperature distribution in the plasma which, provided that a volume neutralization of charged particles takes place, leads to a sharp contraction of the discharge [10].

The sound wave propagation along the discharge leads to the modulation of the gas temperature and density and, hence, in the intensity of heat evolution related to the vibrational *V–T* relaxation. This, in turn, leads to an increase in the initial modulation amplitude of the gas temperature and density and to a growth in the sound intensity. Provided that the *V–T* relaxation time τ_{VT} upon the jumplike contraction is smaller than the sound wave period τ_S, the intensity of heat evolution (caused by the *V–T* relaxation) will be modulated by the sound wave. This leads to a significant growth in the initial amplitude of the gas temperature and density modulation and, hence, to a jump in the sound amplitude.

The results of temperature measurements (with a thermocouple junction placed at a distance of 8 cm from the anode) on the tube axis before the onset of charge pinching gave values not exceeding 860 K. Upon pinching, the temperature was established at 935 K. In pure nitrogen, the *V–T* relaxation constant at 900 K is $k_{VT} = 10^{-16}$ cm^{-3}/s [11] and the relaxation time is $\tau_{VT} = (k_{VT}N)^{-1} \cong 10^{-2}$ s. The period of the sound of oscillations is $\tau_S \cong 6 \times 10^{-3}$ s, so that $\tau_{VT} > \tau_S$. Since the gas used in our experiments contained up to 0.07% of water vapor, the actual situation is somewhat different. At 900 K, the vibrational relaxation constant for nitrogen on water is $k_{VT} = 10^{-13}$ cm^{-3}/s [12]. Estimates show that an average time of the *V–T* relaxation in nitrogen containing 0.07% water vapor at a pressure of 78 Torr is $\tau_{VT} \cong 5 \times 10^{-3}$ s, so that $\tau_{VT} < \tau_S$.

Taking into account that the nitrogen–water vapor mixture contains additionally 0.4% of oxygen, the *V–T* relaxation time will further decrease because the vibrational relaxation constant for nitrogen on oxygen is two orders of magnitude greater than that for pure nitrogen [13]. All these estimates indicate that the pinching is accompanied by intense vibrational *V–T* relaxation leading to an increase in the gas temperature in the dis-

charge plasma. Owing to a strong temperature dependence of the vibrational relaxation constant, this gives rise to a further increase in the temperature and so on. Thus, the sound is subject to a nonlinear amplification in the discharge plasma according to the theory [4, 5]. However, no unlimited growth in the temperature will take place because a considerable proportion of the vibrationally excited molecules exhibit relaxation. As a result, a stationary pinched discharge regime is set, which corresponds to a different nonequilibrium state of the plasma. An increase in the sound intensity up to $J_0 > 75$ dB leads to a decrease in the pinching-induced gain jump. This is related to the appearance of an acoustic vortex flow, which produces radial mixing of the plasma in the column leading to a decrease in the gas temperature, the *V–T* relaxation rate, and the sound wave amplification.

Adding oxygen into the discharge medium (at a constant discharge current and gas pressure in the tube) leads to a significant increase in the coefficient of sound wave amplification. For example, the gain increased by a factor of approximately 1.5 for the discharge in a mixture of nitrogen with 10% oxygen at a pressure of 78 Torr.

REFERENCES

1. H.-J. Bauer and H. E. Bass, Phys. Fluids **16** (7), 988 (1973).
2. E. Ya. Kogan and V. N. Mal'nev, Zh. Tekh. Fiz. **47** (3), 653 (1977) [Sov. Phys. Tech. Phys. **22**, 391 (1977)].
3. A. I. Osipov and A. I. Uvarov, Inzh.-Fiz. Zh. **55** (1), 149 (1988).
4. E. Ya. Kogan and N. Ya. Molevich, Zh. Tekh. Fiz. **56** (5), 941 (1986) [Sov. Phys. Tech. Phys. **31**, 573 (1986)].
5. A. V. Eletskiĭ and E. V. Stepanov, Khim. Fiz. **8** (9), 1247 (1989).
6. Z. I. Avdus' *et al.*, in *Practical Works on General Physics* (Prosveshchenie, Moscow, 1971), p. 85.
7. G. A. Galechyan, Usp. Fiz. Nauk **165** (12), 1357 (1995) [Phys. Usp. **38**, 1309 (1995)].
8. G. A. Galechyan, A. R. Mkrtchyan, and L. B. Tavakalyan, Fiz. Plazmy **19** (11), 1400 (1993) [Plasma Phys. Rep. **19**, 734 (1993)].
9. G. A. Galechyan, Laser Phys. **4** (1), 23 (1994).
10. A. V. Eletskiĭ, in *Chemistry of Plasma*, Ed. by B. M. Smirnov (Énergoatomizdat, Moscow, 1982), Vol. 9, pp. 151–178.
11. A. V. Eletskiĭ, L. A. Palkina, and B. M. Smirnov, *Transport Phenomena in Weakly Ionized Plasma* (Nauka, Moscow, 1992).
12. M. Whitson and R. McNeal, J. Chem. Phys. **66**, 2696 (1977).
13. V. N. Kondrat'yev, *Chemical Kinetics of Gas Reactions* (Akad. Nauk SSSR, Moscow, 1958; Pergamon, Oxford, 1963).

Translated by P. Pozdeev

Technical Physics Letters, Vol. 27, No. 7, 2001, pp. 608–610. Translated from Pis'ma v Zhurnal Tekhnicheskoĭ Fiziki, Vol. 27, No. 14, 2001, pp. 74–79.

The Electron Pinch Lifetime in High-Current Rod Pinch Diodes

S. Ya. Belomyttsev and V. V. Ryzhov*

Institute of High-Current Electronics, Siberian Division, Russian Academy of Sciences, Tomsk, Russia

** e-mail: ryzhov@to.hcei.tsc.su*

Received February 13, 2001

Abstract—In high-current coaxial diodes with rod anode (rod pinch diodes), the current of the magnetic self-insulation in the gap is approximately two times greater than the critical magnetic insulation current ($J_S \approx 2J_C$). Based on this fact, a model is proposed according to which a quasistationary electron pinch state in such diodes is explained by a change in the gap magnetic insulation conditions caused by the pinch formation. This circumstance can be used to evaluate the pinch lifetime Δt. The Δt values calculated using the oscillograms measured on the Gamble I accelerator agree satisfactorily with the values experimentally determined in a coaxial rod pinch diode. © *2001 MAIK "Nauka/Interperiodica".*

High-current coaxial diodes with rod anode (rod pinch diodes, RPDs) were developed and experimentally characterized in 1978 in the Naval Research Laboratory (United States) using the Gamble I accelerator [1]. Recently, these diodes have drawn the attention of researchers again as possible sources of high-power X-ray radiation possessing a record emission intensity level [2, 3] exceeding that known in other sources.

The experiments [1, 2] showed that an increase in the RPD current leads to the formation of an electron pinch, which is transported along the rod anode and arrested at the anode tip, after which the RPD operates in a quasistationary regime characterized by stable impedance and a stable diode current (with respect to small voltage variations [1]. In this very stage, an outburst of high-intensity X-ray radiation takes place. The duration of this stage, or the pinch lifetime, is an important characteristic determining the efficiency of X-ray emission in RPDs.

The pinch formation under the conditions of magnetic self-insulation in high-current RPDs was explained [1] by reaching a critical value of the intrinsic magnetic field strength of the electron beam in the gap. Note that the electron pinch may exist under these conditions only in the regime of current buildup. Indeed, at a constant diode current, a decrease in the gap width as a result of the motion of the anode and cathode plasmas immediately leads to a drop of the magnetic field strength below the critical level, so that $\Delta t = 0$. In order to remove the discrepancy, it was postulated [1] that the intrinsic magnetic field retards the anode plasma, so that the critical current of magnetic insulation is stabilized and the pinch lifetime is determined by the time of instability development in the anode plasma held by the magnetic field. However, this hypothesis does not always provide a satisfactory explanation, since the cathode plasma also moves, the gap decreases, and the critical current grows.

We propose an explanation of the quasistationary state of the electron pinch in RPDs, which does require an assumption concerning retardation of the emission from cathode by the circular region (Fig. 1). In a stationary state, the z component of the field and particle momentum in the gap is constant. Therefore, the flux of this momentum component through the volume boundary is zero:

$$\frac{1}{8\pi}\int_{R_A}^{R_C}\left[\frac{2(J_b + J_1)}{cr}\right]^2 2\pi r dr - \frac{1}{8\pi}\int_{R_A}^{R_C}\left[\frac{2J_1}{cr}\right]^2 2\pi r dr - P_z = 0. \quad (1)$$

Here, R_A and R_C are the radii of the anode and cathode, respectively; P_z is the flux of the z component of momentum brought by electrons to the anode; c is the speed of light in vacuum; $2(J_b + J_1)/cr$ is the magnetic

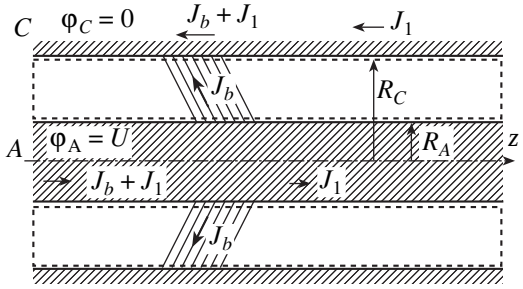

Fig. 1. A schematic diagram illustrating calculation of the magnetic insulation currents in a rod pinch diode: (*A*) anode; (*C*) cathode. Dashed lines indicate the volume for which the condition of conservation of the z component of momentum was used.

field strength on the left-hand volume boundary; $2J_1/cr$ is the analogous value on the right-hand volume boundary; J_b is the electron beam current; and J_1 is the external current. We neglect the contribution due the magnetic field of the ion current, assuming this current to be much smaller as compared to the electron current. The ion contribution to the z component of momentum is ignored because ions are weakly deflected in the magnetic field.

Let us determine the maximum values of J_b and J_1, above which a stationary current J_b cannot flow without the electron beam (or part of it) crossing the edge of the volume under consideration. Apparently, this corresponds to the case when all electrons at the anode would possess only the z component of velocity:

$$P_z = \frac{J_b}{e} mc\sqrt{\gamma^2 - 1}, \tag{2}$$

where $\gamma = 1 + eU/mc^2$; e and m are the electron charge and mass, respectively; and U is the anode voltage. Substituting (2) into (1) yields

$$J_b + 2J_1 = J_0 \frac{\sqrt{\gamma^2 - 1}}{\ln(R_C/R_A)}, \tag{3}$$

where $J_0 = mc^3/e \approx 17$ kA.

The beam with a sufficiently small current ($J_b \ll J_1$) is magnetized by the external current J_1 when the latter reaches a certain critical value J_c for the magnetic insulation. In a one-electron approximation,

$$J_1 = J_c = \frac{J_0}{2} \frac{\sqrt{\gamma^2 - 1}}{\ln(R_C/R_A)}. \tag{4}$$

In the case of the magnetic self-insulation ($J_1 = 0$), formula (3) yields

$$J_b = J_s = J_0 \frac{\sqrt{\gamma^2 - 1}}{\ln(R_C/R_A)}. \tag{5}$$

Thus, the self-insulation current J_s is two times the critical value J_c:

$$J_s = 2J_c. \tag{6}$$

In real diodes, the gaps have finite dimensions in the z axis. The gap boundary effect will change the magnetic insulation currents and their relationships. Therefore, relationship (6) should be considered as approximate. Note that, based on the experimental data, Maenchen *et al.* [3] concluded that a stationary beam pinching regime in high-current RPDs is observed for $J_D \approx 2J_c$, which is consistent with our results.

Based on the above relationship between the critical field and the beam self-insulation current, we propose the following model determining the electron pinch lifetime. The electron beam exhibits pinching at the time instant $t = t_1$ (point A in Fig. 2) provided the magnetic self-insulation condition $J_D = J_s$ (5) is valid. Beginning with this time instant, the diode current passing in the anode rod plays the role of an external current for the gap. Therefore, the gap is overmagnetized in the initial stage of pinching, whereby the magnetic field strength is two times the critical value. The condition of magnetic self-insulation in the gap will hold unless the critical current value increasing as a result of the plasma motion (curve J_c in Fig. 2b) becomes equal to the diode current $J_c = J_D$ at a time instant $t = t_2$ (point B in Fig. 2). Thus, the pinch lifetime can be determined as $\Delta t = t_2 - t_1$.

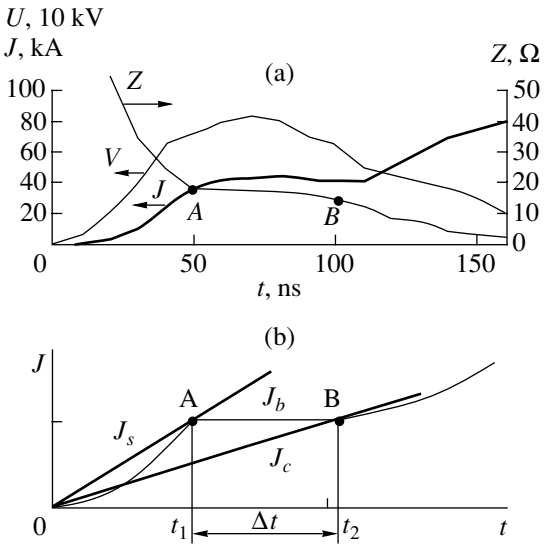

Fig. 2. (a) Typical oscillograms of the current J and voltage V and the impedance profile for an RPD (R_A = 0.08 cm; R_C = 0.58 cm) for the Gamble I accelerator (data taken from [1]). (a) Schematic plots showing the time variation of the diode current J_D, self-insulation current J_s, and critical current J_c.

We may estimate the t value using the oscillograms of current and voltage and the diode impedance reported for the Gamble I setup (Fig. 2a) [1]. Assuming that the anode and cathode plasmas move at the same constant velocity and taking the time from the onset of the current passage to the gap closing equal to $t \approx 160$ ns, we determine the plasma velocity and position at the time instant t_1 for a given gap width. Assuming that the pinching stage corresponds to the time-independent diode impedance [1], we obtain from Fig. 2a that the pinch lifetime is $\Delta t_{\text{exp}} \approx 50$ ns (segment AB in the impedance plot, Fig. 2a). Since the diode voltage at this stage is approximately constant, the critical current growth is determined by a change in the radii of the cathode and anode plasma regions. Therefore, the $\ln(R_C/R_A)$ value decreases by half during the time interval Δt. From this we readily evaluate the pinch lifetime as $\Delta t \approx 57$ ns, which agrees satisfactorily with the above Δt_{exp} value.

Thus, a quasi-stationary state of the electron pinch in a high-current coaxial rod pinch diode can be explained by a change in the magnetic insulation condition in the gap during the pinch formation. The beam pinching takes place in the regime of magnetic self-insulation, when the diode current becomes approximately two times greater than the critical level $J_D = J_s \approx 2J_c$. The condition of the magnetic insulation of the gap in a quasistationary pinching condition is ensured by the diode current for $J_D \geq J_c$.

REFERENCES

1. R. A. Mahaffey, J. Golden, A. Goldstein, and G. Cooperstein, Appl. Phys. Lett. **33** (9), 795 (1978).
2. G. Cooperstein, R. J. Commisso, D. D. Hinshelwood, *et al.*, in *Proceedings of the 12th International Conference on High-Power Particle Beams, 1998*, Vol. 1, p. 31.
3. J. Maenchen, P. R. Menge, D. C. Rovang, *et al.*, Paper presented on the 12th Symposium on High Current Electronics, Tomsk, Russia, 2000.

Translated by P. Pozdeev

Technical Physics Letters, Vol. 27, No. 7, 2001, pp. 611–614. Translated from Pis'ma v Zhurnal Tekhnicheskoĭ Fiziki, Vol. 27, No. 14, 2001, pp. 80–87.

Ultimate InAsSbP Solid Solutions for 2.6–2.8-μm LEDs

V. V. Romanov, É. V. Ivanov, A. N. Imenkov, N. M. Kolchanova, K. D. Moiseev, N. D. Stoyanov, and Yu. P. Yakovlev

Ioffe Physicotechnical Institute, Russian Academy of Sciences, St. Petersburg, 194021 Russia

Received March 7, 2001

Abstract—Epitaxial layers of phosphorus-rich $InAs_{1-y-x}Sb_yP_x$ solid solutions were obtained by liquid phase epitaxy (LPE). The films with $x = 0.32$ were grown at 575°C on isoperiodic (100)InAs substrates. It is shown that the growth of InAsSbP layers from a phosphorus-rich liquid phase is accompanied by saturation of the phosphorus content in the solid state. InAsSbP-based diode heterostructures emitting in the 2.6–2.8 μm wavelength range were obtained, the output emission power of which is sufficient for detecting both natural and industrial gases in the atmosphere. *© 2001 MAIK "Nauka/Interperiodica".*

In recent years, semiconductor diode structures emitting in the middle IR range have been widely used in the spectroscopy of gas molecules occurring in the atmosphere. This is related to the fact that the 2–5 μm wavelength range contains the absorption bands of some natural and industrial pollutants (CO_2, H_2S, C_4H, N_3H, etc.). The 2.6–2.8 μm wavelength range is of special interest for environmental monitoring in ecology because this spectral interval contains absorption bands of carbon dioxide and hydrogen sulfide. Detection of the latter pollutant is very important since H_2S is the main factor leading to the acid rain formation. For this reason, extensive research is now devoted to the development of light-emitting diodes (LEDs) based on multicomponent $A^{III}B^{V}$ compounds that would be capable of operating at room temperature and emitting in the 2.6–2.8 μm wavelength range.

Previously [1, 2], LED structures emitting in the 1.7–2.4 μm wavelength range were obtained by liquid phase epitaxy (LPE) using solid solutions of the $Ga_{1-x}In_xSb_{1-y}As_y$ system. The diode sources emitting at longer wavelengths cannot be obtained by LPE in this solid solution system because there is a region of immiscibility at $0.29 \le x \le 0.74$. On the other hand, LEDs operating in the 2.8–4.5 μm wavelength range were obtained based on the $InAs_{1-y-x}Sb_yP_x$ solid solutions. In particular, LEDS with phosphorus-rich emitter layers ($x = 0.30$) were capable of emitting in the region of 2.8 μm [3]. In order to obtain LEDS emitting in the region of wavelengths shorter than 2.8 μm, it is necessary to grow high-quality emitter layers with a still greater phosphorus content to provide for a good electric confinement. However, this task encounters considerable technological difficulties.

This study presents a continuation of previous research [3]. The purpose of our experiments was to develop an LPE process for the growth of phosphorus-rich $InAs_{1-y-x}Sb_yP_x$ solid solutions and obtain LED structures based on these layers.

The layers of $InAs_{1-y-x}Sb_yP_x$ solid solutions were grown by LPE at $T = 575$°C on *p*-InAs(100) substrates doped with Zn or Mn to an equilibrium charge carrier density of 1×10^{19} cm^{-3}. The number of layers and the amount of phosphorus in the $InAs_{1-y-x}Sb_yP_x$ composition were monitored by X-ray diffraction and by quantitative X-ray probe microanalysis. Data on the epitaxial layer quality and compositions are summarized in the table. These data were used to plot the phosphorus concentration in the solid phase versus its content in the solution melt (Fig. 1).

As is seen from the data presented in Fig. 1 and in the table, an increase in the phosphorus content in the liquid phase above 0.136 mol % (1 mol. fraction = 0.1 mol %) leads to a decrease in the concentration of this element in the solid phase. This is explained by the necessity of increasing the arsenic content in the liquid phase so as to maintain the solution melt in a supersaturated state on further increasing the phosphorus content in the liquid phase. As a result, the content of

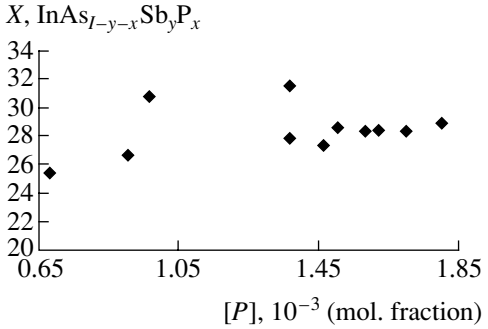

Fig. 1. The plot of phosphorus concentration in the solid phase (X, $InAs_{1-y-x}Sb_yP_x$) versus its content [P] in the liquid phase.

Relationship between the phosphorus content in the liquid phase and in LPE grown solid layers

$X_P^l \times 10^{-3}$	$X_{As}^l \times 10^{-2}$	X_{Sb}^l	$\bar{X}$	$\bar{Y}$	h, μm	$\Delta\alpha/\alpha \times 10^{-3}$
0.68	1.12	0.375	0.254	0.136	1.2	1.59
0.90	1.05	0.405	0.267	0.152	2	3.0
0.96	0.96	0.435	0.308	0.147	1.6	1.07
1.36	1.0	0.473	0.316	0.149	1	0.447
1.36	1.06	0.475	0.279	0.165	1.6	4.17
1.46	1.12	0.4874	0.274	0.159	1.8	5.2
1.5	1.12	0.497	0.286	0.153	1.4	3.63
1.58	1.12	0.51	0.283	0.154	1	2.7
1.62	1.12	0.51	0.284	0.149	1	2.4
1.7	1.12	0.51	0.284	0.148	0.5	2.0
1.8	1.12	0.52	0.289	0.144	0.5	1.7

Note: X_P^l, X_{As}^l, and X_{Sb}^l are the molar fractions of phosphorus, arsenic, and antimony in the solution melt (liquid phase); $\bar{X}$ and $\bar{Y}$ are the average molar fractions of phosphorus and antimony in the epitaxial $InAs_{1-y-x}Sb_yP_x$ layer (solid phase); h is the epitaxial layer film thickness (μm); $\Delta\alpha/\alpha$ is the layer–substrate lattice mismatch.

arsenic in the solid phase increases as well, and, hence, the phosphorus concentration accordingly decreases. In the region of the relative phosphorus content in the liquid phase from 0.146 to 0.18 mol %, the element concentration in the solid phase remains virtually unchanged.

According to [4], the growth in the phosphorus content in the solid phase is prohibited by the condition of molecular limitation ($X_P^l + X_{As}^l + X_{Sb}^l > 0.5$). Experiments showed that introducing phosphorus into the liquid phase above 0.146 mol % does not lead to additional increase in the element content in the solid phase. The results of our investigations indicate that high phosphorus concentrations in the liquid phase do not detrimentally affect the quality of epitaxial layers, but cannot provide for the growth of materials possessing a still greater bandgap width E_g and emitting in the range of shorter wavelengths.

Based on the $InAs_{1-y-x}Sb_yP_x$ solid solution layers grown, we have prepared two- and three-layer heterostructures. The two-layer structures were grown on Zn-doped InAs substrates. Most of the wide-bandgap *p*-type layers with a phosphorus content of 0.32 were doped with Zn until reaching a hole density of $\sim 10^{18}$ cm^{-3}. A narrow-bandgap layer of $InAs_{1-y-x}Sb_yP_x$ with $x = 0.28$ was obtained using undoped material with an electron density of $\sim 10^{16}$ cm^{-3}. Three-layer heterostructures were grown on the substrates doped with either manganese (InAs:Mn) or zinc (InAs:Zn). The phosphorus concentrations in both wide- and narrow-bandgap structures were the same as in the two-layer samples. The wide- bandgap *p*-type layers were doped with zinc to a free hole density of $\sim 10^{18}$ cm^{-3}. The wide-bandgap *n*-type layers, grown above the narrow-bandgap ones, were doped with Sn to a free electron density of $\sim 10^{18}$ cm^{-3}. The narrow-bandgap layer was doped from an In–Zn alloy melt up to a hole density of $\sim 10^{16}$ cm^{-3}. The thickness of wide- and narrow-bandgap layers was 1.2–1.6 and 3.2 μm, respectively.

The LPE-grown heterostructures were used to fabricate mesa-diodes with a diameter of 300 μm by photolithographic technology. The contacts to the *n*- and *p*-type layers were made of Au–Te and Au–Zn alloys, respectively. These diodes were characterized by the current–voltage (*I–V*), spectral, and output power–current (*P–I*) characteristics measured at 300 K for various pulse durations and magnitudes of the injection current.

Figures 2a and 2b show the spectral characteristics of LED structures of the three types studied. The measurements were conducted in a quasi-continuous regime at a pulse repetition rate of 500 Hz, an on–off ratio of 2, and an injection current of 100 mA. In Fig. 2a, curves *1* and *2* show the electroluminescence spectra of three- and two-layer structures grown on InAs:Zn substrates; Fig. 2b refers to a three-layer structures grown on InAs:Mn. The spectra of all samples exhibit three absorption bands at the wavelengths of 2.6, 2.68, and 2.78 μm. The energy separation of these bands and their stability under conditions of the current-induced heating of the active zone indicate that the bands are due to the light absorption by the gas molecules present in the laboratory atmosphere.

Figure 3 shows the output power versus current characteristics measured for various regimes of the nonequilibrium carrier injection in a three-layer LED heterostructure grown on an InAs:Zn substrate. In all power supply regimes studied, the *P–I* curves are linear

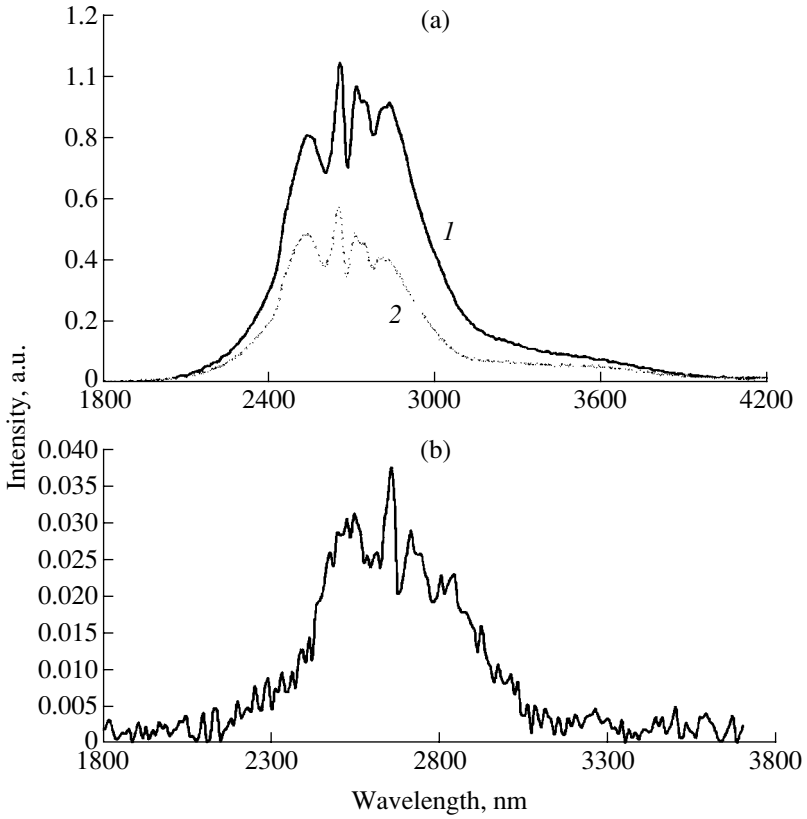

Fig. 2. Electroluminescence spectra of (*1*) three- and (*2*) two-layer $InAs_{1-y-x}Sb_yP_x$ structures grown on (a) InAs:Zn and (b) InAs:Mn substrates.

for currents up to 400 mA, the current-induced heating being significant only above 500 mA. In the pulsed mode (100 μs, 800 mA), the peak output power reached ~100 mW.

As is seen in Fig. 2, all samples (irrespective of the substrate dopant type) exhibit emission bands with a width at half maximum (FWHM) of 70–80 meV. Unfortunately, the absorption bands of atmospheric gases hinder a correct analysis of the shape of the emission band from the standpoint of determining the bandgap width and comparing this to theoretical estimates [5]. A somewhat overstated FWHM value for the emission bands observed suggests that we deal with a total emission due to the interband transitions in the narrow-bandgap layer and in the *p*-InAsSbP emitter layer. The structures grown on Zn-doped *p*-type substrates differ from the samples grown on *n*-InAs [3] by the absence of re-emission effects in the substrate. An analysis of the *P–I* curves showed that the quadratic Auger recombination in the layers studied was lower as compared to the level observed previously [3]. The leaks in the substrates of structures studied in these experiments are lower as well, which is probably explained by a higher phosphorus content in the electric confinement layers.

As expected, the intensity of emission from two-layer structures is lower than that from three-layer ones because of a less pronounced electric confinement. On doping the substrates with manganese, we hoped to obtain a smaller concentration of impurity atoms in the InAsSbP layer (because of a lower coefficient of diffusion for manganese), thus increasing the LED efficiency. However, the efficiency of samples grown on the Mn-doped substrates was found to be minimal in all the sample types studied. This is probably explained by the fact that Mn is a multicharged impurity in $A^{III}B^{V}$ semiconductors, which may enhance the nonradiative recombination channel in the solid solution layers.

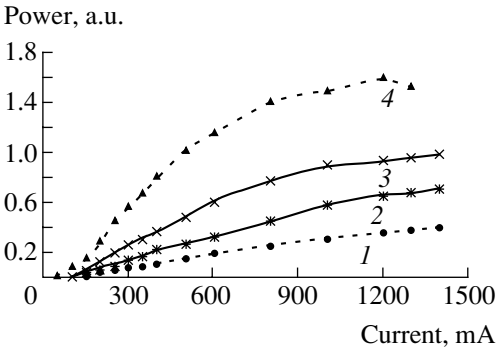

Fig. 3. The plots of output power versus injection current measured for various pulse durations (μs): (*1*) 50 (on–off ratio, 40); (*2*) 100 (20); (*3*) 200 (10); (*4*) 500 (4).

As noted above, the emission spectra (Fig. 2) exhibit three absorption bands. According to the absorption spectra of gas molecules in the 2.5–3.1 μm wavelength range [6], the observed bands can be attributed to carbon dioxide (2.68 and 2.78 μm) and water vapor (2.6 and 2.68 μm) present in the atmosphere.

Thus, the epitaxial growth of InAsSbP layers from a phosphorus-rich liquid phase is accompanied by the saturation of the phosphorus content in the solid state. Increasing the phosphorus content in the liquid phase above 0.146 mol % does not lead to increase in the bandgap width of the InAsSbP solid solution. LED heterostructures based on the LPE-grown InAsSbP solid solutions emit in a 2.6–2.8 μm wavelength range. These structures can be used for detecting carbon dioxide and water vapor by their absorption bands falling within this spectral interval.

Acknowledgments. This study was partly supported by the Russian Foundation for Basic Research (project nos. 99-02-18109 and 00-02-17047) and by the Ministry of Science and Technology (Laser Optics Program).

REFERENCES

1. A. A. Andaspaeva, A. N. Baranov, E. A. Grebenshchikova, *et al.*, Fiz. Tekh. Poluprovodn. (Leningrad) **23** (8), 1373 (1989) [Sov. Phys. Semicond. **23**, 853 (1989)].
2. A. N. Imenkov, O. P. Kapranchik, A. M. Litvak, *et al.*, Pis'ma Zh. Tekh. Fiz. **16** (24), 19 (1990) [Sov. Tech. Phys. Lett. **16**, 931 (1990)].
3. T. N. Danilova, A. N. Imenkov, K. D. Moiseev, *et al.*, Pis'ma Zh. Tekh. Fiz. **20** (10), 20 (1994) [Tech. Phys. Lett. **20**, 394 (1994)].
4. A. N. Baranov, B. E. Dzhurtanov, A. M. Litvak, *et al.*, Zh. Neorg. Khim. **35** (12), 3008 (1990).
5. E. R. Gertner, D. T. Cheung, A. M. Andrews, and J. T. Longo, J. Electron. Mater. **6** (2), 163 (1977).
6. R. D. Hudson, Jr., *Infrared System Engineering* (Mir, Moscow, 1972; Wiley, New York, 1969).

Translated by P. Pozdeev

Technical Physics Letters, Vol. 27, No. 7, 2001, pp. 615–617. Translated from Pis'ma v Zhurnal Tekhnicheskoĭ Fiziki, Vol. 27, No. 14, 2001, pp. 88–94.

Some Features of the Ion-Beam Mixing during Simultaneous Ion Implantation and Metal Deposition

A. D. Pogrebnyak, V. A. Martynenko, A. D. Mikhalev, V. T. Shablya, and V. P. Yanovskiĭ

Institute of Surface Modification, Sumy, Ukraine

Received June 20, 2000; in final form, November 2, 2000

Abstract—Experimental results on the ion implantation of Ta and Cu ions into an Al substrate, accompanied by the deposition of these ions in the form of a surface coating are reported. The coatings composed of the implant elements exhibit a complicated structure and lead to an increase in the microhardness, adhesion properties, and corrosion resistance of the substrate. An analysis of data on the energy distribution of secondary ions shows that the surface layer of ion-implanted substrates contains intermetallic phases. © *2001 MAIK "Nauka/Interperiodica".*

As is well known, the main disadvantages of ion implantation are (i) a relatively low production efficiency, which is determined by the rate of the implanted dose accumulation amounting to $\approx 10^{16}$ cm^{-2} over an area of 300 cm^2 [1, 2] and (ii) a small implant concentration for ions with large masses, which is explained by the increasing role of sputtering.

At the same time, the process of implantation by recoil ions (or ion-beam mixing) based on the incorporation of atoms from surface layers to which a kinetic energy is transferred by the primary beam has good prospects as a method for obtaining new structures and compounds with preset properties [2–4].

One of the possible ways of eliminating the aforementioned disadvantages is to use a combined setup including an arc plasma source for the coating deposition and an additional source for the ion implantation. In such a system, the process may be conducted using the two sources operating either simultaneously or sequentially [4]. The combined process involves mutual diffusion of atoms from the coating and substrate as a result of the atomic or ballistic mixing. This results in the smearing of a sharp interface between the materials and increasing the adhesion, which allows the deposition–implantation process to be used for predicted modification of the working properties of articles and materials.

The purpose of our experiments was to study the process of ion-beam mixing during simultaneous deposition and implantation of Cu and Ta ions into Al substrates.

The experiments were performed with 200- or 500-μm-thick Al samples, the surface of which was preliminary cleaned by sputtering with Ar^+ ions. Then Cu^+ or Ta^+ ions were either plasma-deposited with or without additional implantation of the same ions at an accelerating voltage of 60 kV.

The samples were prepared in the following regimes (subscripts "i" and "d" indicate implantation and deposition, respectively):

(1) Al($Ta_d^+ + Ta_i^+ + Ta_d^+$), implantation dose $\approx 8 \times 10^{15}$, Ta film thickness ≈40 nm;

(2) Al($Ta_d^+ + Ta_i^+ + Ta_d^+$) + ($Cu_d^+ + Cu_i^+ + Cu_d^+$) implantation dose $\approx 8 \times 10^{15}$, Ta film thickness ≈25 nm, Cu film thickness ≈30 nm;

(3) Al($Ta_d^+ + Ta_i^+ + Ta_d^+$) + ($Cu_d^+ + Cu_i^+ + Cu_d^+$) + ($Ta_d^+ + Ta_i^+$), implantation dose $\approx 10^{16}$, first Ta film thickness ≈45 nm, Cu film thickness ≈55 nm; second Ta film thickness ≈70 nm;

(4) Regime 3 + Ta_d^+.

The implantation and deposition processes were carried out using an accelerator with an implantation pulse duration of about 200 μm and a deposition pulse duration of 0.8–1 ms; the process was conducted in a vacuum of $\approx 10^{-3}$ Pa. The experimental regimes are described in more detail elsewhere [2]. The experimental conditions were varied by controlling the implantation dose, substrate temperature, pulse repetition rate, and the film deposition rate. The elemental compositions were studied by Auger electron spectroscopy (AES) and secondary ion mass spectrometry (SIMS) [5, 6]. The ion sputtering was performed either with an Ar^+ beam with the parameters $E = 2$ keV, $j = 5 \times 10^{-5}$ A/cm^2 (dynamic sputtering mode) or with an N^+ ion beam with $E = 2$ keV, $j = 1 \times 10^{-7}$ A/cm^2 (static sputtering mode). The experimental setup was equipped with an energy analyzer that allowed the energy distributions of secondary ions (EDSI) to be measured.

A comparison of the changes in the EDSI pattern measured on the Cu and Ta films on Al obtained by dep-

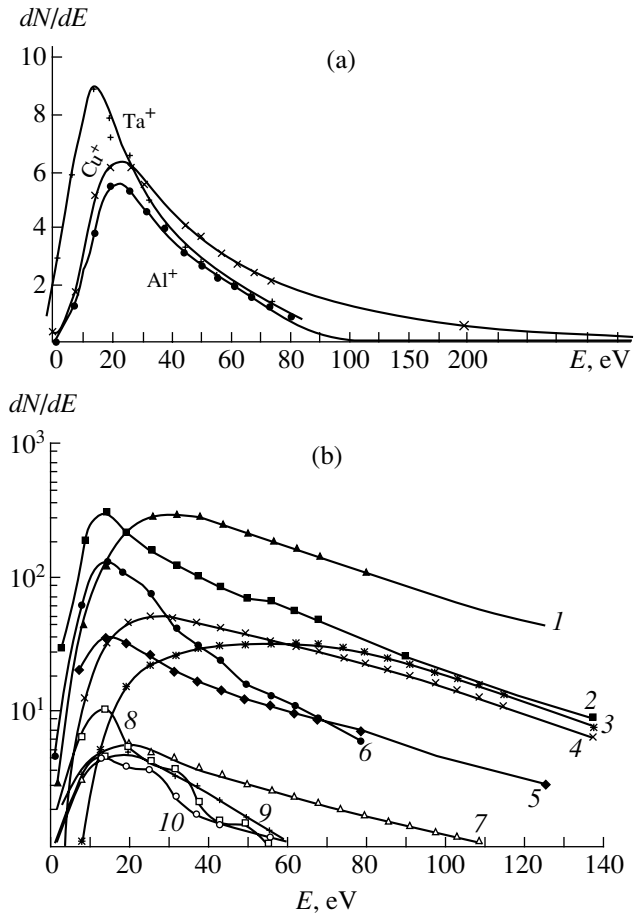

Fig. 1. Energy profiles of secondary ions for the surface of (a) Al substrate after deposition of Cu and Ta and (b) Al substrate after deposition and implantation of the same ions in regime 3 (in various regions of the coating).

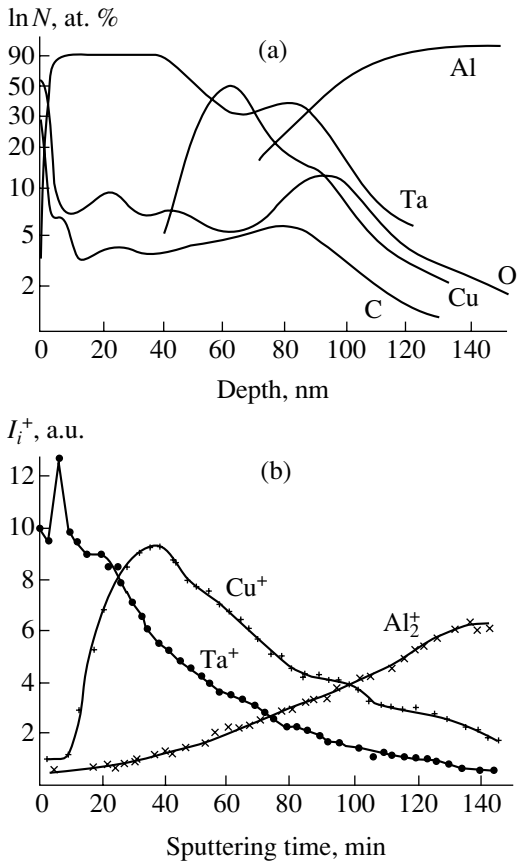

Fig. 2. (a) Elemental depth–concentration profiles obtained by SIMS for the surface layers of Al after implantation of Cu (20 min) and deposition–implantation of Ta (10 min, regime 2). (b) Elemental depth (sputter time)–composition profiles obtained by AES for the surface layers of Al after deposition–implantation of Ta and Cu (15 min, regime 3).

osition without mixing (Fig. 1a) and by a combined deposition–implantation process in regime 3 (Fig. 1b) shows evidence of a change in the character of chemical bonds as a result of the ion-beam mixing. The EDSI peak position changes only slightly (by 10 eV) toward greater energies.The width of the energy distribution exhibits a more pronounced variation, considerably increasing upon the onset of sputtering of the film–substrate interface (Fig. 1b, curves *1*, *4*, *7*, and *9* for Cu, curves *2*, *5*, *6*, *8* for Ta, and curves *3* and *10* for Al). The most significant changes in the width of energy spectra are observed for Cu and Al ions. In addition, an interesting feature is revealed by curves *8* and *10* in Fig. 1b showing several peaks instead of one, which is evidence of an additional interaction with the residual atmosphere components—probably, with oxygen, leading to the formation of oxides (Ta_2O_5–Al_2O_3) at the interphase boundary. All these changes in the EDSI curves (width, main peak position, appearance of additional peaks) are indicative of an increase in the binding energy and the work function. This, in turn, is evidence of the interaction between target components at the film–substrate interface (caused by ballistic mixing and recoil ion implantation) with the formation of a complex system of intermetallic phases [5, 7–9].

An analysis of the elemental depth–concentration profiles observed for the samples obtained in two regimes (Fig. 2) shows, in addition to the complicated shape of Ta and Cu profiles (multipeak structure), the presence of a high concentration of carbon on the surface and at the film–substrate interface. Oxygen also exhibits a complicated profile and an increase in concentration at the film–substrate interface. The shapes of the Auger electron spectra of oxygen and carbon indicated that these elements could be present in the form of oxides and carbides, as well as in the free state.

The measurements of microhardness of the coated samples, performed with the aid of the Knoop pyramidal indenter with variable load, showed that the ion-beam mixing leads to an increase in microhardness up to 153 ± 6 kg/mm^2. This gain in microhardness was markedly greater than that in the case of pure implantation with Cu or Ta, where the resulting microhardness was 96 ± 4 kg/mm^2. It must be noted that the thickness

of the hardened layer in the case of the combined deposition–implantation process is also greater than that in implanted aluminum.

The results of adhesion testing showed that the combined deposition–implantation process increases the adhesion of coating to the aluminum substrate above 120 ± 8 kg/mm^2. The corrosion resistance of the coated material also markedly increased—by almost two orders of magnitude as compared to the initial material.

Thus, the deposition of Ta and Cu ions accompanied by their simultaneous implantation into Al substrates results in the formation of coatings with complicated elemental profiles revealing mutual penetration of elements from the film into the substrate and vice versa. All these factors suggest that the combined deposition–implantation process is more effective than ion implantation alone. This is also manifested by increasing microhardness and adhesion values and by a two-order increase in the corrosion resistance of aluminum.

Acknowledgments. The authors are grateful to A.M. Tolopa for his help in conducting the deposition and implantation processes and to O.G. Bakharev for the fruitful discussion of results.

This study was supported by the Ukrainian Scientific-Technological Center (project no. 1472) and by the Ukraine–Germany Joint Scientific Cooperation Program.

REFERENCES

1. A. I. Aksenov, S. P. Bugaev, N. T. Pankovets, and A. M. Tolopa, Prib. Tekh. Éksp., No. 3, 139 (1987).
2. A. D. Pogrebnjak and A. M. Tolopa, Nucl. Instrum. Methods Phys. Res. B **52**, 25 (1990).
3. A. D. Pogrebnjak, A. P. Kobzev, B. P. Gritsenko, *et al.*, J. Appl. Phys. **87** (5), 2142 (2000).
4. A. D. Pogrebnjak, O. G. Bakharev, N. A. Pogrebnjak, *et al.*, Phys. Lett. A **265**, 225 (2000).
5. L. G. Kositsin, N. N. Nikitenkov, L. N. Puchkareva, and V. P. Yanovskiĭ, in *Nuclear-Physical Methods of Analysis and Their Application for Analysis of Matter Composition* (Atomizdat, Moscow, 1983), p. 67.
6. A. V. Kozhevnikov, V. I. Kravtsov, and V. A. Pirogov, Prib. Tekh. Éksp., No. 3, 67 (1986).
7. N. N. Nikitenkov, Author's Abstract of Candidate's Dissertation in Mathematical Physics (Tomsk, 1987), p. 18.
8. Yu. A. Bykovskiĭ, V. N. Nevolin, and V. A. Fominskiĭ, *Ion and Laser Implantation of Metallic Materials* (Énergoatomizdat, Moscow, 1991).
9. A. N. Didenko, A. E. Ligachov, and A. D. Pogrebnjak, Nucl. Instrum. Methods Phys. Res. B **17**, 165 (1986).

Translated by P. Pozdeev